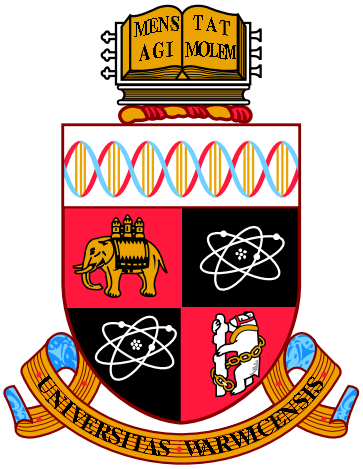


# Tunnelling effects in multiferroic tunnel junctions

by

**Geanina Apachitei**

**Thesis**

Submitted to the University of Warwick

for the degree of

**Doctor of Philosophy**

**Physics**

July 2017

# Contents

# List of Figures

# List of Tables

# Acknowledgments

I would like to thank Prof. Marin Alexe, my supervisor for introducing me to the subject of thin film growth and microelectronics and for giving me the opportunity to do a PhD in this exciting field. I would also like to thank him for his encouragement, support and advice on physics, as well as life in general. I would like to thank every member of the Department of Physics who have helped me get to this point.
I am grateful to Prof. Dietrich Hesse for allowing me to use the PLD system in the 'Max Planck' Institute for Microstructure Physics in Halle and everyone there for all their help.
I am extremely grateful to Dr. Andy Quindeau for introducing me to the practical aspects of tunnelling devices and training me in thin film growth, as well as for thoroughly reading the first chapter.
I would like to thank Jon Peters for training me in TEM sample preparation and image acquisition, as well as Dr. Ana Sanchez and Dr. Richard Beanland in the Warwick Microscopy Group for their guidance in TEM and fruitful collaboration. I also appreciate the time and effort put into training and discussions by Dr. Martin Lees (magnetic measurements), Dr. David Walker (X-ray diffraction) and Dr. Dongjik Kim (PFM).
I would like to express my deep gratitude to the Electronic Functional Materials and Surface and Interface Groups at Warwick University, the group from 'Max Planck' Institute and the Dielectrics, Ferroelectrics and Multiferroics Group at 'Al. I. Cuza' University in Iasi, Romania for all the helpful conversations and encouragements.
I would like to acknowledge Daniel Brunt for helping me with Latex and offering valuable feedback on the theoretical chapters.

# Declarations

I declare the content of thesis is my own work except where states otherwise. The growth was carried out at the 'Max Planck' Institute for Microstructure Physics in Halle Germany, as well as part of structural and electrical characterisation. The main part of characterisation and investigations were performed in the Department of Physics at the University of Warwick, during the period of October 2013 to March 2017 under the supervision of Prof. Marin Alexe. The research carried out here has not been submitted, either fully or in part, for admission to a higher degree in any other academic institution. The transmission microscopy sample preparation and analysis in Chapter 5 has been done by Jonathan James Prescott Peters under the supervision of Dr. Ana Sanchez in the Warwick Microscopy group. The piezoresponse force microscopy experiment in the same chapter was realised with the help of Dr. Dongjik Kim.

Work carried out by the author of this thesis during the PhD published in refereed journals:

- Antiferroelectric tunnel junctions, *Geanina Apachitei*, Jonathan J. P. Peters, Ana M. Sanchez, D.J. Kim, Marin Alexe, Advanced Electronic Materials (2017)
- Polarization curling and flux closures in multiferroic tunnel junctions, Jonathan J. P. Peters, *Geanina Apachitei*, Richard Beanland, Marin Alexe and Ana M. Sanchez, Nature Communications 7 (2016): 13484.
- Four-state ferroelectric spin-valve, Andy Quindeau, Ignasi Fina, Xavi Marti, *Geanina Apachitei*, Pilar Ferrer, Chris Nicklin, Eckhard Pippel, Dietrich Hesse and Marin Alexe, Scientific Reports 5 (2015).

Work presented in this thesis and at the moment waiting to be submitted to a refereed journal:

- Polarisation influence on spin transport in multiferroic tunnel junctions with $PbTiO_3$ and $PbZrO_3$ barriers, *Geanina Apachitei*, Marin Alexe, in preparation

Work in this thesis presented at international conferences by the author:

- Polarisation effect on tunnelling magnetoresistance in multiferroic tunnel junctions, *Geanina Apachitei*, Marin Alexe, TO-BE Spring Meeting, 3-5th April 2017, Luxembourg, Luxembourg (poster)
- Ferroelectric and antiferroelectric tunnel junctions, *Geanina Apachitei*, Marin Alexe, TO-BE Spring Meeting, 6-8th April 2016, University of Warwick, United Kingdom (oral presentation)
- Polarization influence on electronic transport in multiferroic tunnel junctions, *Geanina Apachitei*, Andy Quindeau, Dietrich Hessse, Marin Alexe, Electroceramics, 16-20th June 2014, Bucharest, Romania (poster)

# Abstract

The demands from electronic devices have always been to be portable, fast, non-volatile, more intelligent and to consume low energy. One way towards this goal is to introduce multifunctionality of materials in devices. Ferromagnetism and ferroelectricity are two order parameters that can be coupled in a limited number of multiferroics and their coexistence implies the control over magnetisation and polarisation with both electric and magnetic fields. Similar properties were observed at ferromagnetic/ferroelectric thin film interfaces and attracted attention, since high quality thin film devices can be easily obtained nowadays through monitoring in real time of their structural and physical properties. This effect was observed also in tunnel junction configurations, devices which are formed from metallic electrodes separated by a very thin insulating barrier. By combining a barrier with various ferroelectric order parameters (ferroelectric, antiferroelectric, ferrielectric) and ferromagnetic electrodes, multi-field controlled multi-state non-volatile memory devices can be obtained. Tunnelling processes, especially in junctions containing $d$ orbital elements are not completely understood and need deeper investigation.

In this thesis, multiferroic tunnel junctions with $La_{0.7}Sr_{0.3}MnO_3/PbTiO_3/Co$ structure are shown to be functional down to 3 unit cells. Moreover, the domain structure is shown to change with thickness, going through complex patterns including toroidal flux closure structures.

The fabrication and working principle of the novel antiferroelectric tunnel junctions are reported for the first time using $La_{0.7}Sr_{0.3}MnO_3/PbZrO_3/Co$ structures. Both investigated systems exhibit a multiferroic interface characterised by a magnetoelectric coupling which can be tailored by switching the ferroelectric polarisation.

# Abbreviations

| | |
|---|---|
| ABF | Annular bright field |
| ADF | Annular dark field |
| AFE | Antiferroelectric |
| AFM | Atomic force microscopy |
| AFM* | Antiferromagnet |
| AFTJ | Antiferroelectric tunnel junctions |
| AMR | Anisotropic magnetoresistance |
| DOS | Density of states |
| DT | Direct tunnelling |
| ER | Electroresistance |
| FE | Ferroelectric |
| FIB | Focused ion beam |
| FM | Ferromagnet |
| FNT | Fowler-Nordheim tunnelling |
| FTJ | Ferroelectric tunnel junction |
| GM | Glazman-Matveev |
| GMR | Giant magnetoresistance |
| LSMO | Lanthanum strontium manganate $La_{1-x}Sr_xMnO_3$ |
| MFTJ | Multiferroic tunnel junctions |
| MR | Magnetoresistance |
| MRAM | Magnetic random access memory |
| MTJ | Magnetic tunnel junction |

| | |
|---|---|
| PFM | Piezoresponse force microscopy |
| PLD | Pulsed laser deposition |
| PTO | Lead titanate, $PbTiO_3$ |
| PZO | Lead zirconate, $PbZrO_3$ |
| PZT | Lead zirconium titanate, $PbZr_xTi_{1-x}O_3$ |
| PPMS | Physical properties measuring system |
| RHEED | Reflection high energy electron diffraction |
| RSM | Reciprocal space mapping |
| SEM | Scanning electron microscopy |
| SQUID | Superconducting quantum interference device |
| SRO | Strontium ruthenate $SrRuO_3$ |
| STO | Strontium titanate, $SrTiO_3$ |
| TEM | Transmission electron microscopy |
| TER | Tunnelling electroresistance |
| TEMR | Tunnelling electro-magnetoresistance |
| TI | Thermoionic injection |
| TMR | Tunnelling magnetoresistance |
| u.c. | Unit cells |
| VSM | Vibrating sample magnetometer |
| WKB | Wentzel-Kramers-Brillouin |
| XAS | X-ray absorbtion spectrum |
| XRD | X-ray diffraction |
| XMCD | X-ray magnetic circular dichroism |

# Chapter 1

# Introduction

Nowadays there is an increasing demand for compact, multifunctional and interactive electronics with low energy consumption which are implemented in many aspects of people's lives, from entertainment to health and public security. Semiconductors which are at the base of microelectronics are shifting towards nanoelectronics and approaching fundamental limits at the nanoscale, so there is an interest in introducing new materials and technology processes in practical applications. One way to achieve novel devices is to use multiple functions of a material. A good example are multiferroic materials, in particular those which exhibit magnetic (ferro-, ferri- and antiferromagnetic) and ferroelectric (also ferri- and antiferroelectric) coupled properties which imply multi-field control over the order parameters (magnetisation and ferroelectric polarisation). The magnetoelectric coupling was observed also at ferromagnet/ferroelectric interfaces in thin film structures. The advantage in this case is the possibility of tailoring the final properties with the selection of the component materials, which could be achieved once the processes at the interfaces are fully understood.

In semiconductor devices, electric fields are used to control the electron transport, while in magnetic materials, the spin up (majority) and spin down (minority) populations are unequal and a current through these materials is expected to be spin polarised, controllable by both electric and magnetic field. This additional degree of freedom has been widely investigated and exploited within the field called spintronics (spin electronics). One of the main emerging applications are the magnetic tunnel junctions formed by two ferromagnets separated by a very thin insulating barrier. They are characterised by a bi-stable resistance, yielding a performance parameter called tunnelling magnetoresistance which can reach $10^3$% [1].

Ferroelectric materials also attracted attention lately, due to improvements in the

growth processes allowing high quality epitaxial films to be achieved. Nowadays, local investigations of the physical properties of ultrathin films can be performed with atomic resolution [2, 3], monitoring of the structure in real time by reflection high energy electron diffraction is very common and even the evolution of the ferroelectric polarisation during growth can be obtained [4]. Ferroelectrics can be used on their own in memory applications, replacing the plain insulator barriers in devices called ferroelectric tunnel junctions which are bi-stable due to the polarisation orientation and can reach up to $10^6$ ON/OFF ratio [5]. When the evolution of domain configurations during the switching process causes multiple resistive states, they are called memory resistors (memristors). These kind of devices behave like biological synapses and are promising in highly intelligent neuromorphic network applications. By combining ferroelectric barriers with ferromagnetic electrodes, multiferroic tunnel junctions are obtained which can be used in high density multi-state storage devices. In these thin film structures, the importance of the interfaces increases and complex interactions can occur, affecting the spin transport. In particular, it has been observed that a multiferroic interface occurs causing the surface density of states (spin polarisation and tunnelling magnetoresistance) to depend on the ferroelectric polarisation orientation. The tunnelling magnetoresistance was shown to reversibly change its magnitude at polarisation reversal [6] and even its sign in $La_{0.7}Sr_{0.3}MnO_3$ (LSMO)/$PbZr_{0.2}Ti_{0.8}O_3$ (PZT)/Co junctions [7].

LSMO/PZT/Co tunnel junctions present a multiferroic interface which allows the modulation of the density of states in the ferromagnetic electrodes by switching the orientation of the polarisation in the ferroelectric barrier; an effect which is present also in other heterostructures containing $3d$ shell ions. Its origin was considered to be the magnetic moment induced by the interfacial Co ions on the Ti ions. However, theoretical results also pointed towards the contribution of the Zr ions at these interface effects, but there is no experimental confirmation up to date. One of the aims of this thesis is to study separately the effects on the spin transport of the Ti and Zr ions in multiferroic tunnel junctions. Because PZT is a known solid solution of $PbTiO_3$ (PTO) and $PbZrO_3$ (PZO) perovskites, the Zr/Ti composition dictates its structure and properties. A straightforward approach in this study is to fabricate tunnel junctions with PTO (PZT with composition x=0) and PZO (x=1) barriers. The LSMO/PTO/Co and LSMO/PZO/Co systems are interesting even on their own, since PTO is a tetragonal ferroelectric at room temperature while PZO is an orthorhombic antiferroelectric in bulk form. While several experimental and theoretical studies were performed on LSMO/PTO/Co tunnel junctions [8, 9, 10], PZO has not been approached so far as a barrier in tunnel junctions.

Another aim of this thesis is to understand the processes occurring in multiferroic tunnel junctions in the hope of finding a way to improve their performance and by exploiting the barrier properties, even to obtain novel devices. By analysing original experimental results with the help of existing experimental and theoretical observations, this thesis presents the effect of the nature of the tunnelling barrier on the spin transport in LSMO/PTO/Co and LSMO/PZO/Co tunnel junctions.
Chapters 2 and 3 introduce the background needed to understand the experimental results, from the quantum tunnelling principles to the methods used in fabrication and characterisation of the samples. Chapter 3 presents the practical aspects of growth and characterisation of the samples after every step to ensure the high quality of the final devices and to help in understanding the overall behaviour of the fabricated devices.
In chapter 4, LSMO/PTO/Co multiferroic tunnel junctions are shown to display the characteristic four resistive states. The ferroelectric properties of the PTO films are investigated for different thicknesses and the critical thickness where ferroelectricity vanishes is determined. The evolution of complex domains with reducing thickness is reported in a capacitor configuration; from almost classical antiparallel domains through a disordered phase characterised by polarisation curling to a polarisation oriented out of plane. The resulting barrier/electrode multiferroic interface determines a ferroelectricity-controlled spin transport which is investigated with thickness and temperature.
In chapter 5, the behaviour of LSMO/PZO/Co tunnel junctions is reported for the first time. The structures help in defining the concept of novel devices called antiferroelectric tunnel junctions whose behaviour is studied at room temperature. At low temperatures, the devices behave as four-states multiferroic tunnel junctions from which two non-volatile resistive states are dictated by the polarisation direction, characteristic to ferroelectric tunnel junctions. A change in the tunnelling magnetoresistance sign is observed with polarisation reversal and several responsible mechanisms are proposed.
Finally, conclusions are drawn in order to understand the observed tunnelling effects, especially the influence of the ferroelectric polarisation on the spin transport in the investigated systems correlated with the behaviour observed in LSMO/PZT/Co junctions. Then further questions and paths for future work arising from this study are proposed.

# Chapter 2

# Theoretical background

Understanding the experimental results presented in this thesis requires knowledge of electron tunnelling processes and properties of the materials composing the tunnel junctions. The following section will cover the fundamental principles starting with a brief introduction into quantum tunnelling in metal/insulator/metal junctions. The advantages of using functional materials (ferromagnets over plain metallic electrodes and ferroelectrics over plain insulating barriers) are highlighted and correlated to the characteristics of magnetic tunnel junctions, ferroelectric tunnel junctions and multiferroic tunnel junctions. Motivation of the choice of materials used in the tunnelling devices under study ($SrTiO_3$ substrate, $La_{0.7}Sr_{0.3}MnO_3$ and Co electrodes, $PbTiO_3$ and $PbZrO_3$ barriers) and an overview of their properties are provided.

## 2.1 Quantum tunnelling

In a metal/insulator/metal ($M_1$/I/$M_2$) junction, under certain conditions, electrons can tunnel from one metal to the other when a voltage is applied. figure 2.1 a depicts a tunnelling junction which is a capacitor with $M_1$ and $M_2$ metallic electrodes separated by an insulating barrier I as schematically shown in figure 2.1 c. Across the electrodes a small voltage is applied which injects electrons in $M_1$. The electrons having lower energy than the potential barrier given by the insulator, tunnel through the barrier (from left to right 1→2) to $M_2$, where they can be found with a finite probability. This quantum-scale effect originates from the particle-wave duality of the electron: the wave function of the electrons in $M_1$ decreases exponentially through the barrier (region I) and when the barrier is thin enough (of the order of a few nanometers), it also extends significantly beyond the barrier, in $M_2$ (region III). The tunnelling process can be treated in terms of reflected and transmitted

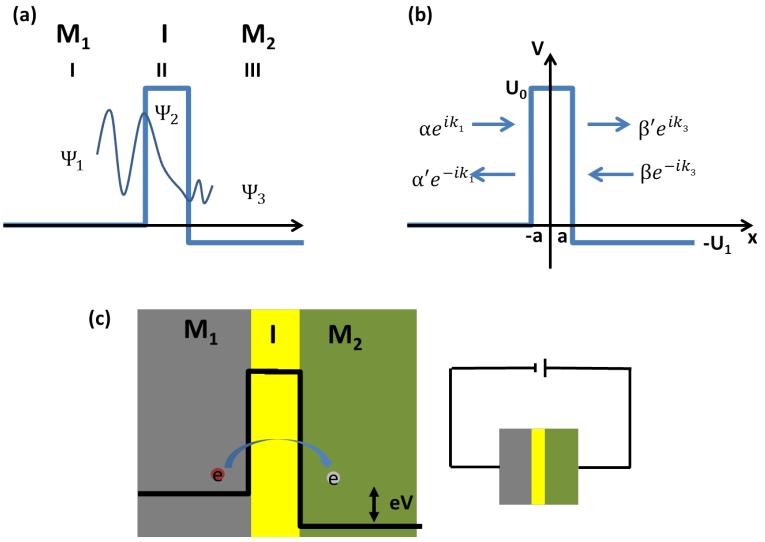


Figure 2.1: a) Tunnelling process highlighting the wave function exponential decay through the barrier and transmission into the second electrode; b) asymmetric square barrier profile with the wave function components for the two metals; c) metal/insulator/metal tunnelling device schematics.

particles. The application of this quantum effect in real devices implies understanding, predicting and controlling the transmission and reflection coefficients for a given barrier potential and an incident particle energy. In the following section, tunnelling through an asymmetric square barrier with thickness $d = 2a$ is treated in one dimension [11]. The time-independent Schrödingers equation in one dimension is:

$$-\frac{\hbar^2}{2m}\frac{d^2\psi(x)}{dx^2} + U(x)\psi(x) = E\psi(x) \tag{2.1}$$

Where $E$ is the total energy of the particle, $U(x)$ the potential energy function and $\psi(x)$ the spatial part of the full wavefunction in equation (2.2), $m$ is the electron mass and $\hbar$ is the reduced Planck's constant.

$$\Psi(x,t) = \psi(x)\exp\left(-i\frac{E}{\hbar}t\right) \tag{2.2}$$

In region I, II and III, the potential is defined by

$$V = \begin{cases} 0 & x < -a; \\ U_0 & -a < x < a; \\ -U_1 & x > a; \end{cases} \tag{2.3}$$

and the Schrödinger equations can be written in the form:

$$\begin{cases} -\frac{\hbar^2}{2m}\frac{d^2\psi_1(x)}{dx^2} = E\psi_1(x) & x < -a; \\ -\frac{\hbar^2}{2m}\frac{d^2\psi_2(x)}{dx^2} = (E-U_0)\psi_2(x) & -a < x < a; \\ -\frac{\hbar^2}{2m}\frac{d^2\psi_3(x)}{dx^2} = (E+U_1)\psi_3(x) & x > a; \end{cases} \tag{2.4}$$

with the solutions:

$$\begin{cases} \psi_1(x) = \alpha e^{ik_1x} + \alpha' e^{-ik_1x} & x < -a; \\ \psi_2(x) = Ce^{ik_2x} + De^{-ik_2x} & -a < x < a; \\ \psi_3(x) = \beta' e^{ik_3x} + \beta e^{-ik_3x} & x > a; \end{cases} \tag{2.5}$$

where $\alpha$, $\alpha'$, $C$, $D$, $\beta$ and $\beta'$ are arbitrary complex constants and $k_1 = \sqrt{2mE}/\hbar$, $k_2 = \sqrt{2m(E-U_0)}/\hbar$ and $k_3 = \sqrt{2m(U_1+E)}/\hbar$ inside the barrier. In the classically forbidden case when the energy of the quantum particle is lower than the potential barrier ($E < U_0$), $k_2$ is imaginary and $\kappa = \sqrt{2m(U_0-E)}/\hbar$ is conventionally used. $\alpha e^{ik_1x}$, $Ce^{ik_2x}$ and $\beta' e^{ik_3x}$ represent the waves travelling in the positive direction of $x$ and $\alpha' e^{-ik_1x}$, $De^{-ik_2x}$ and $\beta e^{-ik_3x}$ are waves travelling in the opposite direction (Figure 2.1 b). The solution in the three intervals can be rewritten as:

$$\begin{cases} \psi_1(x) = \alpha e^{ik_1x} + \alpha' e^{-ik_1x} & x < -a; \\ \psi_2(x) = Ce^{\kappa x} + De^{-\kappa x} & -a < x < a; \\ \psi_3(x) = \beta' e^{ik_1x} + \beta e^{-ik_1x} & x > a. \end{cases} \tag{2.6}$$

The wave function matching method gives the conditions at the boundaries ($\psi(x)$ and its first derivative are continuous). At $x = -a$, they are:

$$\alpha e^{-ik_1a} + \alpha' e^{ik_1a} = Ce^{-\kappa a} + De^{\kappa a} \tag{2.7}$$

$$ik_1\left(\alpha e^{-ik_1a} - \alpha' e^{ik_1a}\right) = \kappa\left(Ce^{-\kappa a} - De^{\kappa a}\right) \tag{2.8}$$

At $x = a$,

$$Ce^{\kappa a} + De^{-\kappa a} = \beta' e^{ik_3a} + \beta e^{-ik_3a} \tag{2.9}$$

$$\kappa Ce^{\kappa a} - \kappa De^{-\kappa a} = ik_3\left(\beta' e^{ik_3a} - \beta e^{-ik_3a}\right) \tag{2.10}$$

Equation (2.7) can be multiplied with $ik_1$ and the addition and substraction of equation (2.8) results in the dependencies of $\alpha$ and $\alpha'$ on $C$ and $D$:

$$2ik_1\alpha e^{-ik_1a} = Ce^{-\kappa a}(ik_1 + \kappa) + De^{\kappa a}(ik_1 - \kappa) \tag{2.11}$$

$$2ik_1\alpha' e^{ik_1a} = Ce^{-\kappa a}(ik_1 - \kappa) + De^{\kappa a}(ik_1 + \kappa) \tag{2.12}$$

A similar treatment (multiplication by $\kappa$) is applied to (2.9) and (2.10), resulting:

$$2\kappa Ce^{\kappa a} = \beta' e^{ik_3a}(\kappa + ik_3) + \beta e^{-ik_3a}(\kappa - ik_3) \tag{2.13}$$

$$2\kappa De^{-\kappa d} = \beta' e^{ik_3a}(\kappa - ik_3) + \beta e^{-ik_3a}(\kappa + ik_3) \tag{2.14}$$

By using equations (2.11) to (2.14), the relation between $\alpha$ with $\beta$ and $\beta'$. The elements of the transfer matrix $M$ can thus be determined.

$$\begin{pmatrix} \alpha \\ \alpha' \end{pmatrix} = M \begin{pmatrix} \beta' \\ \beta \end{pmatrix} = \begin{pmatrix} M_{11} & M_{12} \\ M_{21} & M_{22} \end{pmatrix} \begin{pmatrix} \beta' \\ \beta \end{pmatrix} \tag{2.15}$$

$$M_{11} = \frac{1}{4}\Big[ i\left(\frac{\kappa}{k_1} - \frac{k_3}{\kappa}\right)\left(e^{2\kappa a} - e^{-2\kappa a}\right) + \left(1 + \frac{k_3}{k_1}\right)\left(e^{2\kappa a} + e^{-2\kappa a}\right)\Big] e^{i(k_1+k_3)a} = M_{22}^* \tag{2.16}$$

$$M_{12} = \frac{1}{4}\Big[ i\left(\frac{\kappa}{k_1} + \frac{k_3}{\kappa}\right)\left(e^{2\kappa a} - e^{-2\kappa a}\right) + \left(1 - \frac{k_3}{k_1}\right)\left(e^{2\kappa a} + e^{-2\kappa a}\right)\Big] e^{i(k_1-k_3)a} = M_{21}^* \tag{2.17}$$

By using the hyperbolic functions, $\sinh(2\kappa a) = \left(e^{2\kappa a} - e^{-2\kappa a}\right)/2$ and $\cosh(2\kappa a) = \left(e^{2\kappa a} + e^{-2\kappa a}\right)/2$, they can be written as:

$$M_{11} = \frac{1}{2}\left[ i\left(\frac{\kappa}{k_1} - \frac{k_3}{\kappa}\right)\sinh(2\kappa a) + \left(1 + \frac{k_3}{k_1}\right)\cosh(2\kappa a)\right] e^{i(k_1+k_3)a} \tag{2.18}$$

$$M_{12} = \frac{1}{2}\left[ i\left(\frac{\kappa}{k_1} + \frac{k_3}{\kappa}\right)\sinh(2\kappa a) + \left(1 - \frac{k_3}{k_1}\right)\cosh(2\kappa a)\right] e^{i(k_1-k_3)a} \tag{2.19}$$

Finally, the transmission and reflection coefficients are obtained:

$$T = \frac{|\beta|^2}{|\alpha|^2} = \frac{4\frac{k_3}{k_1}}{\left(\frac{\kappa}{k_1} + \frac{k_3}{\kappa}\right)^2 \sinh^2(2\kappa a) + \left(1 - \frac{k_3}{k_1}\right)^2 \cosh^2(2\kappa a) + 4\frac{k_3}{k_1}} \tag{2.20}$$

$$R = \frac{|\alpha'|^2}{|\alpha|^2} = \frac{\left(\frac{\kappa}{k_1} + \frac{k_3}{\kappa}\right)^2 \sinh^2(2\kappa a) + \left(1 - \frac{k_3}{k_1}\right)^2 \cosh^2(2\kappa a)}{\left(\frac{\kappa}{k_1} + \frac{k_3}{\kappa}\right)^2 \sinh^2(2\kappa a) + \left(1 - \frac{k_3}{k_1}\right)^2 \cosh^2(2\kappa a) + 4\frac{k_3}{k_1}} \tag{2.21}$$

The particle has a non-zero probability of travelling beyond the barrier even when the energy is lower than the barrier potential ($E < U_0$). The results in equations (2.20) and (2.21) correspond to inelastic tunnelling and can be reduced to elastic tunnelling when $k_1 = k_3$. For high, wide barriers ($2\kappa a \gg 1$), the transmission coefficient simplifies to:

$$T \propto \exp\left(-2\kappa a\right) \propto \exp\left(-2\frac{\sqrt{2m(U_0 - E)}}{\hbar}a\right) \tag{2.22}$$

In conclusion, the transmission decreases exponentially with the barrier thickness and $m^{1/2}$. Particles of low mass are more likely to tunnel than heavier particles. In practice, the Wentzel-Kramers-Brillouin (WKB) approximation is used to treat more complicated shaped barriers as a succession of square barriers of different heights when potentials $U(x)$ do not vary rapidly [12]. The transmission coefficient becomes:

$$T \propto \exp\left(-2\int_{-a}^{a} \frac{\sqrt{2m(U(x) - E)}}{\hbar}dx\right) \tag{2.23}$$

## 2.2 Transport mechanisms in thin film structures

In real metal/insulator/metal devices such as the one in figure 2.2 c the reflection and transmission coefficients are related to physical observable quantities such as charge current and conductance, helping to determine the junction performance. The tunnelling current from $M_1$ to $M_2$ electrode (left to right) is given by the characteristics of the barrier and electrodes:

$$I_{1\to2}(V) \propto \int_{-\infty}^{+\infty} N_1(E)N_2(E + eV)Tf(E)[1 - f(E + eV)]dE \tag{2.24}$$

where $N_1(E)$ and $N_2(E+eV)$ are the density of states at energy $E$ and $E+eV$ in $M_1$ and $M_2$, respectively; $f(E)$ and $f(E+eV)$ are the Fermi-Dirac distribution functions,

$e$ is the electron charge and $V$ the applied voltage. The tunnelling current depends on the barrier thickness $d$, height $\Phi$ and tunnelling effective mass of electrons $m_{eff}$ given by the probability of transmission through the barrier $T \propto \exp(-d\sqrt{m_{eff}\Phi})$.

The total tunnelling current through the junctions is $I(V) = I_{1\to2}(V) - I_{2\to1}(V)$:

$$I(V) \propto \int_{-\infty}^{+\infty} N_1(E)N_2(E+eV)T[f(E) - f(E+eV)]dE \tag{2.25}$$

The electrons must be transported from the insulator/$M_1$ interface through the barrier before being emitted into the second metal $M_2$. At the interfaces with $M_1$ and $M_2$ the electron emission occurs depending on the rates of transfer across the metal/insulator boundaries. As these bulk and interface processes are connected in series, the resulting tunnelling current is limited by the ones that cause more scattering [13].

Depending on the thickness of the insulator thin film, the resulting current can be dominated by three tunnelling mechanisms: direct tunnelling, Fowler-Nordheim tunnelling and thermoionic injection (Figure 2.2).

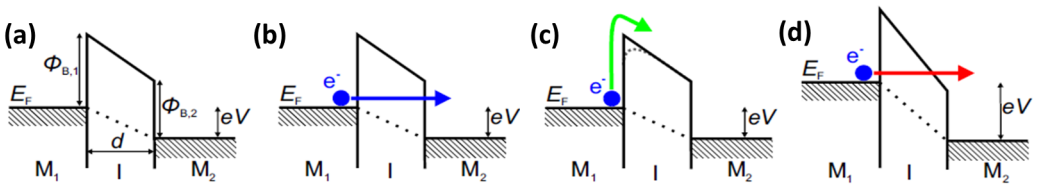


Figure 2.2: a) Tunnelling junctions barrier profile under applied bias; b) direct tunnelling; c) thermionic emission; d) Fowler- Nordheim tunelling mechanisms; reproduced from [20].

### 2.2.1 Direct tunnelling

In the case of direct tunnelling, the electrons tunnel through the barrier when their energy is below the barrier height (Figure 2.2 b).

The Simmons model [14] is applied to general shape barriers at small voltages and brings equation 2.25 to a simpler form which contains the mean height of the barrier $\bar{\phi}$. The Fermi level ($E_F$) is used to express the barrier potential $U(x) = E_F + \bar{\phi}(x)$

and equation 2.25 can be written as [15]:

$$J = \frac{4\pi me}{h^3}\Big[eV\int_0^{E_F-eV}\exp\left[-A(E_F+\bar{\phi}-E_x)^{1/2}\right]dE_x + \int_{E_F-eV}^{E_F}(E_F-E_x)\exp\left[-A(E_F+\bar{\phi}-E_x)^{1/2}\right]dE_x\Big] \quad (2.26)$$

After integration, considering usually $A(\bar{\phi}+eV/2)^{1/2} \gg 1$, the following form is obtained:

$$j = j_0\Big(\bar{\phi}\exp\left[-A\bar{\phi}^{1/2}\right] - (\bar{\phi}+eV)\exp\left[-A(\bar{\phi}+eV)^{1/2}\right]\Big) \quad (2.27)$$

Where $j_0 = \frac{e}{2\pi h(\beta\Delta d)^2}$, $A = (4\pi\beta\Delta d/h)(2m)^{1/2})$, $\Delta d$ is the effective thickness of the barrier and $\beta$ is a correction factor. The experimental data is usually modelled in the case of intermediate applied voltages. The approximations $\bar{\phi} = \phi - eV/2$ and $\beta = 1$ are used. The current density has the following dependence on the barrier mean height $\phi$ and thickness $d$:

$$j(V) = j_0\left(\phi - \frac{eV}{2}\right)\exp\left[-A\sqrt{\phi-\frac{eV}{2}}\right] - j_0\left(\phi+\frac{eV}{2}\right)\exp\left[-A\sqrt{\phi+\frac{eV}{2}}\right] \quad (2.28)$$

where $j_0 = \frac{e}{2\pi hd^2}$ and $A = 4\pi\frac{\sqrt{2m_{eff}}}{h}$ are constants, $m_{eff}$ is the electron effective tunnelling mass and $d$ the barrier thickness.

The Brinkman model describes tunnelling through trapezoidal potential barriers [16]. Considering the barrier is characterised by the potential steps at the interface $\Phi_{B,1}$ and $\Phi_{B,2}$, the applied voltage should be low such that $eV/2 < \Phi_{B,i}$ and the barrier thick enough that $d[(2m_{eff}/\hbar^2)\Phi_{B,i}]^{1/2} >> 1$. Then the current density is given in the following form [17]:

$$j_{DT} = C\frac{\exp\left[\alpha\left(\left(\Phi_{B,2}-\frac{eV}{2}\right)^{\frac{3}{2}} - \left(\Phi_{B,1}+\frac{eV}{2}\right)^{\frac{3}{2}}\right)\right]}{\alpha^2\left(\sqrt{\Phi_{B,2}-\frac{eV}{2}} - \sqrt{\Phi_{B,1}+\frac{eV}{2}}\right)^2} \times \sinh\left[\frac{3eV}{4}\alpha\left(\sqrt{\Phi_{B,2}-\frac{eV}{2}} - \sqrt{\Phi_{B,1}+\frac{eV}{2}}\right)\right] \quad (2.29)$$

where $C = \frac{-4em_{eff}}{9\pi^2\hbar^3}$, $\alpha = \frac{4d\sqrt{2m_{eff}}}{3\hbar\left(\Phi_{B,1}+eV-\Phi_{B,2}\right)}$ and $m_{eff}$ is the electron effective tunnelling mass. In this model, the shape of the potential barrier is given by:

$$\Phi(x,V) = \Phi_{B,1} + eV/2 + x(\Phi_{B,2} - eV - \Phi_{B,1})/d \tag{2.30}$$

and does not consider the effect of the image force between an electron and the surface of the metal which would produce a rounding off of the top corner of the trapezoidal barrier leading to underestimations of the tunnelling current [18, 19].

### 2.2.2 Thermionic injection

The thermionic effect consists in an actual transfer of electrons through the junction. In this case the thermal energy of the electrons is higher than the potential barrier (Figure 2.2 c). The current density can be described by equation 2.31 at voltages higher than $3k_BT/e$

$$j_{TI} = A^{**}T^2\exp\left[-\frac{1}{k_BT}\left(\Phi - \sqrt{\frac{e^3E}{4\pi\epsilon_0\epsilon_i}}\right)\right] \tag{2.31}$$

where $\Phi$ is the potential barrier, $A^{**}$ the effective Richardson's constant and $\epsilon_i$ the permitivity of the ferroelectric responsible for image force lowering.

### 2.2.3 Fowler-Nordheim tunnelling

A triangular shaped barrier can be formed by applying an electric field across a rectangular or trapezoidal barrier. Fowler-Nordheim tunnelling occurs in these barriers in a higher voltage regime, similar to direct tunnelling (Figure 2.2 d). The current density in this case is:

$$j_{FNT} = \frac{e^3m_e}{8\pi hm_{eff}\Phi}E^2\exp\left[-\frac{8\pi\sqrt{2m_{eff}}}{3he}\frac{\Phi^{\frac{3}{2}}}{E}\right] \tag{2.32}$$

The image force lowering does not significantly affect the tunnelling current at room temperature.

## 2.3 Magnetic tunnel junctions

The observation of giant magnetoresistance (GMR) in 1988 [21, 22] triggered further research on the spin of the electrodes and was quickly applied in the data storage

industry, leading to the development of a completely new field called spintronics. Nowadays magnetic tunnel junctions are widely known devices used in common electronic devices [23]. Magnetic tunnel junctions rely on the magnetic properties of materials and are basically tunnel junctions with ferromagnetic electrodes. The application of magnetism in data storage is based on writing the information within the magnetic state of the device and reading it through its resistance. The development of this type of devices was mainly driven by practical industry requirements of non-volatile, faster, smaller, more reliable and less power consuming magnetic random access memories (MRAM).

### 2.3.1 Ferromagnetic materials

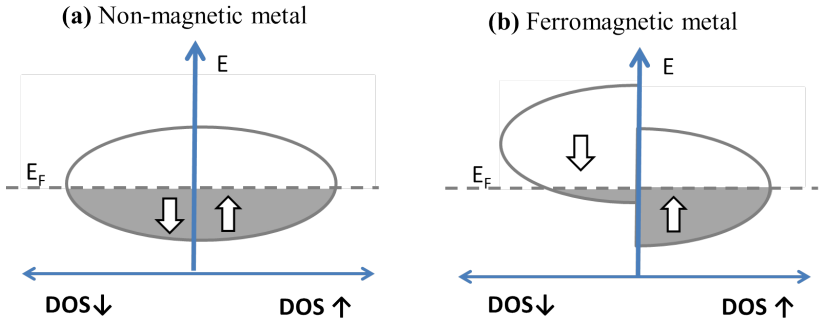


Figure 2.3: Difference between the density of states (DOS) of a) non-magnetic metals and b) ferromagnets.

Ferromagnetism originates from the energy splitting into majority and minority spin subbands in the partially filled $f$ levels in rare earth magnets and $d$ levels in transitional magnets. Figure 2.3 shows the density of states (DOS) of majority (spin up) and minority spins (spin down) of a ferromagnet in comparison with a non-magnetic metal. The difference in energy between the two spin states is called the exchange interaction energy. The nonvolatile nature of ferromagnetism is based on spins aligning under a magnetic field and remaining aligned even after its removal. The ferromagnetic behaviour is caused by coupling of the electron spins by exchange and super exchange coupling. Spins of adjacent cations in transition elements such as Fe, Co and Ni and their compounds are directly coupled in order to align in the same or opposite direction depending on the interatomic distance (exchange coupling). In oxides, the electron spins of the cations are shared through an oxygen anion which facilitates the exchange (superexchange coupling) [24]. There are cases of adjacent cations with spins opposing each other that create two intermixed

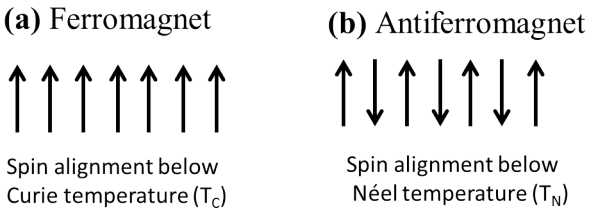


Figure 2.4: Schematic drawing of relative spin orientations in: a) ferromagnetic; and b) antiferromagnetic materials.

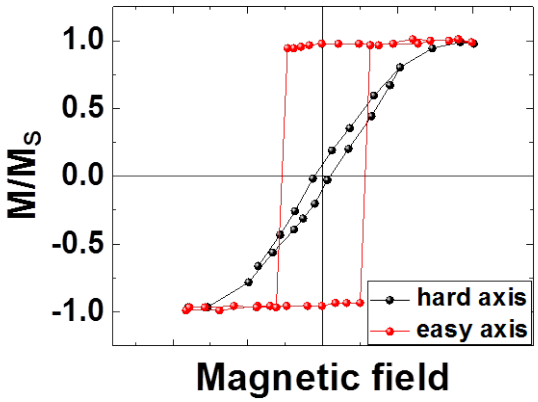


Figure 2.5: Normalised magnetisation hysteresis loops for magnetic field varied along the easy axis (red) and hard axis (black) of a ferromagnetic sample.

sublattices. In the case they are as strongly magnetised, the material has no net magnetic moment and is called a antiferromagnet (Figure 2.4 b). Ferromagnetism and antiferromagnetism are superimposed on paramagnetism, so at the Curie and Neel temperature, respectively they vanish and materials exhibit just paramagnetic properties.

Depending on the size and shape of a magnetic material, it will minimize the magnetostatic energy associated with the surface poles by creating domains which can be opposing each other or form closure domains. Magnetic anisotropy entails the variation of magnetisation strength with the direction of the applied magnetic field which can be caused by three factors: crystalline, shape and magnetoelastic anisotropy. With the origin in the lattice forces acting on the electron spin configuration, the crystal anisotropy dictates the direction-easy axis (easy plane) on which the magnetisation tends to align and have a higher magnitude when magnetic field is applied (Figure 2.5). The shape anisotropy is the attempt of the material to minimize the


Figure 2.6: Cross sectional view of the domain wall structure: a) Bloch domain wall in thick films; b) Neel domain wall in thin films; reproduced from [28].

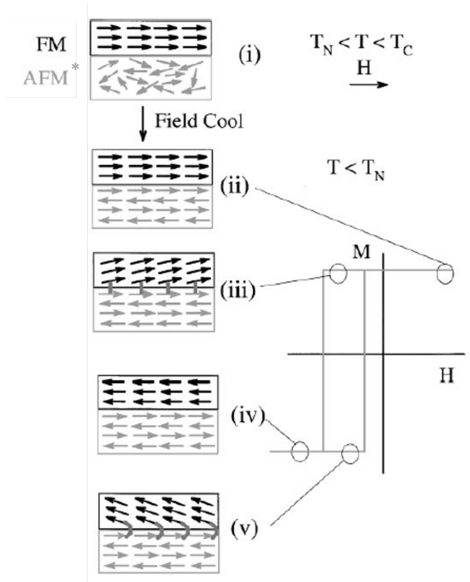


Figure 2.7: Intuitive image of exchange bias at the ferromagnet/antiferromagnet interface illustrated on a hysteresis loop after field cooling from a temperature higher than the Neel temperature of the antiferromagnet and lower than the Curie temperature of the ferromagnet; reproduced from [30].

self-demagnetising fields by setting the surface poles further apart. In-plane magnetic anisotropy is therefore expected in thin films due to their reduced thickness dimension; however perpendicular magnetic anisotropy is also possible in thin films when caused by a dominating magnetocrystalline or magnetoelastic anisotropy.
Magnetic properties of materials in thin film form varies with their thickness, roughness and morphology. Coercivity is proportional to the film thickness when Neel walls are present and decreases with thickness in the case of Bloch walls. While a combination of the characteristics of both types can be found (cross-tie walls), mainly the Neel-type walls are more stable in thin films and the transition to Bloch domain walls occurs when the thickness of the film reaches the domain size. The two types of domain walls are represented in figure 2.6. The rotation axis in the

Bloch walls is perpendicular to the magnetisation in the magnetic domains and to the domain wall plane, while the rotation axis of the spins is perpendicular to the effective magnetisation in the domains and is in the domain wall plane in a Neel wall [25, 26, 27]. The coercivity of a ferromagnetic material can be artificially increased by pinning its orientation using the coupling with an antiferromagnet. This effect is called exchange biasing effect and is characterised by a shift of the hysteresis loop on the field axis with a quantity called exchange field ($H_{EX}$) (Figure 2.7). The coupling occurs at a ferromagnetic/antiferromagnetic interface below the Neel temperature of the antiferroelectric after the structure was cooled in a field high enough to saturate the ferromagnet [29]. This process usually results in a $H_{EX}$ opposite to the applied field which is called negative exchange bias.

### 2.3.2 Magnetoresistance effects

The change in the electrical resistivity of a material caused by an applied magnetic field is generally called the magnetoresistance (MR) effect and is conventionally defined by the values of the high ($R_{high}$) and low ($R_{low}$) resistance states of the device (Equation 2.33). Though not under this name, the effect was studied for the first time on Ni and Fe as far back as 1857 by Thomson [31]. In ferromagnetic materials the change of resistivity usually depends on the angle between the magnetisation and current directions and is called anisotropic magneto resistance (AMR) [32]. The low resistance and the change of just a few percent in AMR devices limited their aplicability in memory storage. A new effect with higher MR ratio was reported in ferromagnet/non-magnetic metal lattices in 1988 and was named giant magnetoresistance (GMR). This discovery is at the base of a new field of research called spintronics which considers apart from the charge of the electrons, also their spin [21, 22]. GMR was adopted in commercial hard disk reading heads and triggered new research in GMR-based memory storage devices. However, the MR range (4-8%) and the low resistivity were not completely compatible with semiconductor applications.

$$MR = \frac{R_{high} - R_{low}}{R_{low}} \tag{2.33}$$

### 2.3.3 Tunnelling magnetoresistance

A better signal for MRAM technology was offered by combining the magnetoresistance effects with quantum tunnelling through an insulating barrier in devices called magnetic tunnel junctions (MTJ). By using ferromagnetic electrodes, the junction resistance depends on the angle between their magnetization direction giving rise to

the tunnelling magnetoresistance (TMR) effect (Figure 2.8 a) defined by:

$$TMR = \frac{R_{\rightleftarrows} - R_{\rightrightarrows}}{R_{\rightrightarrows}} = \frac{2P_1P_2}{1 - P_1P_2} \tag{2.34}$$

where $R_{\rightrightarrows}$ is the resistance in the parallel magnetisation orientation and $R_{\rightleftarrows}$ the resistance in the antiparallel orientation and $P_1$ and $P_2$ are the spin polarisations at the two interfaces.

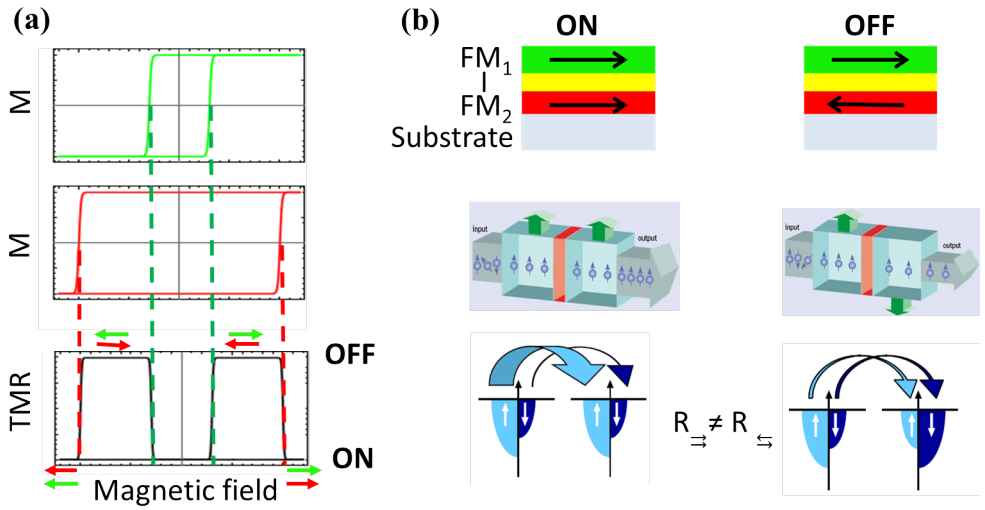


Figure 2.8: a) Resistance change of a magnetic tunnel junction correlated with the magnetisation switching in the top and bottom ferromagnetic electrodes; b) ON and OFF states highlighting the electron spin scattering through the electrodes and the tunnelling in the minority and majority spin channels.

The high value of the resistance and of the TMR (10%) at room temperature and following development made these devices suitable as memory cells in MRAM storing devices [33, 34]. The basic MTJ is composed of a soft ferromagnet (free layer) and a hard ferromagnet (fixed layer) with the same easy axis of magnetisation. Perfect parallel and antiparallel alignment can be obtained by having ferromagnetic films with different values of coercive field, by changing the coercive field during the lithography patterning process or by magnetically pinning one of the layers by exchange bias with an antiferromagnet (AFM*). In a simplistic view, the majority spins of the electrons are oriented in the direction of the applied magnetic field and during the transport through the tunnelling junction get scattered more in the ferromagnetic electrodes with opposite magnetisation than in electrodes where magnetisation is parallel to their orientation. A very simple model for this process is assuming two parallel channels corresponding to the two spin states. As a result the

junction resistance is usually lower in the case of magnetisations aligned parallel to each other in the two electrodes resulting in a positive (normal) TMR (Figure 2.8 b). Apart from the nature of the ferromagnet electrode, the sign of TMR was shown to depend dramatically on the ferromagnet/barrier interface [35], given by the spin polarisations at the two ferromagnet/barrier interfaces $P_1$ and $P_2$ in equation 2.34.

## 2.4 Ferroelectric tunnel junctions

By replacing the insulating barrier in a tunnelling junction with a ferroelectric, the polarisation orientation will influence the tunnelling current and two non-volatile resistive states can be obtained [36].

### 2.4.1 Ferroelectric materials

Ferroelectric materials are characterised by the presence of a spontaneous polarisation even in the absence of an external electric field. A common structure of ferroelectrics is the perovskite structure $ABO_3$ in which the ionic radius of A-site cations is typically larger than that of B-site cations. Spontaneous polarisation is caused by the ionic displacement inside the unit cell and can be switched in the direction of an applied electric field when higher than the coercive field of the material. This gives rise to two non-volatile states given by the field orientations which incur from the $P(E)$ ferroelectric hysteresis loops. By increasing the temperature the symmetry of the material is increased and ferroelectric properties are lost. The temperature where this transition occurs is called the Curie temperature ($T_C$).
The general tendency to minimise the size of electronic devices brought attention to thin films. Ferroelectrics in this form have different properties from their bulk counterparts (Curie temperature, coercive fields) and the reasons are not completely understood. By reducing the thickness of a ferroelectric, polarisation charges give rise to a large depolarisation field which forces the ions into their paraelectric positions. Traditionally, the system reduces the depolarising field by separating into domains and by screening it with charges accumulated at the electrodes [37]. In practice loss of ferroelectricity occurs below a critical thickness, an effect attributed partly to the quality of the devices. This has been improved over time leading to effective thickness approaching the theoretical critical thickness.
There is a special type of material named antiferroelectrics which are similar to the more known antiferromagnets. They exhibit a zero macroscopic polarisation in the absence of an external electric field because they are formed of sublattices with local polarisations that cancel each other. Due to the existence of local dipoles which at

high fields can be oriented, antiferroelectrics are characterised by a double $P(E)$ hysteresis loop.

### 2.4.2 Tunnelling electro-resistance

Two resistive states can be obtained from the polarisation orientations in the barrier in ferroelectric tunnel junctions [38]. This is the origin of the tunnelling electroresistance effect (TER) defined as:

$$TER = \frac{R_{\downarrow} - R_{\uparrow}}{R_{\uparrow}} \tag{2.35}$$

where $R_{\downarrow}$ is the FTJ resistance when the polarisation is oriented towards one of the electrodes, generally the one resulting in the higher resistance value (in this thesis, towards the bottom electrode) and $R_{\uparrow}$ the resistance in the state with opposite polarisation orientation.

Figure 2.9 shows the mechanisms causing the TER effect [36]. The inverse piezoelectric effect is based on the strain resulted from applying voltage on the barrier which is reversed with the polarisation orientation. Even though the piezoelectric coefficient is rather small (∼45 pC/V for PZT [40]), its contribution to the effective thickness can be important due to the exponential decrease of current through the barrier. Another mechanism is the interaction of the outermost ions in the barrier with the innermost ions in the electrode. The extent of the orbitals' overlap depends on the ferroelectric ions displacements and affects the density of states and thus the resulting tunnelling currents. In junctions with different electrodes, due to dissimilar electrode abilities to screen the surface charges, an electrostatic potential is created which adds to the barrier potential and alters its shape and height for the two orientations.

The electroresistance (ER) is caused by competing direct tunnelling, Fowler-Nordheim and thermionic injection mechanisms. The magnitude and sign of ER is determined by the dominating mechanism which depends on the applied voltage and barrier thickness as seen in figure 2.10 [41]. FNT appears to be dominating at high voltages ($> 1\ V$), while at low voltages a transition from direct tunnelling to thermionic injection occurs with increasing thickness ($d > 4$ nm). ER can also be optimised by using the electrodes screening abilities and their work function which influence the barrier height.

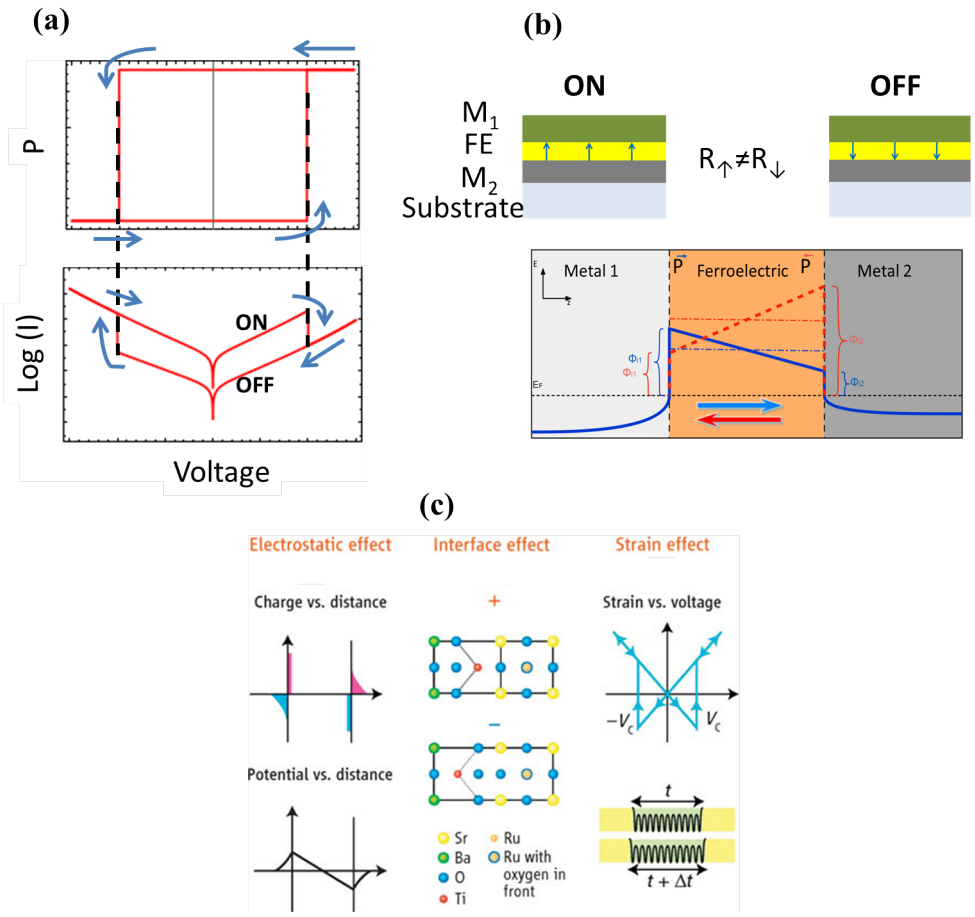


Figure 2.9: a) Ferroelectric $P(V)$ hysteresis (top) with corresponding resistance changes at the coercive voltage values (bottom); b) Schematics of changes in the barrier potential caused by polarisation switching which reflect on the resistance values in the two states; c) mechanisms leading to TER effect; adapted from [39].

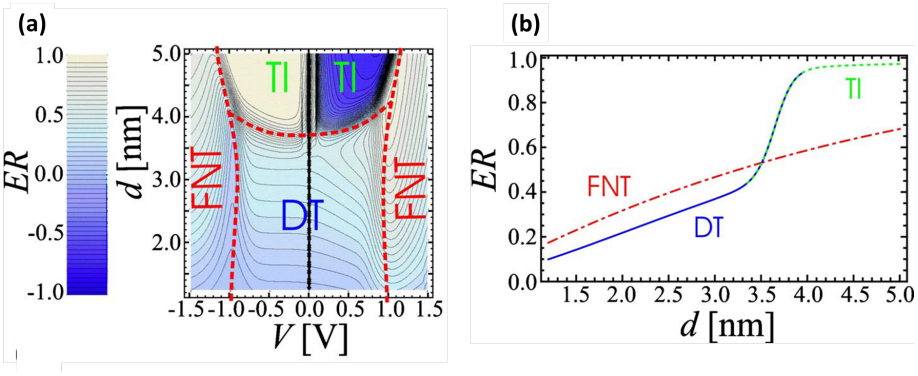


Figure 2.10: a) Tunnelling mechanisms contribution to the electroresistance (ER) with variation of applied voltage and barrier thickness, higlighting the transition regions; b) slice from the plot in a) representing the thickness dependence of ER at high (red dashed-dotted line) and low voltages (solid blue and green dashed lines); reproduced from [41].

## 2.5 Multiferroic tunnel junctions

Multiferroics are generally called the materials which present simultaneously two order parameters. Multiferroic tunnel junction (MFTJ) devices are based on ferromagnetic electrodes and ferroelectric barriers which would allow the control of both magnetisation and ferroelectric polarisation by electric and magnetic fields [39]. This type of device exhibit both TMR and TER effects and thus exhibit four resistive states. MFTJ are also the subject for fundamental studies due to the ferroelectric-controlled spin properties observed for some interfaces and which are not completely understood.

## 2.6 Materials used in multiferroic tunnel junction fabrication

In tunnel junctions highly oriented crystalline films are important in obtaining good physical properties; the lattice matching at the interfaces improves the overall performance of the devices. Particularly the quality of the barrier must be high to ensure the film is still ferroelectric at the small thickness characteristic to tunnelling junctions. High quality crystalline films can be obtained by pulsed laser deposition when choosing a suitable substrate and optimising the deposition parameters for each material, so epitaxial growth is obtained. The multiferroic tunnel junctions fabricated and investigated in this thesis are heterostructures as presented in figure 2.11 a: LSMO bottom electrode and PTO or PZO barriers grown on STO

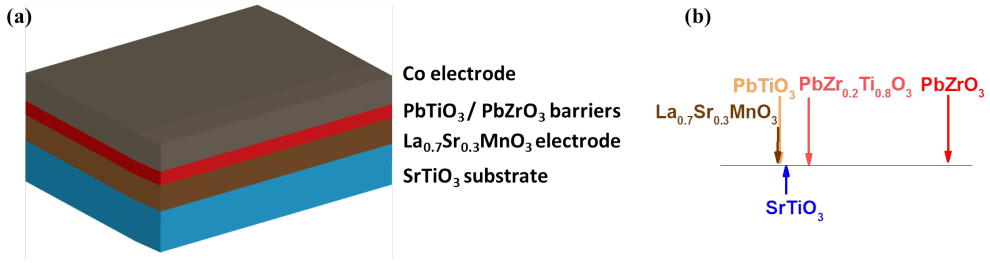


Figure 2.11: a) Schematics of the fabricated multiferroic tunnel junctions; b) schematics of in-plane lattice parameters of the STO substrate, pseudocubic LSMO electrode and the PTO, PZT and pseodocubic PZO barriers.

substrate with Co sputtered on top.

### 2.6.1 Strontium titanate ($SrTiO_3$) substrate

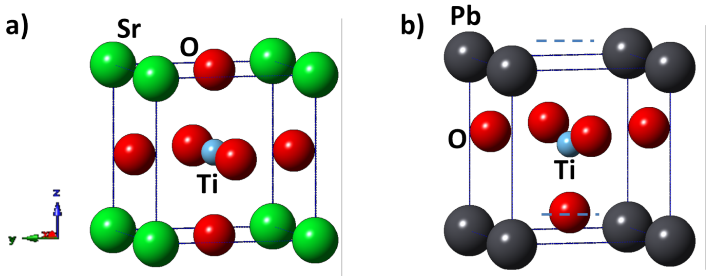


Figure 2.12: Representation of: a) STO, b) PTO unit cells [42] realised with CrystalMaker software using National Chemical Database Service [43].

Above T≃110 K, strontium titanate ($SrTiO_3$, STO) is a cubic perovskite with lattice parameter a= 3.905 Å (Figure 2.12) [43, 44]. STO is chosen as substrate to closely match the LSMO in plane lattice parameter ($a_{pc}$=3.889 Å), having a lattice mismatch, $f$, of 0.41% (calculated with Equation 2.36) which enables further layer-by-layer growth (Figure 2.11 b).

$$f = (a_{subst} - a_{film})/a_{subst} \tag{2.36}$$

Where $a_{subst}$ ($a_{film}$) is the in-plane lattice parameters of the substrate (film).
STO has diamagnetic properties with negligible effects on the deposited heterostructures properties [45].

### 2.6.2 Lanthanum strontium manganate ($La_{0.7}Sr_{0.3}MnO_3$) bottom electrode

LSMO is an oxide with a perovskite structure whose composition can be varied with the substitution of La ions (1-x) by Sr ions (x). The mixed valences $Mn^{3+}$ (corresponding to $LaMnO_3$) and $Mn^{4+}$ (corresponding to $SrMnO_3$) are caused by the different valence of the $La^{3+}$ and $Sr^{2+}$ ions. The resulting $Mn^{3+}/Mn^{4+}$ ratio affects both electric and magnetic properties of the material [46, 47]. The temperature of metal-insulator and ferromagnetic-antiferromagnetic transitions coincide in the case of single crystals and epitaxial thin films and can be significantly different depending on the grain boundaries and structural defects. Electric and magnetic properties can be affected also by other factors such as oxygen stoichiometry (effects on magnetic saturation moment and transition temperature), lattice strains (leading to magnetic anisotropy) and morphology [48, 49].
Field splitting and Jahn Teller effect on Mn ions are shown in figure 2.13. An isolated Mn ion has 5 available 3d orbitals which in an ideal cubic perovskite undergo a crystal field splitting resulting in a $t_{2g}$ triplet ($d_{xy}$, $d_{xz}$, $d_{yz}$) and an $e_g$ doublet ($d_{x^2-y^2}$, $d_{3z^2-r^2}$). In crystals with lower symmetry than cubic the degeneracy is lifted and is called Jahn-Teller distortion. Compositions x=0.3 or 1/3 Sr are common

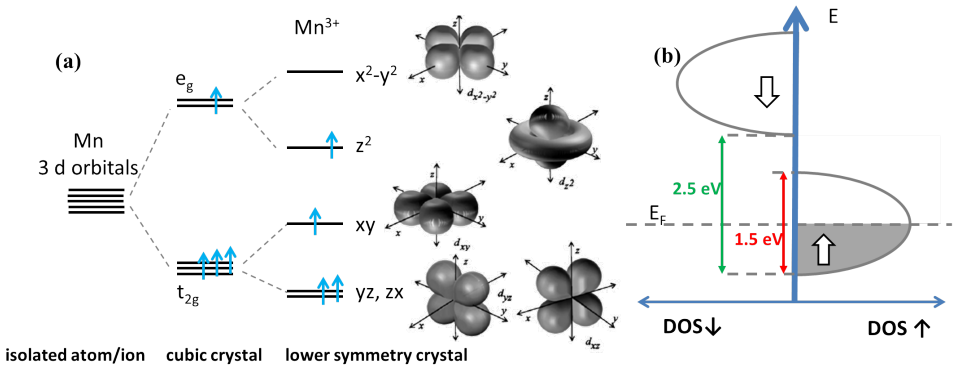


Figure 2.13: a) Schematic representation of crystal field splitting in $3d$ band energy levels: isolated manganese ion (left), an octahedral crystal field (middle) and a Jahn Teller distortion in the form of a tetrragonal crystal field (right) with the coresponding electron localisation surfaces of the orbitals; b) majority and minority spin bands characteristic to half-metals illustrated in $La_{2/3}Sr_{1/3}MnO_3$; adapted from [50, 51, 52].

in practice for obtaining LSMO with ferromagnetic and metallic properties. For x=0.3 the unit cell is rhombohedral with the lattice constants $a_r$=5.471 Å and $\alpha_r$=60.43$^o$ [53]. In two-dimensional growth on the STO substrate, the mismatch

compatibility between the two perovskites can make LSMO grow coherently, having a resulting orthorhombic unit cell which is generally regarded as a pseudocubic. LSMO is usually the material of choice in tunnelling devices because it enables the analysis of tunnelling electrons spin [54] due to its high spin polarisation (100% spin polarisation predicted, 95% determined by tunnelling experiments [55]). LSMO is therefore a half-metal which means it is a ferromagnet with no electrons on one of the two spin channels (Figure 2.13 b), giving it a semiconductor-like behaviour on one spin channel and metallic on the other one [56]. In LSMO this is caused by the relatively narrow majority spin band (1.5 eV) being separated from the minority spin band by a relatively high exchange energy (2.5 eV).
Transport mechanisms are determined by the exchange mechanism and the magnetic ordering by both super exchange and double exchange interaction between Mn ions through O ions [57, 58]. The double exchange process takes place when the parallel spin configuration is favoured, resulting in the transfer of one electron with the same spin orientation from one Mn atom to another, while the super exchange results in the transfer of an electron with antiparallel spin. By substitution of La with Sr, the material is practically doped with holes and exhibits ferromagnetic properties at charge densities of $\sim 10^{21}$ holes/cm$^3$ [59]. The screening length is 2-3 Å [60], larger than in metals.

### 2.6.3 Ferroelectric lead zirconium titanate $PbZr_{0.2}Ti_{0.8}O_3$

Lead zirconium titanate ($PbZr_xTi_{1-x}O_3$, PZT) is a solid solution of $PbTiO_3$ (PTO) and $PbZrO_3$ (PZO). At x=0.2, due to the low Zr content, its properties resemble more closely to those of PTO (Figure 2.14). The materials crystallize in a perovskite structure. PZT is tetragonal (ferroelectric) at room temperature with lattice parameters $a$=3.935 Å and $c$=4.135 Å up to $T_C \sim 480\ ^oC$ and above that, it becomes cubic (paraelectric). Characteristic of a perovskite structure, the spontaneous polarization is due to the shift of the ions in the unit cell. The high value of the polarization (105 $\mu$C/cm$^2$ [40]) is the reason it is preferred in studies on ferroelectric and multiferroic tunnel junctions [61].

### 2.6.4 Ferroelectric lead titanate ($PbTiO_3$)

Lead titanate ($PbTiO_3$, PTO) is ferroelectric (FE) at room temperature with large spontaneous polarisation of $\sim$94 $\mu$C/cm$^2$ [64]. PTO is tetragonal with in plane lattice parameter a=3.894 Å and c=4.140 Å and goes through a tetragonal (ferroelectric)-cubic (paraelectric) phase transition at $T_C \sim 490^oC$. The shift of the O, Ti and Pb

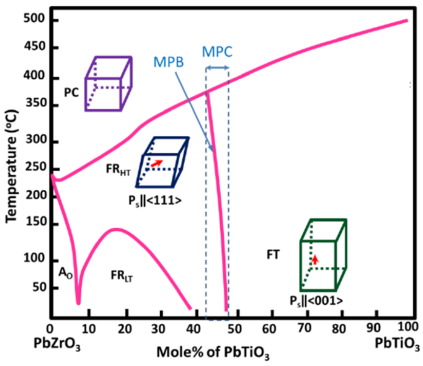


Figure 2.14: PZT phase diagram highlighting the structure and Curie temperature dependence on the composition, where $A_O$: antiferroelectric orthorhombic; PC: paraelectric cubic; $FR_{HT}$: ferroelectric rhombohedral at high temperature; $FR_{LT}$: ferroelectric rhombohedral at low temperature; FT: ferroelectric tetragonal, MPB: morphotropic phase boundary and MPC: morphotropic phase composition; reproduced from [62, 63]

ions causing ferroelectricity in the tetragonal unit cell is seen in figure 2.12 b. PTO is also ferroelastic with tetragonal $c/a$ strain of 6%, higher than typical ferroelastic materials [65]. This property is structure-dependent and is characterised, similar to ferroelectricity, by a spontaneous macroscopic strain that can be switched to another state with the application of mechanical stress [66, 67].

### 2.6.5 Antiferroelectric lead zirconate ($PbZrO_3$)

$PbZrO_3$ became technologically important due to its antiferroelectric (AFE) properties. PZO crystals typically have temperature, field and thickness-induced AFE-FE phase transitions. PZO is AFE (orthorhombic centrosymmetric) at room temperature with lattice parameters $a$=5.88 Å, $b$=11.787 Å and $c$=8.231 Å (Figure 2.15). The approximation of the lattice with a pseudocubic unit cell having $a_{pc}$=4.14 Å is also common. The antiferroelectric axis lies in the $ab$-plane and is caused by antiparallel pairwise shifts of the Pb ions accompanied by a $ZrO_6$ octahedra rotation. PZO becomes FE (orthorhombic noncentrosymmetric) at low temperatures and paraelectric (cubic) above ∼505 K. Under an applied electric field exceeding a threshold value, a structural transition from orthorhombic AFE to rhombohedral FE takes place due to the small energy difference between the two phases. In the case of thin films, room temperature FE was observed below critical thicknesses, depending on the system they were grown in [68, 69, 70].

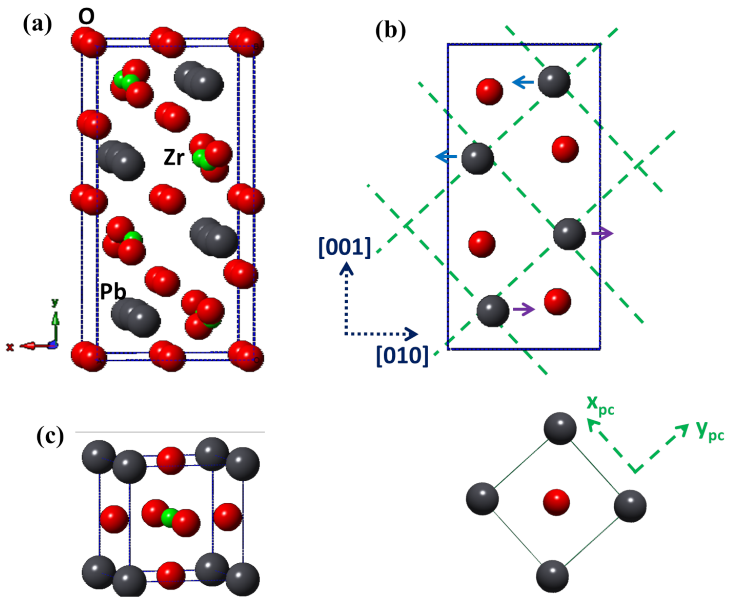


Figure 2.15: a) PZO orthorhombic unit cell; b) projection highlighting the displacements of Pb ions and the pseudocubic unit cell and c) pseudocubic unit cell of PZO; adapted from [71].

### 2.6.6 Cobalt top electrode

Cobalt is a ferromagnet with a very high Curie temperature ($T_C$ ~1400 K in bulk). The work function of pollicrystalline Co is 5.0 eV, depending also on the interface distribution of crystalline facets [72]. The Thomas-Fermi screening length was calculated 1.5 Å in hexagonal Co [73]. When exposed to air, Co oxidises forming antiferromagnetic CoO with a Neel temperature of ~293 K.

## 2.7 Summary

The quantum tunnelling process is presented as generally treated by quantum mechanics textbooks, then its practical importance is illustrated in real devices such as magnetic and ferroelectric tunnel junctions. Multiferroic tunnel junctions are proposed with LSMO and Co magnetic electrodes and PTO and PZO barriers grown on STO substrate and the relevant properties of the used materials are briefly presented. The mechanisms leading to the TMR and TER effects are illustrated in parallel with the physical properties of the materials that causes them. The TER and TMR effects, together with the junction resistance, yield the performance of the device and its applicability in memory circuits. The magnetoelectric coupling between

the ferromagnetic electrodes and ferroelectric barrier can give rise to multiferroic-like interfaces which are not yet completely understood and which will be treated experimentally in the following chapters for the chosen systems.

# Chapter 3

# Experimental methods

In this chapter the experimental techniques used in the study of tunnel junctions are presented, starting from the fabrication process to determination of the electric and magnetic properties. The equipment used in the film growth process is described to illustrate the control of the deposition parameters and how these can affect sample properties. The working principles of the equipment used for characterisation are briefly described in order to highlight the relevant information obtained on the systems under study. This is essential for determining the quality of the films and interfaces and characteristics which determine the device properties and to help understanding the experimental results.

## 3.1 Thin film growth

### 3.1.1 Pulsed Laser Deposition (PLD)

Tunnel junctions require high quality interfaces and films which can be obtained with pulsed laser deposition (PLD); a physical deposition method successfully used in fabrication of complex oxides with different structures and functionalities. PLD was used for growth of the $La_{0.7}Sr_{0.3}MnO_3$ bottom electrode and the $PbTiO_3$ and $PbZrO_3$ barriers due to its simple working principle and operation resulting in stoichiometric transfer. A high powered UV laser ablates a target forming a plasma plume which transfers material to a substrate placed opposite the target. A schematic of the PLD deposition set-up is shown in figure 3.1. A PLD vacuum chamber generally includes the target holders which can be rotated or raster-scanned and the substrate heater with temperature controller. It is also connected to vacuum pumps to enable base pressures lower than $10^{-6}$ mbar, gas supplies by valves and pressure gauges that monitor and control partial pressure during deposition.

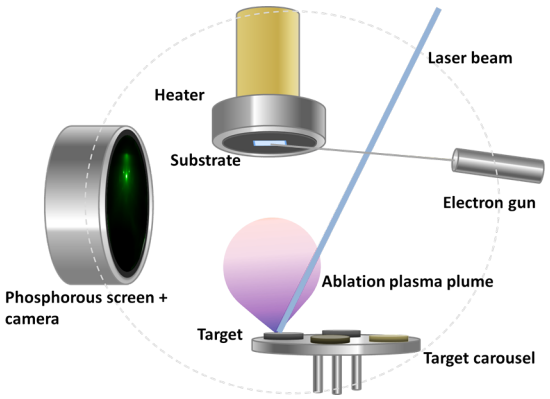


Figure 3.1: PLD chamber and RHEED setup illustrating the laser beam ablating the target and depositing material to the substrate. During the deposition, the electron beam is oriented on the substrate surface and creates a diffraction pattern on the phosphor screen.

The laser beam is directed by a system of mirrors and focused with a convergent lens onto the target surface. The use of apertures and attenuators helps to obtain a homogeneous spot with the optimum energy density. During the deposition process, the laser is focused on a rotating target and ablates material within the laser spot (typically for 10-50 ns). The electromagnetic energy of the laser converts to electronic excitation, thermal, chemical and mechanical energy leading to a highly directional expulsion of particles from the target by ablation and other simultaneous processes such as evaporation, excitation, plasma formation and exfoliation. The plume spreads normal to the target surface and is confined by the background gas, causing atoms, molecules, electrons, ions, clusters and sometimes even micron-sized particles to transfer to the substrate. Depending on the surface mobility and film-substrate lattice mismatch, further growth occurs through rearrangement [74, 75]. Three growth modes can be observed on flat surfaces (Figure 3.2): layer-by-layer (Frank-van der Merwe), island (Volmer-Weber) and both layer and island (Stranski-Krastanov). The deposition process depends on the laser characteristics as well as on optical, topological and thermodynamic properties of the target material. The laser pulse energy density, frequency, gas pressure, substrate temperature and substrate-target distance are all parameters that influence the quality of the deposited film and need optimising until the desired structure and properties are achieved. PLD can also present disadvantages such as macro-particle deposition, though that can be overcome by carefully selecting the deposition parameters. While growth on small areas ($5\times5$ mm$^2$) has been sufficient for academic research, up-scaling of PLD was forced by industry requirements and nowadays films can be deposited even on

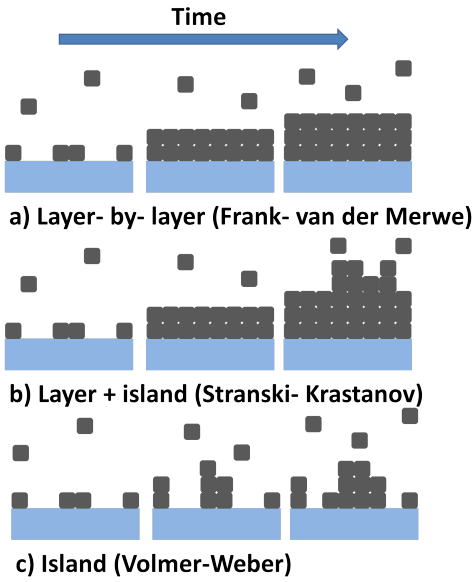


Figure 3.2: Representation of the deposition and growth illustrating differences in growth modes: a) layer-by-layer (Frank-van der Merwe); b) layer + island (Stranski-Krastanov) and c) island (Volmer-Weber).

200 mm diameter wafers [76, 77]. The high deposition rate and stoichiometric deposition characteristics of PLD are extremely useful in obtaining oxides films with complex structures. However volatile elements are an exception and to compensate for the lack of stoichiometry, it is usual to have them in excess in the target materials ($Pb_{1.1}TiO_3$ targets for obtaining $PbTiO_3$ film) or use them as background gas ($O_2$ for oxides, $N_2$ for nitrides).

### 3.1.2 Reflection High Energy Electron Diffraction (RHEED)

PLD is a more powerful tool when combined with reflection high energy electron diffraction (RHEED) which helps monitoring of the film growth *in situ* in real time. An electron gun emits electrons that scatter from the surface of the sample creating a diffraction pattern on a phosphor screen as pictured schematically in figure 3.1 and 3.3. Due to the high energy electron beam (10-50 keV) that reaches the surface under a grazing incident angle ($0.1° - 5°$), the electrons interact only with the topmost atomic layers (1-2 nm depth), making the method very sensitive to the surface and therefore to changes during film deposition. The Ewald sphere is a geometrical construction that provides the relation between the orientation of a crystal and the direction of the beam diffracted by it and can be used in understanding how the RHEED pattern is produced and the information it offers (Figure 3.3).

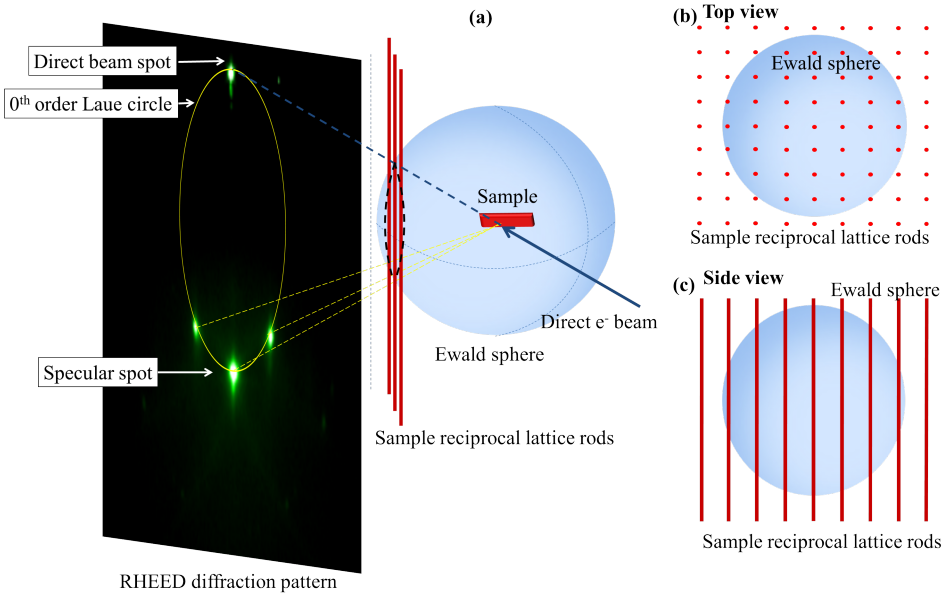


Figure 3.3: a) Diffraction conditions shown in reciprocal space by the intersection of the Ewald sphere of the electron beam with selected sample reciprocal lattice rods creating the 0th order Laue circle; b) top view and c) side view of the Ewald sphere and reciprocal lattice rods of the sample.

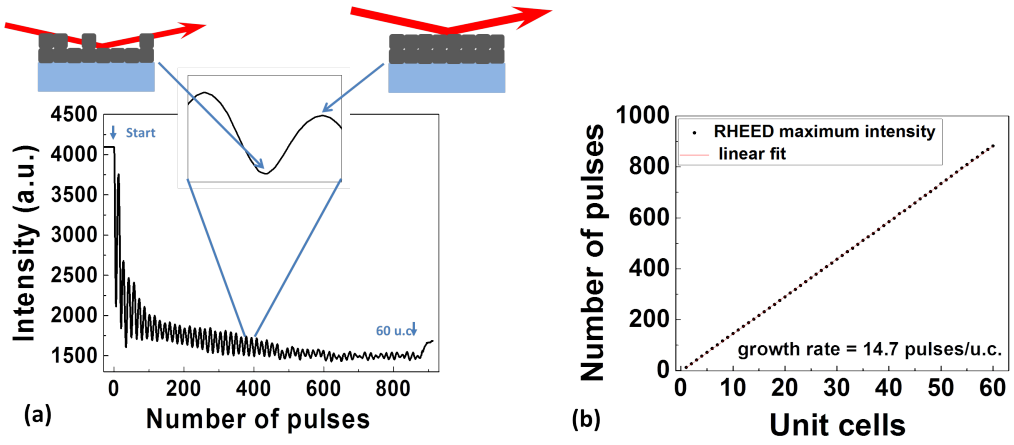


Figure 3.4: a) RHEED specular spot intensity showing oscillations corresponding to $La_{0.7}Sr_{0.3}MnO_3$ layer-by layer growth; the moments where the laser started and stopped ablating are marked; b) Determination of the deposition rate from the number of deposited unit cells variation with the number of ablation pulses.

The electron beam is represented by the Ewald sphere with radius $r$ equal to the reciprocal wavelength $\lambda$ associated to the electrons ($r = 2\pi/\lambda$) and with the centre on the sample surface. The direction of the incident beam is along the radius of the sphere and depends on the chosen incident angle. The reciprocal space lattice of a two-dimensional sample is a lattice of infinitely thin rods perpendicular to the surface corresponding to ($hk0$) planes. Diffraction conditions are met where the Ewald sphere intersects the rods. For perfect surfaces the diffraction spots form concentric circles called Laue circles for which the radius increases with the diffraction order. The 0th diffraction circle corresponds to the smallest radius and is determined by the specular (mirror) reflected beam. A one-dimensional map is obtained by projection on the phosphorus screen and captured by a digital camera. Kikuchi lines originating from the diffuse scattering of electrons can be observed connecting the intense diffraction points. Clear and sharp Kikuchi lines typically describe flat and crystalline surfaces. Information on the dynamics of the growth process is determined in real time from changes in the RHEED pattern and variation of the specular spot intensity during the deposition. Layer-by-layer growth exhibits oscillations of the intensity associated with stages of the layer formation. Maxima in the intensity mean smooth surfaces and indicate the completion of the layer, and minima in the intensity denote rougher surfaces due to the existence of incomplete layers (Figure 3.4 a). The increase in intensity after ending the laser ablation indicates the surface becomes smoother through adatom rearrangement. Based on the specular spot monitoring, the growth rate can be accurately determined as shown in figure 3.4 b for 60 layers of LSMO.

### 3.1.3 Co top electrode sputtering

After the PLD process the samples were immediately transferred to a chamber which has a magnetron sputtering unit for Co electrode deposition. This method is based on the irradiation of a cathode target material with highly energetic cations which eject atoms, molecules and clusters towards the anode substrate [78]. A polycrystalline film was obtained at room temperature in $2.5 \times 10^{-3}$ mbar Ar with 20 W magnetron power.

#### Co electrode patterning

The tunnel junction devices were patterned using photolithography, a process where a pattern present on a mask is transferred onto a substrate by means of UV illumination as described in figure 3.5 [79, 80]. Masks are generally quartz plates,

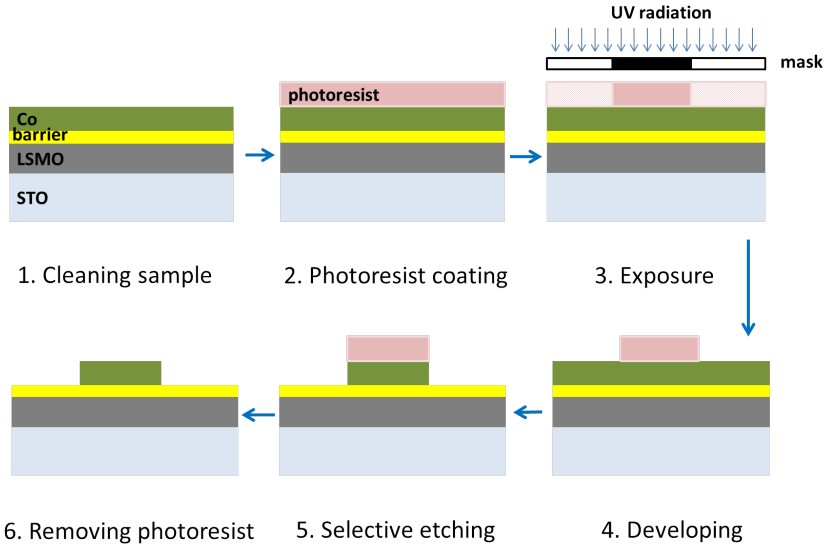


Figure 3.5: Steps in the patterning process of the Co top electrode: photolitography and wet etching.

transparent to UV with a non-transparent chromium defined pattern which enable reproducing the pattern with a resolution roughly equal to the wavelength of the exposure source. The process begins with a UV-sensitive polymer (photoresist) being spin coated onto the samples and baked allowing the solvents to degas, thus the photoresist hardens. In a mask aligner, the substrate is brought close (in contact) with a mask and exposed. A positive (negative) photoresist is more soluble on the exposed (unexposed) areas and can be removed during the developing step. In the present case, lithography is used to shape the $40\times40$ $\mu$m$^2$ area devices, using the positive photoresist for both accurately patterning the top electrodes and protecting them during the wet etching of Co. The samples are immersed in $NH_3$ solution, etching just the unprotected Co areas. Finally the remaining photoresist is removed with organic solvents.

## 3.2 Surface characterisation

### 3.2.1 Atomic Force Microscopy (AFM)

Properties of the tunnel junctions depend strongly on the quality of the interfaces. To ensure high quality and reproducibility of the fabricated devices, the surfaces are analysed before and after film depositions with an atomic force microscope (AFM); a common tool for topographic mapping. Following the film depositions, insights

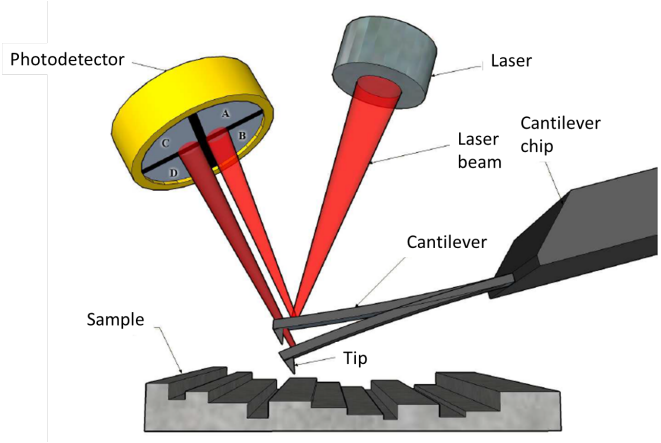


Figure 3.6: Atomic force microscopy principle- reproduced from [81].

on the growth process (roughness of the surface, presence of terrace steps, existence of incomplete layers) can be offered by AFM. During the acquisition the surface is scanned with a very sharp probe placed at the end of a flexible cantilever. Changes in repulsive/attractive forces occurring between the surface and the tip cause vertical and lateral deflection of the cantilever which is monitored by means of a laser beam reflecting off its back onto a four-quadrant position sensitive photodiode (Figure 3.6). AFM provides information on three-dimensional surface features with typical height range of 8-10 $\mu$m with sub-nanometre resolution and lateral range up to $\backsim$100 $\mu$m with resolution given by the radius of the tip ($<$100 Å) [82]. The height sensitivity makes it suitable for distinguishing step terraces that differ even by half to one unit cell ($\sim$0.4 nm) present on the $SrTiO_3$ substrate.
AFM can be used in 3 different modes: non-contact, contact and tapping (intermittent contact) mode; only the latter two were used for characterization in this thesis. The resulting images were processed using the Nanotec WSxM 5.0 software [83]. AFM has been developed to function in certain modes such as magnetic force microscopy or piezoresponse force microscopy in order to obtain also physical properties of the materials.

### Piezoresponse force microscopy (PFM)

Piezoresponse force microscopy (PFM) is essentially a contact-mode AFM where a bias is applied on a conductive tip and represents an essential tool in nondestructive imaging of polarisation domains and testing ferroelectric properties of materials at nanoscale [84, 85]. In this thesis it was used to determine the ferroelectricity of the PTO ultra-thin films and the value of the critical thickness when ferroelectrcity

vanishes. PFM uses AFM in contact mode and detects mechanical deformations (of the order of ∼picometers) of materials under applied electric fields by using the converse piezoelectric effect. During the scanning, an ac voltage is applied through the tip and the amplitude and phase of the resultant displacement is recorded. Typically it can offer information on ferroelectric polarisation by imaging the amplitude and phase signal of a certain area and by voltage spectroscopy (local hysteresis loop measurements). Within PFM spectroscopy the sweep of a large applied bias voltage causing the polarisation to switch under the tip overlaps with a high frequency small amplitude bias voltage $V_{ac}$. The resulting local piezoelectric response is measured and provides information on the switching process (Figure 3.7). Due to the large difference between the signals associated with the topographical features and the small piezoelectric signal from the sample, the overall signal is processed through lock-in amplifiers and then the amplitude and phase images are obtained. Contrast in the phase image is obtained from the offset of the output compared to the input. The PFM experiments in this study were performed on the ferroelectric barrier surface with the conductive AFM tip as top electrode using an Asylum MFP3D-SA system. The sensitivity of the thin films is low and cannot be measured with a small voltage without switching the polarisation or damage the sample. Alternatively, PFM was used in dual ac resonance tracking (DART) mode where a dual excitation is applied on the cantilever. The frequencies of the applied voltages are at or near the contact resonance in order to improve the PFM signal and help in tracking changes in the resonance frequency, reducing the topographic crosstalk.

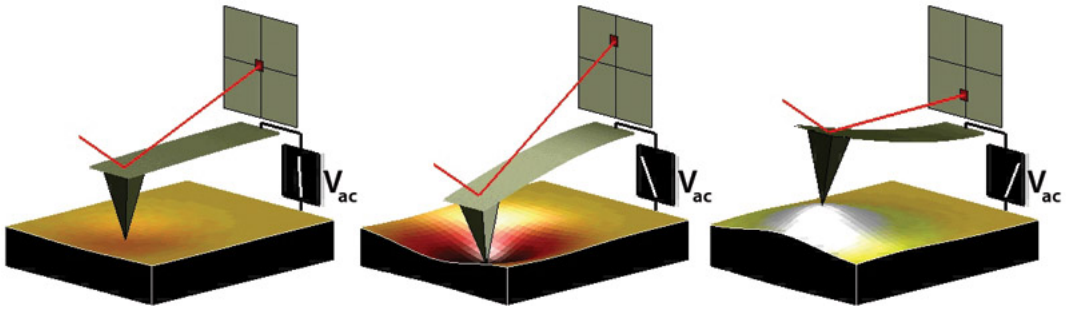


Figure 3.7: PFM detection of the deformation resulting from the inverse piezoelectric effect- reproduced from [86].

## 3.3 Structural characterisation

The structure of a film can be different from the structure of the bulk target from which it was deposited due to the influence of the film/substrate interface and to

unique size effects given by its thickness. Structural characterisation is therefore important in the fabrication process for structure and quality analysis of the resulting heterostructures and leads to better understanding of their functional properties. The structure of the deposited films was investigated using a Philips Panalytical X'Pert Pro MRD X-ray and Phillips X'Pert MRD- type 3050/65 diffractometers, both with wavelength characteristic to copper $K_{\alpha 1}$ line, $\lambda_{K\alpha 1} = 0.1541$ nm. The macroscopic characterisation was combined with local characterisation, micrometric samples were fabricated by focused ion beam using Jeol 4500 SEM/FIB. The resulting lamellas were imaged by transmission electron microscopy (TEM) using Jeol ARM 200F.

### 3.3.1 X-Ray Diffraction (XRD)

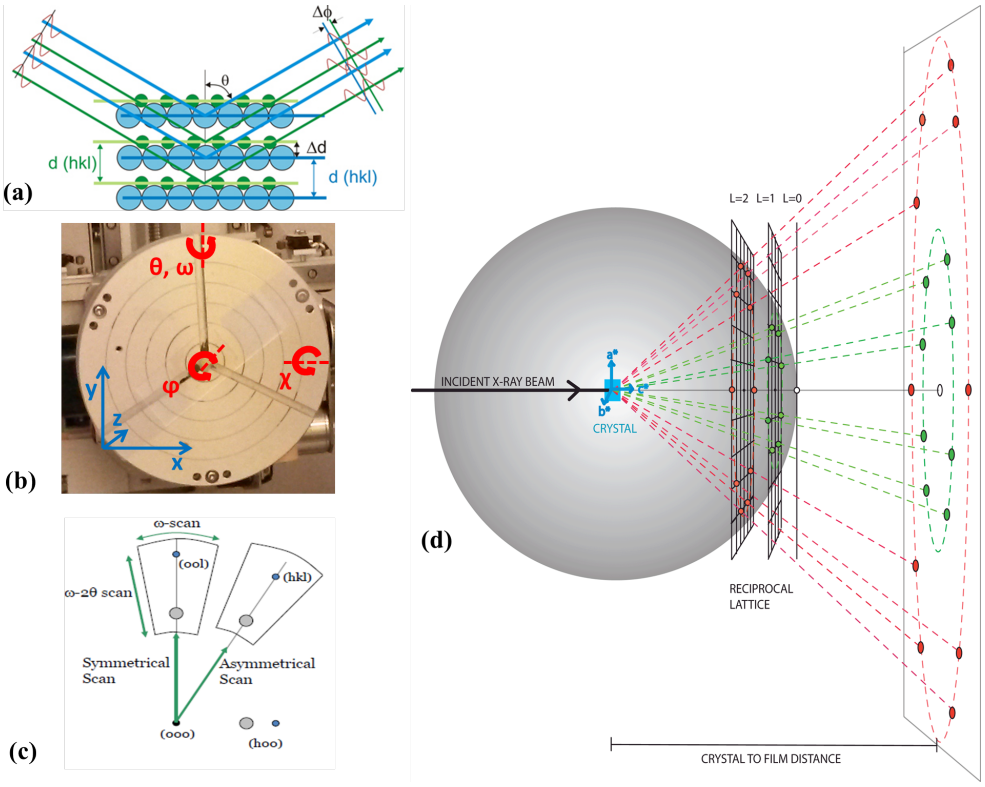


Figure 3.8: a) Diffraction (reflection) process on parallel atomic planes; b) possible rotations of sample position in XRD; c) RSM scans principle and d) RSM measurement principle involving the Ewald sphere and reciprocal lattice of the sample.

X-ray diffraction (XRD) is a common characterisation technique that uses elastic scattering of X-rays to provide information about quality, structure, preferred orientation and composition of crystalline materials. When the incident X-ray radi-

ation interacts with the crystal, its unique periodic arrangement of atoms gives rise to scattered waves which create diffraction patterns characteristic to the material. Sharp intensity peaks are measured when waves are scattered by sets of parallel lattice planes and interfere constructively, satisfying Bragg's law (Figure 3.8 a):

$$n\lambda_{K\alpha 1} = 2d_{hkl}\sin\theta, \tag{3.1}$$

where $n$ is the diffraction order, $\lambda$ is the X-ray wavelength, $d_{hkl}$ is the spacing between consecutive planes with $hkl$ indices and $\theta$ is the angle made by the X-ray beam with the lattice planes of the crystal.
The position of the sample relative to the radiation direction can be modified by rotation ($\omega$, $\phi$, $\chi$) or shift (x, y, z directions) for aligning purposes, gaining access to different ($hkl$) planes and setting up different measurement types (Figure 3.8 b and c). Symmetric ($00l$) $\omega - 2\theta$ scan is a basic measurement performed on the samples. For films with appropriate thickness, the resulting diffractogram is useful in identifying the peaks from substrate and films and determining the out of plane lattice parameter. In order to investigate the epitaxial relationship between the grown films and substrate, reciprocal space maps were performed around selected diffraction planes. Asymmetric peak scans offer information about both in plane and out of plane lattice parameters thus on the degree of strain and relaxation of the films on the mismatch substrate. Ewald sphere construction can also be employed in the case of X-rays to explain graphically the reciprocal space map (RSM) principle (Figure 3.8 d). The ($hkl$) sample planes are represented as points in reciprocal space with the origin intersecting the sphere. For each reciprocal lattice point lying on the sphere surface the diffraction condition is satisfied and it is recorded on the diffraction pattern using an area detector.

### 3.3.2 Transmission Electron Microscopy (TEM)

XRD and RHEED use large sampling volumes and areas offering an average description of the entire sample and are best used in combination with local structural characterisation. The latter helps in detecting the quality of the grown films, lattice parameters, displacement of ions within the unit cell and possible defects at nanoscopic scale. For this purpose, transmission electron microscopy (TEM) was used. This technique consists of imaging the projection of very thin cross sections of the bulk samples (<100 nm) while irradiated with an electron beam of uniform current density. One of the operating modes is conventional TEM when the intermediate lens focuses on the image plane of the objective lens and the resulting image

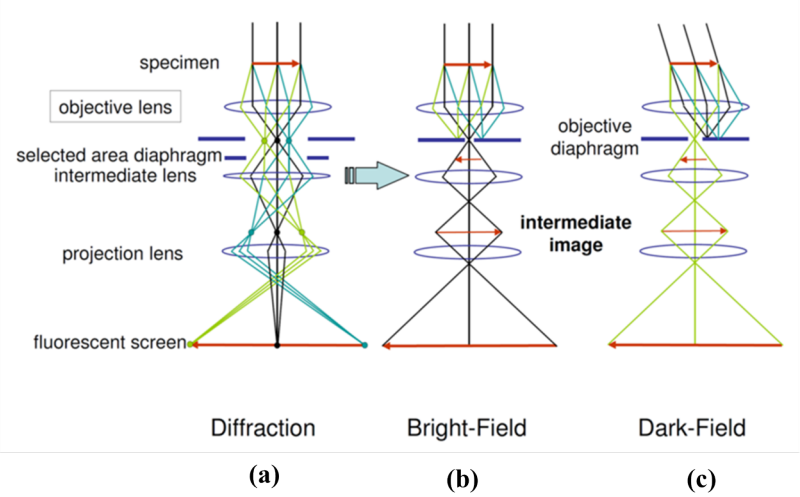


Figure 3.9: Electron ray path in TEM in: a) diffraction; b) bright field and c) dark field modes, depending on the diaframg and lens settings; reproduced from [89].

is a combination of all transmitted and diffracted electron rays with low contrast. Bright-field and dark-field modes can be selected by placing an objective aperture in the back focal plane of the objective (Figure 3.9). When it allows the transmitted beam to pass, a bright-field image is obtained and when it allows the diffracted beam to pass, a dark-field image is obtained. During the transmission process, electrons are scattered due to nuclear interactions depending on the atomic number $Z$ and specimen thickness giving rise to the mass-thickness contrast: thick and/or high $Z$ atom areas appear darker than thinner and/or lower $Z$ atom areas in a bright-field image, while the opposite is valid for dark-field images [87]. Annular bright field (ABF) and annular dark field (ADF) were combined to obtain both light and heavy atoms columns position with picometer accuracy [3]. Acquisition, image processing and numerical analysis were made using the Gatan Inc Digital Micrograph 3.0 software. More experimental details are available in [88].

Generally, information on crystal lattice, orientation and defects in the structure can be obtained from the diffraction pattern, using the electron diffraction mode (selected area electron diffraction). In this case, the intermediate lens is focused on the back focal plane and an intermediate aperture is positioned in the image plane of the objective lens, analysing a relatively small area of the specimen. The selected area is larger than the size of the films used in this study and does not allow their separate analysis.

The quality of TEM samples is very important in obtaining qualitative images and reliable numerical results. Samples suitable for TEM imaging are electron transpar-

ent. Cross sections of the films can be obtained through the classical method by cutting the macroscopic sample with a diamond wire saw, grinding and polishing it using SiC abrasive paper and finally performing ion milling. The advantage of this method is time efficiency since more samples can be ground and polished simultaneously and competes with its main inconvenience of destroying most or the entire $5\times5$ mm$^2$ sized samples under study. Cross section lamellas can also be obtained in a more controlled and non-destructive manner by focused ion beam (FIB) combined with scanning electron microscopy (SEM) which affects only a reduced area of the sample surrounding the lamella fabrication site. Platinum, tungsten or carbon depositions on the surface are usually performed for mechanical protection and to avoid charge build-up. A dual beam Jeol 4500 FIB/SEM was used in order to fabricate the TEM specimen: milling using $Ga^+$ ion beam and imaging with the electron beam. A lamela is cut from the bulk, lift out from the sample and attached to a TEM grid where it is further thinned down to electronic transparency and polished to remove amorphous material with decreasing ion beam current and accelerating voltage [90].

## 3.4 Magnetic and electric characterisation

### 3.4.1 Vibrating Sample Magnetometer (VSM) and Superconducting Quantum Interference Device (SQUID)

The macroscopic magnetic properties of the electrodes determine the tunnelling properties measured in the microscopic tunnelling devices. Oxford Instruments vibrating sample magnetometer (VSM) and Quantum Design MPMS-5S superconducting quantum interference device (SQUID) magnetometer were both used for investigating the samples dependence of the magnetic moment on temperature, $m(T)$ and field, $m(H)$.

The working principle of VSM is based on electromagnetic induction. The vibration of a magnetic sample produces changes in the magnetic flux inducing a voltage across the terminals of the pick-up coils which is proportional to the magnetic moment of the sample. The VSM presents the advantage of fast measurements due to continuous data acquisition while sweeping the magnetic field. In the case of SQUID magnetometer, the principle is similar to VSM, but the sample is moved more slowly in a number of discrete steps within a length of a few centimetres. The flux change is detected by coils formed from a single superconducting wire. Thin films as well as other samples with weak magnetic response are typically measured using SQUID magnetometers due to their higher sensitivity ($10^{-7}$ emu) compared

to VSM ($10^{-5}$ emu) [91]. Shifts on the horizontal axis of the hysteresis loops can occur due to small trapped fields in the superconducting magnets. When possible, degaussing sequences were run before the measurements to minimize them and resulted in residual values of the order of a few Oe. They can still be significant in the hysteresis measurements, considering the bottom LSMO electrode is a soft ferromagnet ($H_c \sim 20$ Oe at 10 K and $\sim 6$ Oe at 300 K). For this reason the magnetic characterisation will be considered for qualitative analysis only [92].
In the case of the grown heterojunctions, the total magnetic moment measured with VSM and SQUID magnetometers corresponds to the thin film and background (sample holder, substrate, other films). In the simple case of a paramagnetic or diamagnetic linear signal which is weaker than the film signal, it can be detected at fields higher than the saturation field of the film and using the $m(H)$ slope can be extracted from the total magnetic moment. When that is not the case, the extraction procedure can be more complex [93, 94]. When conducting measurements with VSM and SQUID magnetometers, running a separate measurement and performing an extraction of the sample holder and substrate signal is recommended. There is still no universal approach on how this should be performed, but the available options involve measuring the sample holder with an identical substrate; or the sample holder with the same substrate either before film deposition (measuring substrate, then depositing the film and measuring the resulting sample) or after the deposition (measuring sample containing the substrate and deposited film, then removing the film and measuring the remaining substrate).

### 3.4.2 Physical Properties Measuring System (PPMS)

The dependence of transport properties on magnetic field and temperature were determined with a Quantum Design physical properties measurement system (PPMS). A rotator sample rod was used to rotate the samplee inside the PPMS allowing measurements with the magnetic field oriented in plane (perpendicular to the current) and out of plane (parallel to the current). The Quantum Design set-up makes PPMS a useful tool for investigating the LSMO metallic properties due to the built-in current source and was used for Van der Pauw LSMO sheet resistance measurements. Current-voltage ($I(V)$) curves can be used to evidence the two resistive states corresponding to the polarisation orientations which represent the TER effect. The tunnelling barrier profile can be obtained from fitting the data with tunnelling model equations presented in the previous chapter. The hardware is unsuitable for the high resistance characteristic of tunnelling devices where a voltage source is needed to keep the samples in tunnelling regime. Therefore for magneto-resistance and

electro-resistance acquisition the PPMS was used to control the temperature and magnetic field, and the transport measurements were performed externally using a Keithley 2635 source-meter. Pulses for switching the polarisation orientation were applied using a Tektronix AFG 3102 function generator.

### 3.4.3 Cryoprober

The junction magnetoresistance was investigated using a TTP4 Lake Shore cryogenic probing station containing a superconducting magnet which creates a magnetic field oriented in the plane of the sample. During the electric measurements the voltage was applied between the LSMO bottom electrode contacted to the copper sample holder and the Co top electrode patches in contact with the probe tip. Magnetoresistance measurements, switching and $I(V)$ curves were acquired by TestPoint software controlling a sourcemeter and also an arbitrary function generator used for switching the polarisation direction in the ferroelectric barriers.

### 3.4.4 Ferroelectricity testing

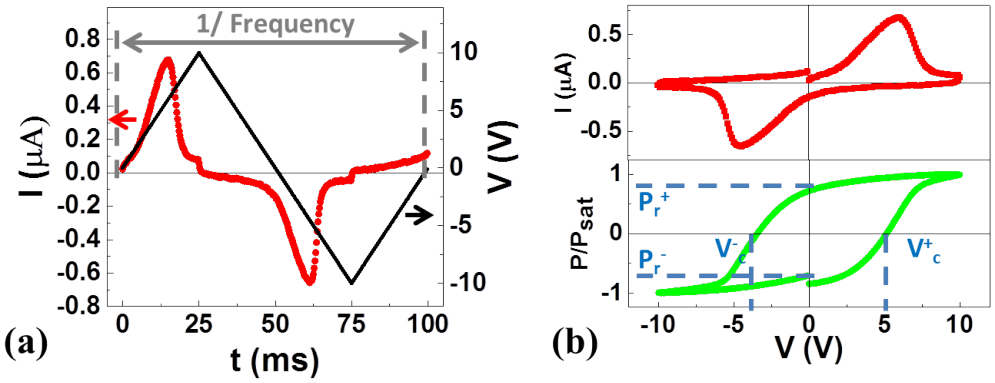


Figure 3.10: a) Transient current in a ferroelectric capacitor and triangular voltage applied during ferroelectricity testing; b) switching current-voltage (red) and polarisation-voltage (green) hysteresis loops measured in a LSMO/PZT/Cu capacitor, illustrating the coercive field and remnant polarisation values.

In the case of films with switching currents higher than the tunnelling currents, the ferroelectricity and/or antiferroelectricity can be investigated by using aixACCT TF 1000 and 2000 analysers which measure the ferroelectric polarisation. This characterisation was possible for films thicker than tunnelling barrier thickness. The values of the coercive voltage, remnant and saturation polarisations can be determined from the resulting polarisation-voltage $P(V)$ loops. A triangular pulse,

shown in figure 3.10 a, is applied after pre-polarizing the sample with an identical pulse. As shown in figure 3.10 b, for a 60×60 $\mu m^2$ $La_{0.7}Sr_{0.3}MnO_3/PbZr_{0.2}Ti_{0.8}O_3$/ Cu device, the measured transient current in ferroelectrics present two peaks corresponding to the switching of the polarisation direction at the coercive fields.

## 3.5 Summary

The methods used in obtaining high quality tunnel junction devices and in their characterization are presented. The aim is to help understand the importance of growth monitoring, the reasons behind the use of different analysis techniques and to detail how the experimental results presented in the next sections were obtained. By using PLD combined with *in situ* RHEED monitoring in real time it is possible to obtain epitaxial films and atomically sharp interfaces which are essential when growing such thin films. When studying devices at the nano-scale, the structure, quality of interfaces and defects can influence device properties, therefore a detailed characterisation is necessary to ensure their functionality and the reproducibility of the results.

The performance of the MFTJ was investigated from a magnetic and electric point of view. The magnetic properties of the ferromagnetic electrodes dictate the behaviour of the MTJ, while the ferroelectricity of the barrier is the defining characteristic of FTJ. Though conventional TF Analyser measurements were not easily applied to the measurement of ferroelectricity in tunnel devices due to typically low thickness, it was evidenced locally by PFM analysis. The study of TER and TMR effects are driven by possible 4-state memory applications and are at the base of fundamental study helping to understand the observed tunnelling effects.

# Chapter 4

# Fabrication and characterisation of multiferroic tunnel junctions

The fabrication process is important for the resulting properties of the tunnelling devices starting with the surface of the substrate to the patterning of the devices. The structure of the films deposited by PLD adapts to the substrate lattice during the epitaxial growth which can lead to properties different from the bulk material. Moreover, the very existence of electrodes (having imperfect screening abilities) and interactions of the ions (overlapping of $d$ orbitals leading to hybridisation) at the ferroelectric/ferromagnet interfaces can influence the overall behaviour of the device. To help in understanding how the fabrication processes affect the device properties presented in the experimental chapters, the films are characterised after the main processing steps.

## 4.1 $SrTiO_3$ substrate treatment

In order to offer reliable information on electronic properties of the interfaces, tunnelling junction devices should present atomically abrupt interfaces between constituent layers. High quality samples can be obtained by starting the fabrication with substrates having atomically flat surfaces. This results in subsequent layer-by-layer film growth and reproducible samples. As stated in the first chapter, the STO substrate was chosen due to its small lattice mismatch with the LSMO and PTO films used for bottom electrode and barrier, respectively; leading to their epitaxial growth [95, 9]. Commercially available substrates with small areas ($5\times5$ mm$^2$) were chemically and thermally treated to ensure an atomically flat surface.
STO cubic perovskite (a= 3.905 Å) is comprised of alternating $TiO_2$ and SrO lay-

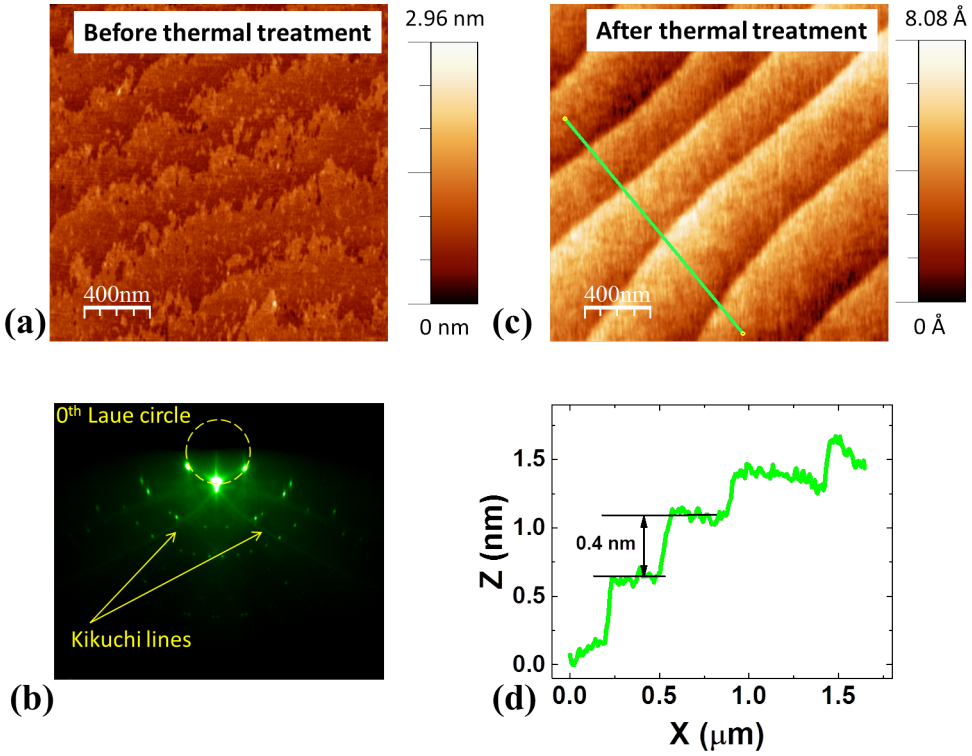


Figure 4.1: a) AFM image of STO surface after HF etching; b) RHEED diffraction pattern of (100) planes after annealing; c) STO surface after annealing process where the green line is the height profile represented in d).

ers. The single-crystal substrates were cut under a small angle with the (001) plane leading to the presence of step terraces with mixed layer termination. Immersing the substrates in water for 10 minutes weakens the bonds in the SrO layer and causes its removal when further immersed in hydrofluoric acid buffered solution ($H_2O$:$NH_4F$:HF= 100:3:1 volumic concentration) [96]. After surface reconstruction during annealing at 950°C for 2 hours, the terrace steps are $TiO_2$ terminated and become better defined with micrometre widths and heights of only one unit cell as seen in the atomic force microscope (AFM) topography (Figure 4.1 c and d) compared to the surface prior the thermal treatment (Figure 4.1 a). The smooth surface is also highlighted by the RHEED diffraction pattern (Figure 4.1 b) through the presence of intense diffraction spots and sharp Kikuchi lines. Slight elongations can be observed in some cases due to the terrace steps on the surface.

## 4.2 Growth and characterisation of (La,Sr)$MnO_3$ bottom electrode

### Growth and surface characterization of LSMO

The range of $La_{0.7}Sr_{0.3}MnO_3$ thickness can be limited in experimental devices due to the existence of the 'dead layer'. Despite the ferromagnetism and metallicity of the bulk, below a critical thickness thin films with this composition can become insulating, lose magnetic properties and have a reduced Curie temperature [97]. The value of the critical thickness was attributed to technical aspects such as variations of growth mode, oxidation level and nature of the substrates and was improved in time by increasing quality of films and interfaces. Due to the importance of interfaces in spintronic devices, the influence of the 'dead layer' has to be avoided. Therefore the LSMO thickness was chosen in order to be ferromagnetic and metallic at room temperature, well above the critical thickness (8 u.c. for metallicity and 3 u.c. for ferromagnetism) and thick enough so the nonmetallic nonmagnetic layer which can form at the interface with the substrate became insignificant [97].
The LSMO bottom electrode was deposited from a polycrystalline target using a multi-target RHEED-assisted PLD system with a 248 nm wavelength KrF excimer laser. Prior to every deposition, target polishing and pre-ablation were performed to avoid significant variations between samples. All LSMO growths took place at a substrate temperature of 600°C in oxygen pressure of 0.15 mbar, with 0.88 J/$cm^2$ laser fluence and 2 Hz repetition rate.
A RHEED phosphorus screen and a CCD camera were used to detect the diffraction pattern from the sample surface in real time. The electron beam was aligned with the (100) or (010) planes under a grazing angle with the substrate surface corresponding to the (001) plane. kSA 400 acquisition software was used to monitor the specular spot intensity. The presence of oscillations (Figure 4.2 a) indicates LSMO grows layer-by-layer on STO with a rate of ∼15 pulses/unit cell (∼39 pulses/nm). The laser ablation was stopped at the maximum intensity indicating the completion of 60 unit cells (u.c.). Further increasing intensity indicates surface smoothing through adatom migration on the sample surface. The intense diffraction spots on the $0^{th}$ order Laue circle in the RHEED pattern for the (001) plane imply a smooth surface with no significant changes of the in-plane lattice parameters compared to STO (insert in figure 4.2 a). In order to obtain high quality tunnelling devices, the barriers are further grown *in situ* on top of the LSMO electrode after selecting the new target and setting up the corresponding parameters. Characterisation of the films is performed *ex situ*, usually after the fabrication process is completed or on

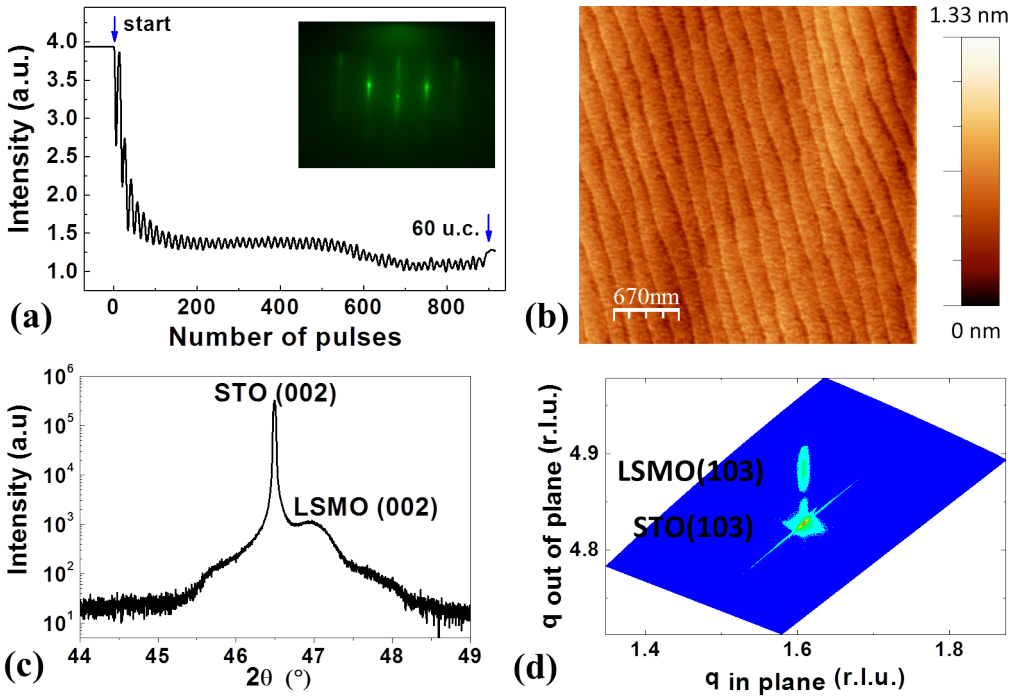


Figure 4.2: a) RHEED oscillations of the specular spot intensity showing the number of LSMO layers deposited; insert: RHEED diffraction pattern after LSMO deposition; b) AFM image of the surface; c) (002) plane diffractogram of STO and LSMO and d) RMS around the (103) plane of STO.

representative samples resulting from intermediate stages. Topography of a sample after depositing 60 u.c. LSMO on STO shows a flat surface which preserves the substrate steps (Figure 4.2 b). This indicates the termination of LSMO is $MnO_2$ as dictated by the $TiO_2$ termination of the substrate [98].

### Structural Analysis

During the growth the rhombohedral (pseodocubic) bulk unit cell turns into a out-of-plane oriented tetragonal unit cell [53]. XRD analysis shows the LSMO film grows epitaxially with the same orientation (001) as the STO substrate, as indexed in the $\omega - 2\theta$ scan (Figure 4.2 c). Asymmetric reciprocal space maps (RSM) around the (103) STO peak (Figure 4.2 d) show that the in-plane parameter extends to the substrate lattice value under tensile strain, causing the out-of-plane parameter to shorten. The value $c = 3.86$ Å was determined from the $2\theta - \omega$ scans around the (002) diffraction peaks (Figure 4.2 c) and the in-plane parameter $a = 3.90$ Å from the reciprocal space map around (103) peak, using the known position of STO

peaks for calibration. At the chosen thickness, LSMO grows fully strained on STO and would start to relax to its bulk values at a much higher critical thickness of ∼100 nm [99, 100]. Therefore the diffuseness of the LSMO (103) peak is attributed not to the lattice parameter variation, but to existence of artefact streaks specific to RSM scans.

TEM analysis was performed on the sample to study the LSMO structure locally. A cross-section of one of the final tunnel junction devices cut on the (110) plane direction is shown in figure 4.3 a. The LSMO film grows epitaxially in continuous layers on STO and no significant defects are visible at nanoscale. In the annular dark field image in figure 4.3 b) the high intensity of La and Sr atom columns is caused by more electron scattering than from Mn and O atoms which are less visible. The sharp interfaces are evident due to difference in Z number of the A-site atoms which causes the contrast. The intensity profile of the atom columns indicates the exact number of layers obtained from RHEED analysis and well delimited interfaces with both the substrate and layers grown subsequently. The values of the lattice parameters determined locally from atomic resolution TEM images ($a = 3.88$ Å and $c = 3.87$ Å) agree with the XRD values within the experimental errors which can be caused by the drift of the TEM specimen during imaging, resolution of the image and error of the sinusoidal function used for fitting the atom columns intensity profile.

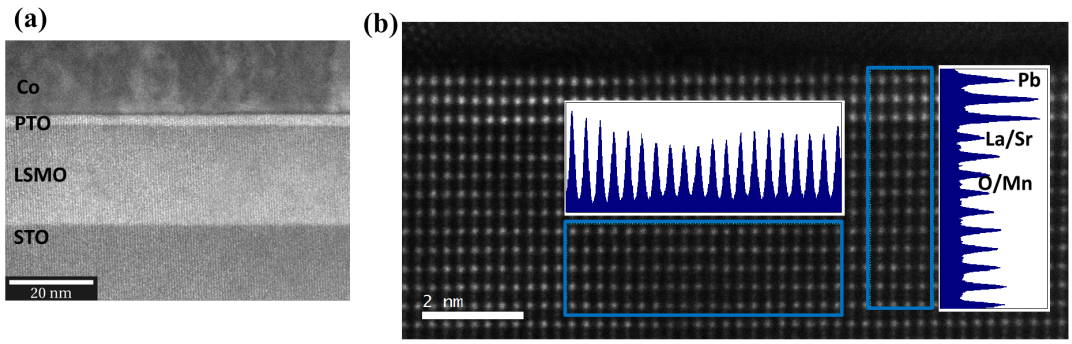


Figure 4.3: a) TEM image of final LSMO(60 u.c.)/PTO(6 u.c.)/Co tunnel junction illustrating the quality of LSMO film in report with the STO substrate and the PTO film; b) high resolution scanning TEM image showing the in-plane and out-of-plane intensity profile in LSMO: the highest peaks correspond to La/Sr atom columns, the less visible ones out-of-plane correspond to the O/Mn columns.

### Magnetic and electric properties

The applicability of the final junctions in practical devices is decided starting with the temperature working range, coercive fields and resistance of the component

films. The magnetic properties of LSMO grown on the STO substrate is given by its lattice deformation. Stress-induced anisotropy is expected; due to the expansion of the $a$ parameter, the direction of the easy magnetisation is oriented in the plane of the film [48, 100, 101]. It has been shown that step-induced magnetic anisotropy can be induced by breaking the rotational symmetry with regular surface atomic steps even in the case of low vicinal angles [102]. Magnetic properties are drastically influenced by the film thickness. 60 u.c. thick LSMO films were used in order to obtain metallic ferromagnetic films up to room temperature with low coercive fields [97].

The magnetic properties of deposited LSMO film were investigated to determine the Curie temperature ($T_C$) and coercive fields. Hysteresis loops acquired with SQUID magnetometer evidence the LSMO is ferromagnetic at $T$= 10 K and remains ferromagnetic at $T$= 300 K, showing a decrease in the coercive field from ∼24 Oe to ∼1.5 Oe as seen in figures 4.4 a and d. Normalised saturation magnetic moment ($m(T)/m(10\text{ K})$) was measured with temperature and illustrates how at $T_C$ the ferromagnetic order is lost due to the randomizing effect of the increasing temperature at $T_C$ = 336 K (Figure 4.4 b). The value was determined from its first order derivative which indicates the abrupt drop of magnetisation. The value is lower than in bulk (369 K [103]) and is similar to literature results obtained for the same composition, substrate and similar thickness values [97]. The distinct behaviour observed at low temperatures is attributed to the STO structural transition. At ∼ 103 K STO goes through a phase transition from tetragonal to cubic phase and LSMO adapts to the in-plane substrate changes which might cause the magnetisation easy axis to rotate slightly out of the film plane. The value of the magnetisation at 10 K is 457 emu/cm$^3$ and is comparable with that obtained for similar films in references [97] and [100]. The small atomic magnetic moment calculated for Mn is 2.85 $\mu_B$ and is lower compared to the bulk (3.5 $\mu_B$) and reference [100].

Transport properties of the LSMO film are affected by the magnetic behaviour of the film. Temperature-dependent resistivity of the LSMO sheet was measured using a Quantum Design physical property measurement system (PPMS). The $R(T)$ measurement was performed in 4 contact configuration during heating with 2 K/min rate under a saturation magnetic field (-10 kOe). An insulator-metal transition can be seen in the low temperatures graph insert (Figure 4.4 c) at $T$ ∼10 K. The ferromagnetic-paramagnetic transition can be correlated to a step-like feature in the sheet resistivity at $T_C$=360 K, slightly higher than the experimental value obtained from $m(T)$ and closer to the bulk $T_C$. The rise in the resistivity when approaching $T_C$ is attributed to decreasing carrier mobility due to scattering by increasing ther-

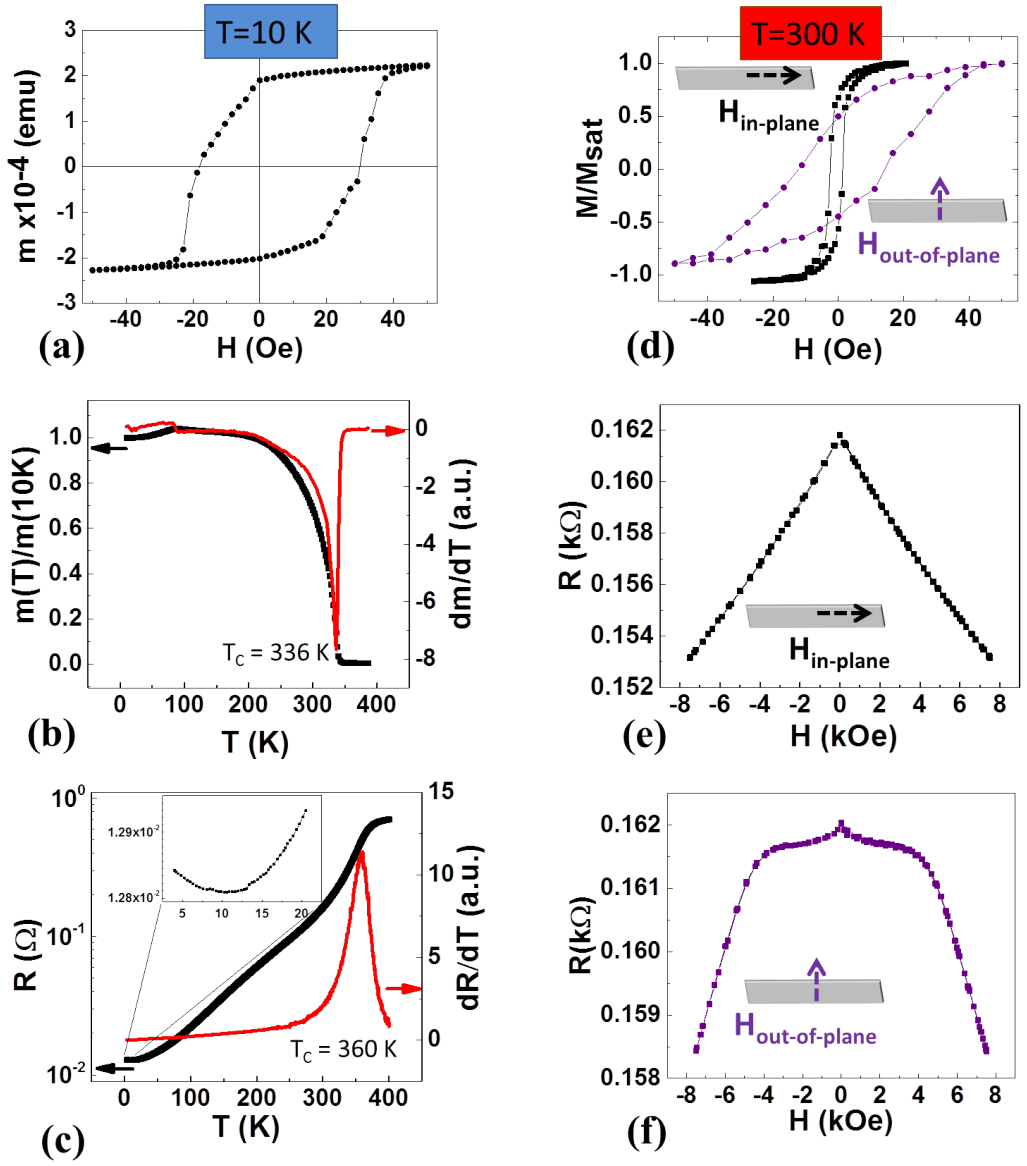


Figure 4.4: a) Hysteresis loop of LSMO magnetic moment measured at 10 K; b) magnetic moment vs. temperature and its derivative indicating the Curie temperature $T_C$; c) LSMO resistivity variation on temperature and its derivative showing $T_C$ = 360 K; d) hysteresis loops measured in-plane (easy axis) and out-of-plane at 300 K; LSMO resistance measured e) in-plane and f) out-of-plane at 300 K.

mal spin fluctuations [104]. TMR effect is correlated with the relative magnetisation orientation of the electrodes, therefore, the easy axis orientation decides the orientation of the applied magnetic field during magnetic measurements. In the case of LSMO grown on STO the easy axis is oriented in the film plane (Figure 4.4 d). The main anisotropy measurements of the magnetoresistance at room temperature are shown in figure 4.4 e and f. The in-plane and out-of-plane orientations of the magnetic field tend to align the local spins at different values reducing spin scattering of the conducting electrons.

## 4.3 Growth and characterisation of $PbTiO_3$ barrier

The functionality given by the two resistive states characteristic of FTJ is determined by the ferroelectric properties of the barrier and sharp interfaces with the electrodes. PTO films with thicknesses down to 3 u.c. were grown with the aim of investigating the critical thickness where ferroelectricity would vanish in this system. $PbTiO_3$ (PTO) ferroelectric barriers were deposited *in situ* on top of LSMO at 600°C, 0.2 mbar $O_2$ pressure, 0.45 mJ/cm$^2$ laser fluence and 4 Hz repetition rate. A $Pb_{1.1}TiO_3$ polycrystalline target was used to compensate for the volatility of lead. The RHEED diffraction pattern monitored by RHEED during the deposition; the specular spot intensity oscillations indicate a layer-by-layer growth (Figure 4.5 a). The resulting RHEED diffraction pattern in the inset indicates no significant change from the STO and LSMO in-plane parameters, while the elongations of the spots indicate the presence of the terrace steps on the surface. It was observed that even when using the same deposition parameters the deposition rate can vary slightly between samples (Figure 4.5 b), therefore the real time RHEED monitoring is necessary to obtain the desired thickness and low roughness of the films. A growing rate of ∼41 pulses/u.c. (∼102 pulses/nm) was determined from the 12 u.c. sample growth.

The deposition of 3, 6, 9 and 12 u.c. of PTO was achieved by stopping the target ablation at the maximum intensity of the specular spot indicating the completion of the topmost layer. Further increasing intensity implies increasing smoothness of the surface (Figure 4.5 a). The AFM topography of the PTO surfaces (Figure 4.5 c) show almost complete formation of the last layers where the height difference is just one unit cell, suggesting PTO is also $TiO_2$ terminated.

Macroscopic and local investigations of the films by XRD and TEM analysis were performed in order to explore the structure of the films and their relation to the substrate and LSMO film. $2\theta - \omega$ and RSM measurements performed on samples

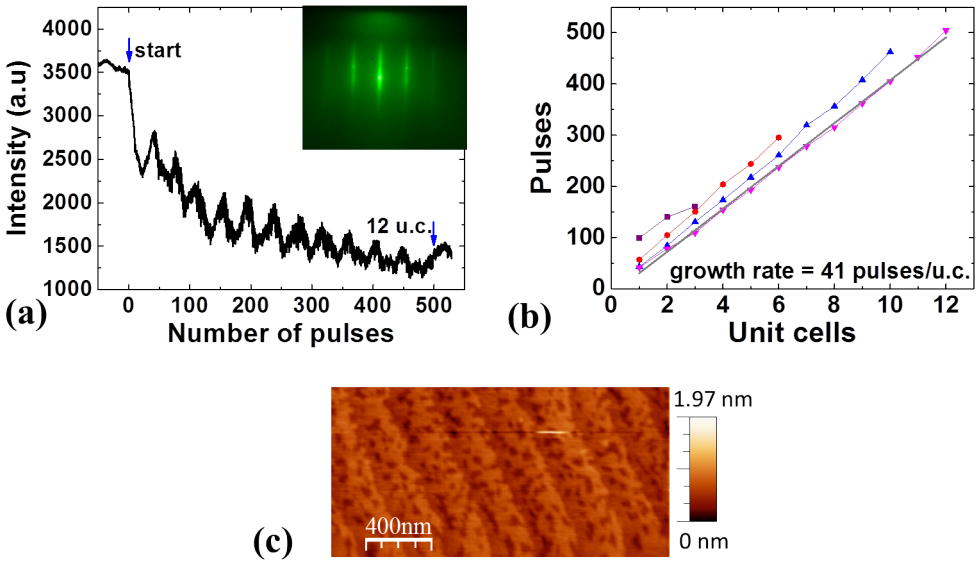


Figure 4.5: a) RHEED oscillations showing layer-by-layer PTO growth; insert: diffraction pattern after the deposition; b) deposition rate determined from RHEED for 12 u.c. PTO film; c) AFM image of the PTO surface.

with reduced thickness exhibit broad low intensity peaks. XRD scans performed on the sample with the thickest barrier, 12 u.c. are shown in figure 4.6. The RSM shows a weak streak corresponding to the value of the in-plane lattice parameter of (103) STO and LSMO peaks. This feature corresponds to the out-of-plane value ∼4.08 Å and can be observed only in the scans of samples containing PTO. The same value is determined from the $2\theta - \omega$ scan after using the STO (002) plane for reference and fitting the intensity with a peak function. The XRD peaks indexing indicates that PTO grows completely strained on STO/LSMO, adapting to the STO in-plane parameter.

High resolution scanning TEM confirms the number of layers and sharp interfaces determined by RHEED monitoring. Images of devices with 3 u.c. and 12 u.c. thick PTO barriers are shown in figure 4.6 c-f. Epitaxial growth of the PTO single crystalline films on LSMO can be observed for all samples, as well as sharp interfaces; no intermixing of A-site atoms at the interfaces or defects are visible. The in-plane parameter of PTO extends to adapt to the LSMO lattice and the out-of-plane parameter decreases reducing the tetragonality of the PTO film. The effects of thickness reduction on the macroscopic and local ferroelectricity and their effect on the tunnel junctions properties will be discussed in detail in the next chapter.

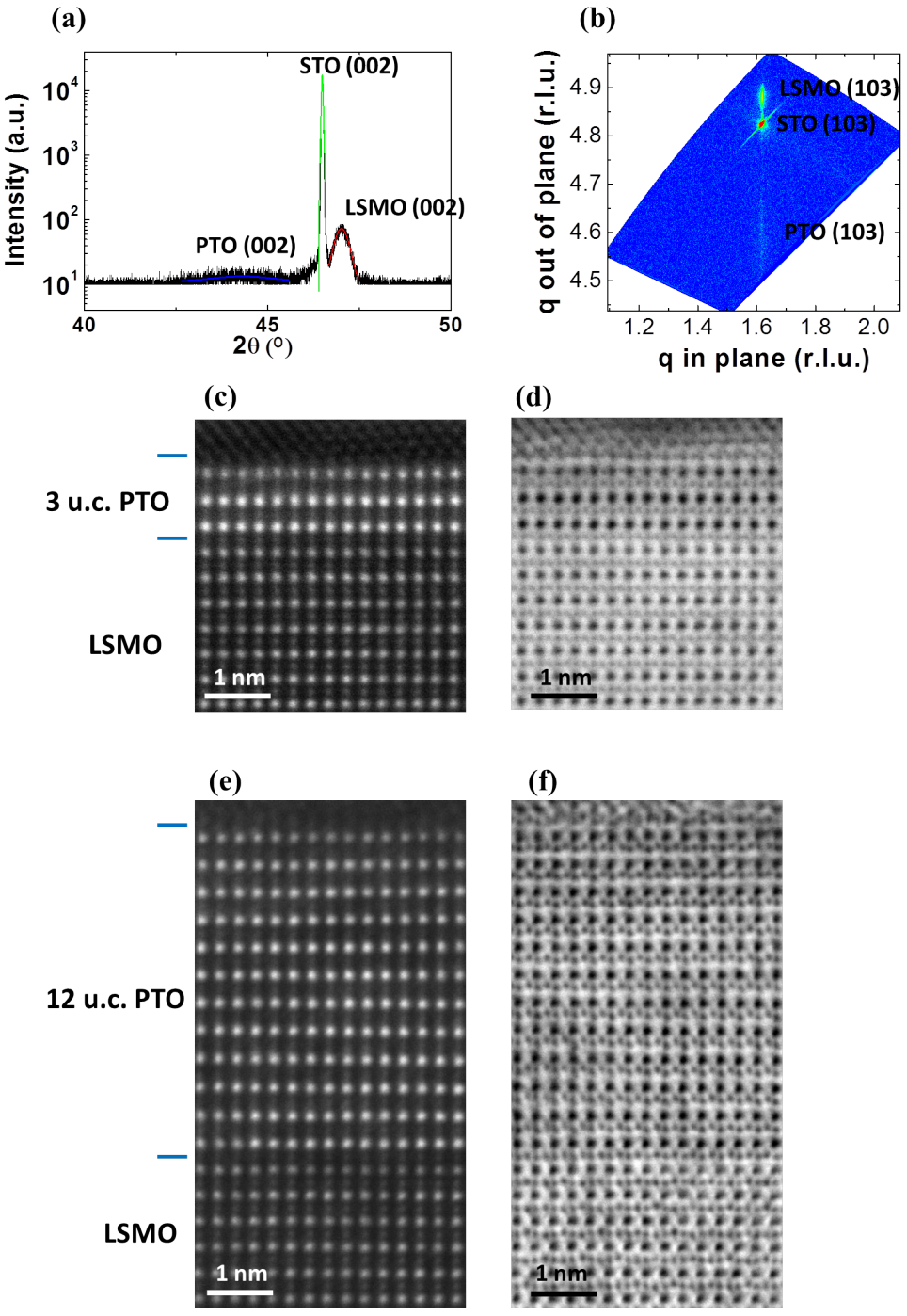


Figure 4.6: a) $2\theta - \omega$ scan of the (002) peaks of STO, LSMO and PTO; b) RSM around STO (103) peak; annular dark field, c) and e) and bright field TEM images, d) and f) of 3 u.c. (top) and 12 u.c. (bottom) PTO tunnel junctions.

## 4.4 Growth and characterisation of $PbZrO_3$ barrier

PZO is a typical antiferroelectric when in bulk form, while in thin films it has been shown to go through a thickness-driven antiferroelectric-ferroelectric transition. The critical thickness where this occurs depends on the system: 6.5 nm was predicted theoretically in a capacitor geometry [70], whilst ∼10 nm was obtained experimentally in PZT/PZO multilayers [68], and ∼22 nm was experimentally observed in LSMO/SRO/PZO/SRO heterostructures [69]. PZO films in a similar thickness range were grown to obtain tunnel junctions with ferroelectric and antiferroelectric barriers.

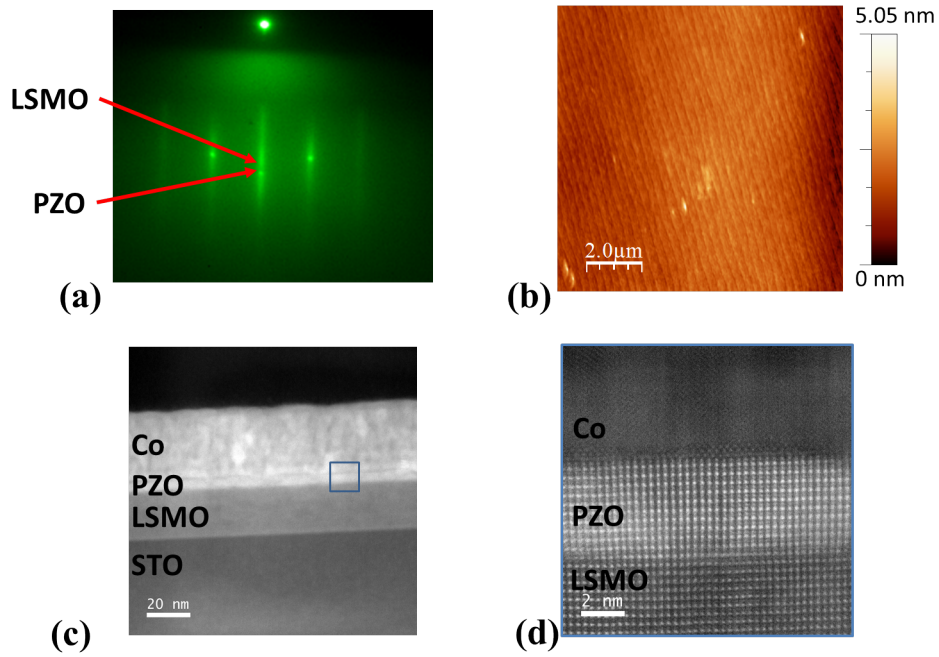


Figure 4.7: a) RHEED diffraction pattern showing the additional spot caused by the PZO film growth; b) AFM image of the PZO surface; c) TEM dark field image of the local structure and d) increased magnification of the area marked in c).

PZO barriers with thicknesses of 11 (∼4.5 nm), 16 (∼6.5 nm), 22 (∼9 nm) and 27 (∼11 nm) u.c. were deposited with 1 J/cm$^2$ energy, 10 Hz repetition rate of the laser, at 600$^o$C substrate temperature, in 0.24 mbar $O_2$ pressure. It is difficult to track changes in the intensity of the specular spot corresponding to the STO substrate and previously grown LSMO film due to the appearance of an extra spot which can indicate different in-plane lattice parameters from STO/LSMO or 3-dimensional growth. Though the surface of the resultant film is smooth, as shown

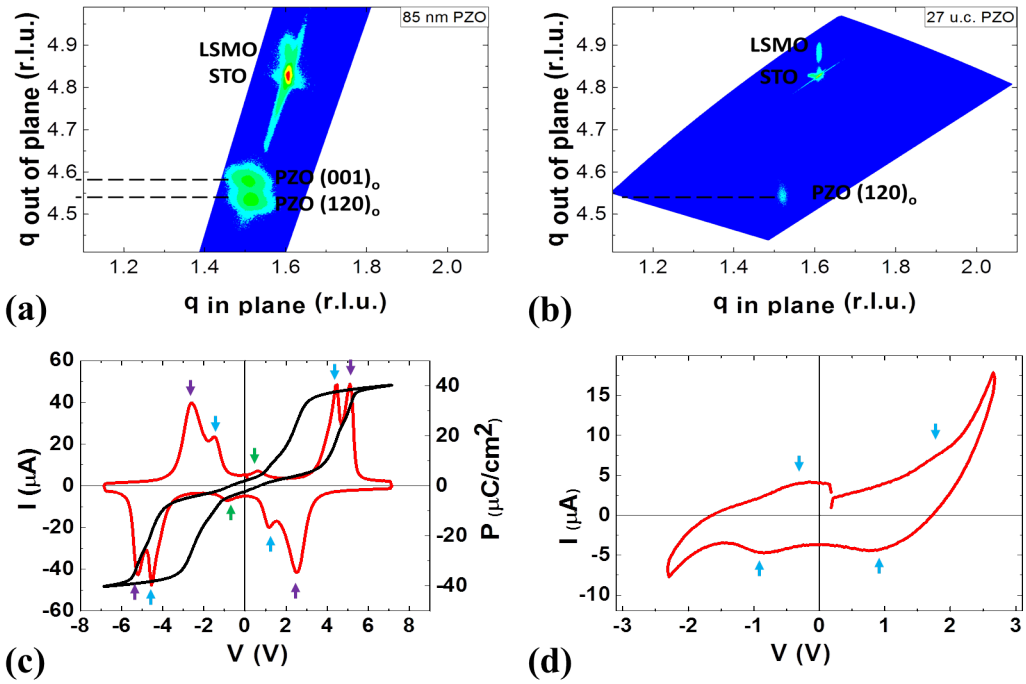


Figure 4.8: RSM of STO/LSMO/PZO for a) 85 nm and b) 12.5 nm thick PZO; c-d) P(V) hysteresis loops for the same thicknesses.

in figure 4.7 b, local analysis shows a few defects in the structure of the PZO film such as dislocations and variation of thickness on larger scales.

Reciprocal space maps (RSM) of samples containing 27 u.c. PZO and significantly thicker PZO (∼85 nm) were performed to evidence the dependence of structure with thickness variation. RSM was performed around the (103) plane of STO and it was observed that thick PZO film (85 nm) grows on LSMO along two orientations: orthogonal $(001)_o$ and $(120)_o$ planes (Figure 4.8 a). Polarisation-voltage hysteresis curves and switching current-voltage dependence were measured using an AixAcct 3000 thin film analyser. On both directions, PZO is antiferroelectric as shown by the two sets of four switching current peaks in the I(V) and P(V) hysteresis loops. At small fields a ferroelectric hysteresis curve is overlapping with the antiferroelectric double loop which implies a ferroelectric phase is present in reduced amounts, most probably rhombohedral PZO, not detected in the RMS. At 11 nm thickness, the dominant orientation is antiferroelectric $(120)_o$ which determines the four weak switching current peaks in figure 4.8 [105]. The nonzero values of the current at zero bias could be caused by the presence of ferroelectric PZO, or due to current leakage through the film.

## 4.5 Co top electrode

A polycristalline Co top electrode was deposited *ex situ* by magnetron sputtering at $2.5\times10^{-3}$ mbar Ar pressure and 20 W applied power. $40\times40$ $\mu m^2$ top electrode patches were obtained by patterning the Co film by photolitography and wet etching: AR-P 3510 (from Allresist) positive photoresist was spin coated on the samples, baked at $100^oC$ for one minute and then exposed to UV light through a mask. The exposed photoresist was then developed and Co was etched in the unprotected areas using commercially available 65% $HNO_3$ solution further diluted in water (1:50). The advantages of using the $40\times40$ $\mu m^2$ squares with 10 $\mu m$ spacing is in obtaining a large number of devices in a $5\times5$ $mm^2$ sample while having suitable dimensions for electric contacts in the TTP4 probing station and PPMS.

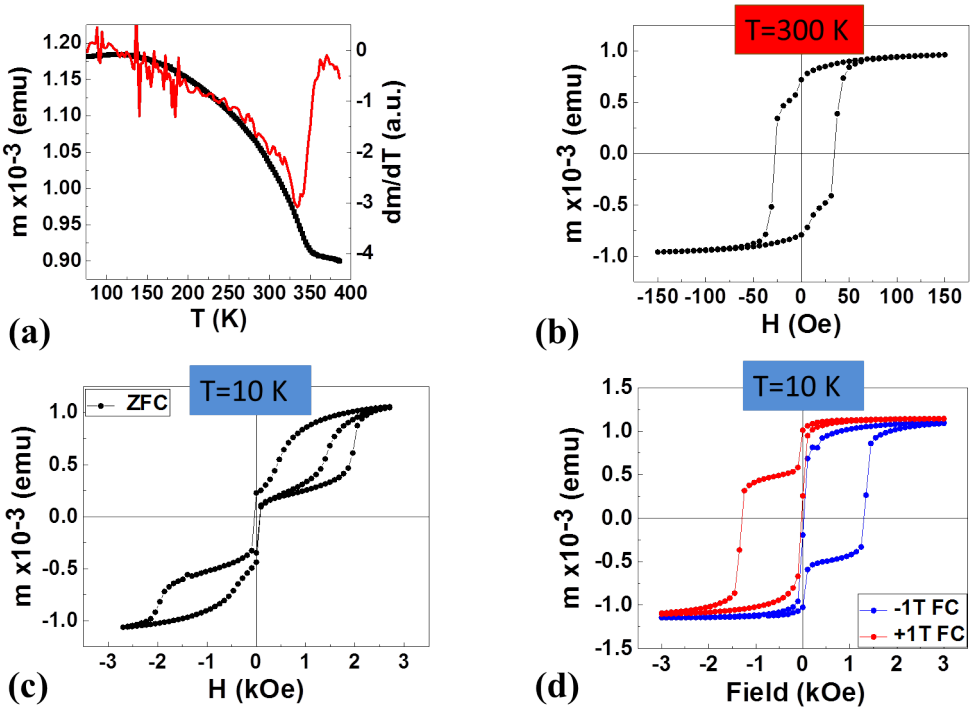


Figure 4.9: a) Magnetic moment variation with temperature and its first derivative for a STO/LSMO/PTO/Co sample; hysteresis curves at b) 300 K and c) 10 K after zero field cooling; d) hysteresis curves at 10 K after cooling the sample in -10 kOe (blue) and +10 kOe (red).

The magnetic measurements of a STO/LSMO/PTO/Co structure are summarised in figure 4.9. Temperature dependence of the total magnetic field shows clearly the ferromagnetic order partially disappears at ∼350 K corresponding to the $T_C$ determined for LSMO. The magnetic hysteresis highlights the existence of two hys-

teresis loops as expected, one with lower coercive fields corresponding to the values previously observed for LSMO and the higher coercive field values to Co. When cooled with an applied magnetic field, the samples exhibit exchange bias: the hard ferromagnetic hysteresis loop is shifted in the opposite direction of the field. The behaviour is characteristic of Co/CoO interaction and is attributed to the oxidation of Co at the surface or interface with the barrier [106, 107]. Pinning the Co layer helps in obtaining stable magnetisation switching, ensuring completely parallel alignment occurs, especially when the coercive fields of the two layers would have close values [33].

## 4.6 Summary

This chapter illustrates how the samples studied in the following part were obtained, to help in interpretation of experimental results and understand how properties of the component films contribute to the observed effects in the whole device. The films are analysed after every major step of the fabrication process to ensure functional devices are obtained. Stoichiometric epitaxial growth of high quality films using PLD can be obtained with optimal parameters. The RHEED *in situ* monitoring of the growth enables sharp interfaces and is a reliable method for real time thickness determination, as confirmed by TEM analysis. The macroscopic transport and magnetic properties of the electrodes were studied in this chapter due to their importance to obtaining the TMR effect in the resultant tunnel junction devices and understanding its origin. The selection, characterisation and optimisation process of the component properties leads to devices which are functional up to room temperature and use low fields for writing information.

# Chapter 5

# Size effect in LSMO/PTO/Co ferroelectric tunnel junctions

The tetragonal ferroelectric $PbTiO_3$ has shown promising results when used in tunnel junctions; it exhibits giant TER effect up to $10^3$-$10^4$% when grown on STO/SRO and TMR at room temperature [9]. Even more interesting, lead titanate is one of the components of the PZT solid solution which presents spin transfer control by polarisation reversal in LSMO/PZT/Co tunnel junctions [7] which were attributed so far to the Ti and Co interaction at the ferroelectric/ferromagnetic interface. The LSMO/PTO/Co junctions can thus offer insights into the effect of the Ti-Co ions hybridisation and help in understanding the effects observed in PZT.
This chapter presents the investigation of the fabricated LSMO/PTO/Co devices and a view on their multiferroic tunnel junction performances. TMR and TER which strongly depend on processes occurring at the ferroelectric/ferromagnet interface are studied with reducing ferroelectric barrier thickness. Generally, due to the increased depolarisation field, the ferroelectricity disappears at a critical thickness which would render ferroelectric tunnel junctions non-functional. This chapter studies the size effect on ferroelectric properties and domain configuration of the films in devices containing lead titanate barriers having 3 u.c., 6 u.c., 9 u.c. and 12 u.c. thickness. The critical thickness is found for the LSMO/PTO/Co system and the tunnelling properties are investigated by varying the contribution of the interfaces compared to the barrier bulk effects. First, the direct tunnelling regime used for defining most of the performance parameters is identified for the investigated thicknesses and temperatures. In this regime, the two non-volatile resistive states characteristic to FTJ which result from polarisation switching in PTO can be read nondestructively, without affecting the polarisation orientation. Two addi-

tional non-volatile magnetic states determined by the magnetisation alignment are highlighted by resistance measurements during magnetic field sweeps. Moreover, a magnetoelectric coupling characteristic to multiferroic materials and interfaces is detected in LSMO/PTO/Co devices.

## 5.1 Size effect on polarisation domain structure in PTO ultra-thin films

### 5.1.1 Formation of local polarisation vortices in LSMO/PTO/Co tunnel junctions

Ferroelectric polarisation at all scales can form complex structures, different from the simple Kittel-like domain structures as shown by recent studies [108, 109, 110, 111]. At ferroelectric-ferroelastic domain walls the flexoelectric response to strain gradients enhances the polarisation curling while at non-ferroelastic walls continuous polarisation rotations have rarely been observed [112, 2]. So far, studies of atomic scale curling of polarisation and vortex formation were made on systems without electrodes, by enhancing the depolarisation field. Vortices could, however, be more easily investigated and manipulated by using electric field applied by electrodes in a capacitor geometry. In this case, the screening effect of the metal's free carriers changes the constraints of the films from previous experiments and raises the question of the stability of vortices. This question can be addressed by studying capacitor devices containing a few unit cell thick ferroelectric films. The practical applications of this kind of devices are FTJ that allow electrons to tunnel between the two electrodes, similar to the better known MTJ [113]. Moreover, the value of the tunnelling current encloses information about the polarisation state which can be read nondestructively: by switching the ferroelectric polarisation orientation, a modulation of more than five orders of magnitude can be obtained [114, 61, 115]. When the ferroelectric barrier characteristic to FTJ is combined with ferromagnetic electrodes in MTJ, four-state multiferroic tunnel junctions are obtained which can be controlled by both electric and magnetic field [116, 117, 8]. Depending on ion interactions at the barrier/electrode interfaces, even polarisation-controlled spin filtering could be observed [7].

When it comes to studying ferroelectrics in capacitor geometries, especially in the case of thin films, it is expected that both the electrodes and their interfaces have an important influence on the domain structure. An important characteristic of the electrode is the free carrier concentration, since they are responsible for screen-

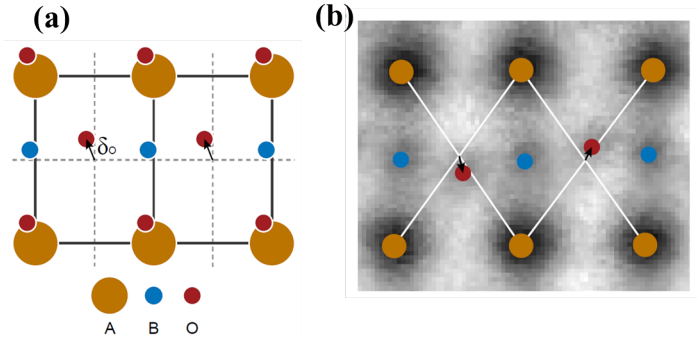


Figure 5.1: a) Schematic oxygen displacement in the projection of the (110) plane of a perovskite; b) oxygen displacement measured from an experimental image of LSMO; reproduced from [3].

ing the depolarisation field produced by bound charges at the ferroelectric surface. An asymmetry of the electrodes can therefore determine a complex domain pattern [118].

In this section aberration-corrected scanning transmission electron microscopy was used to study ferroelectric domains and domain walls in tunnelling devices having PTO films with thicknesses of 3, 6 and 9 u.c. and LSMO and Co electrodes. Experimental details on the preparation, imaging, calculations and analysis can be found in [88]. For this study TEM samples were obtained by a FIB standard lift-out procedure followed by warming to 50$^o$C for $\sim$10 h prior to being inserted into the TEM. In order to obtain the dipole distribution, lamellas with PTO in the 'as grown' polarisation state were imaged along the [110] axis simultaneously in annular dark field (ADF) and annular bright field (ABF) modes, so both heavy and light elements were visible with atomic resolution. After processes involving filtering and Gaussian convolution of the image using an in-house program, the oxygen displacement was determined relative to the A-site atoms as can be seen in the schematic and experimental representations in figure 5.1. The B-site displacements ($\Delta_B$) were obtained relative to the centre of the $O^{2-}$ octahedra from ABF images and were used to determine the local dipoles. The displacement is proportional to the polarisation with a constant $\kappa$ which can be deduced from bulk measurements:

$$P_S = \kappa \Delta_B \tag{5.1}$$

The centre of the oxygen octahedra was determined as the centre of mass of the two nearest oxygen atom columns. Quantitatively, the polarisation was calculated using the volume of the unit cell $v$, the displacements of the O and B-site atoms from the

positions of centrosymmetry (taken as the centre of the nearest A-site positions) $\delta_{O,B}$ and the effective charges of the O and B atoms $Z_{O,B}$:

$$P_S = \frac{1}{v}(3\delta_O Z_O - \delta_B Z_B) \tag{5.2}$$

With decreasing thickness of the film, a transition of the domain structure occurs from Kittel-like domains [119], as observed in thick films, through complex curling to monodomain in the thinnest film. Unlike in thick films where domain walls are thin and smooth [120], it is observed that in ultrathin ferroelectric films the complex domain structure consists of polarisation curling, spanning from Bloch (Néel)-Ising structures to flux closure and vortices.

**Domain structure in 9 u.c.-thick PTO barrier**

In figure 5.2 a can be seen the PTO film having 9 u.c. and interfaces with LSMO and Co electrodes. The $Z$ contrast makes the ADF image sensitive to chemical composition of the component films. The atom column intensity scales with the average atomic number $Z^{1.7}$, demonstrating the sharp LSMO/PTO interface in figure 5.2 b. The ABF image in figure 5.2 c shows the $O^{2-}$ columns and improved contrast and allows determination of the column positions with picometer precision [121, 122].
The ferroelectric state of the PTO film is proven by the 2-dimensional quiver plot in figure 5.2 e, where the polarisation points towards the top Co electrode in the center, while on the outermost regions of the image it points towards the bottom LSMO electrode. This is the illustration of a classic $180^o$ domain structure. For this thickness, the width of the Ising-type domain walls would be 2 u.c.. Instead, a wider wall with roughness of $\sim$ 4-5 u.c. is observed. Moreover, two vortices can be observed in the polarisation map: one at the PTO/Co interface and the other one close to the LSMO/PTO interface. Located at the domain walls, they form a more complex structure separating the two domains. Here the dipole direction changes continuously clockwise and anticlockwise, forming paired vortices opposing each other, similar to the ones recently reported in PTO/STO superlattices [2].
It is worth noting that an atom column containing varying displacements perpendicular to the electron beam would appear elongated, corresponding to the projection of mixed positions. The absence of this effect implies that dipoles are constant through the thickness of the specimen which would not happen in the case of Néel and Bloch walls which would extend within the TEM specimen thickness. The results presented in figure 5.2 imply that at this thickness, and also for thicker films as determined by ab initio calculations [123], the depolarisation field which is always

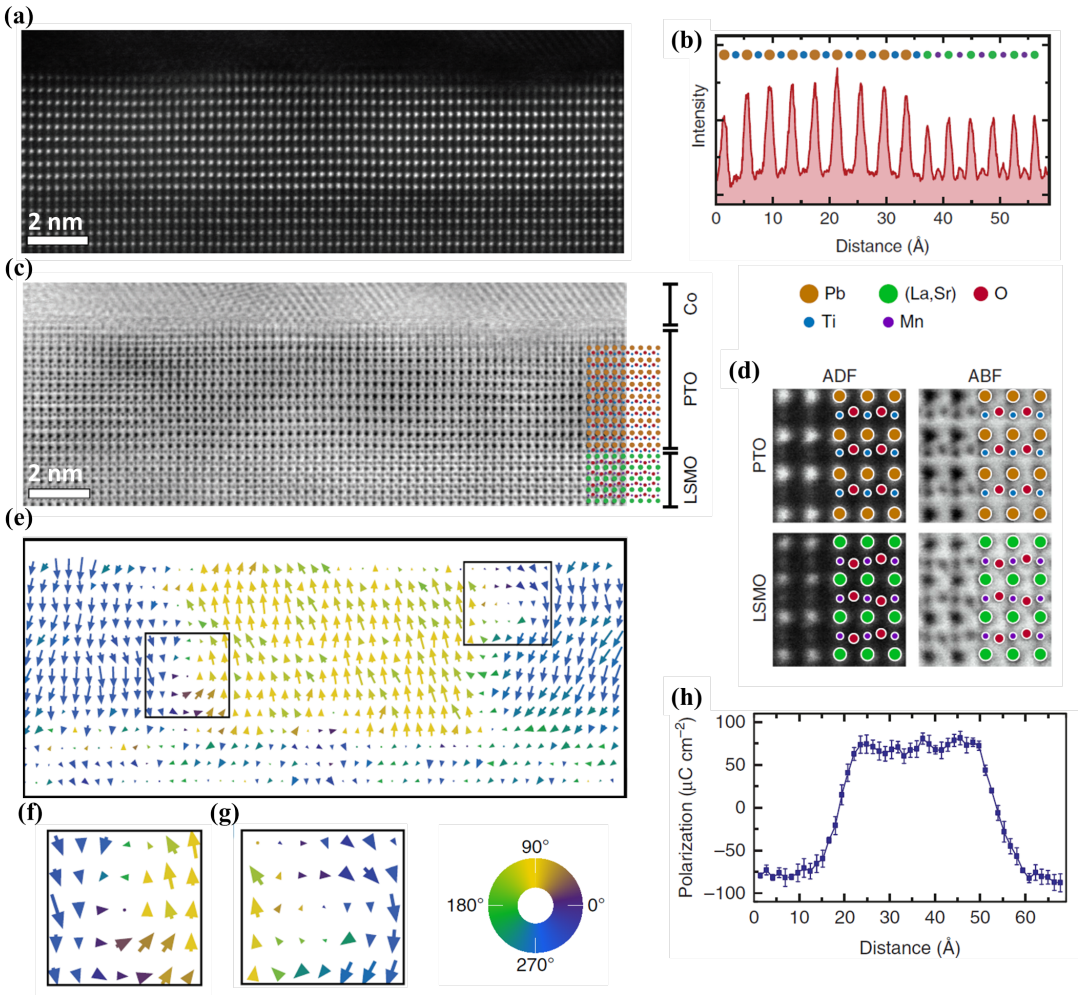


Figure 5.2: a) Atomic resolution ADF image; b) atom column intensity showing the different compositions of the films; c) ABF signal collected simultaneously with a); d) magnified regions to show the LSMO and PTO structure with different contrast; e) quiver plots showing dipoles measured from c); f-g) enlarged vortices from the regions marked in e); h) average out-of-plane polarisation across the domains; error bars are represented by standard error of the mean; reproduced from [3].

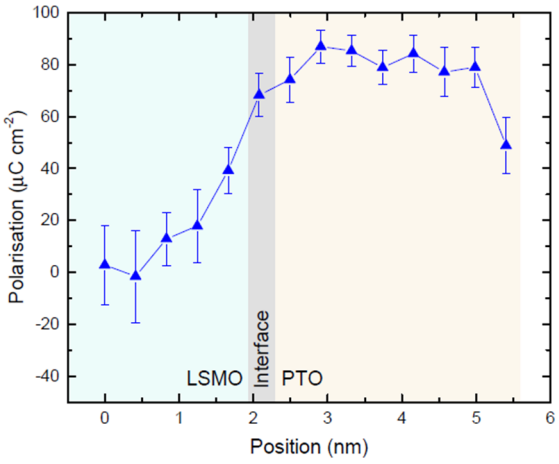


Figure 5.3: Average of polarisation across the thickness of a 9 u.c. PTO film with highlight on the LSMO/PTO interface: values are obtained from averaging rows of unit cells and the error bars are the corresponding standard errors of the means; reproduced from [3].

present in ferroelectrics influences the polarisation distribution. This effect depends on the electrode asymmetry. Figure 5.2 h shows the out-of-plane polarisation averaged through the film thickness, smoothly changing between positive and negative values at the 4-5 u.c. thick domain walls. When oriented toward the LSMO electrode, an average polarisation of 80±1 $\mu$C/cm$^2$ was determined, comparable to the bulk value of 84 $\mu$C/cm$^2$ obtained from the bulk ionic displacement [124]. The polarisation oriented towards the Co top electrode is reduced to 70±2 $\mu$C/cm$^2$. The polarisation is mostly constant across the PTO film and even extends into LSMO where displacements are detected in the first 2-3 u.c.(Figure 5.3). Compared to Co which is able to screen both positive and negative surface charges, LSMO is a half-metal having a lower carrier concentration and weaker screening abilities [54]. Generally, when there is not sufficient free charge for reducing the depolarisation field energy in ultrathin films, they still display ferroelectric properties by formation of 180$^o$ stripe domains as shown by diffraction experiments in STO/PTO (9 u.c.) structures [125]. In the 9 u.c. PTO film under investigation, the cross section suggests the same mechanism could be responsible for the observed polarisation orientations.

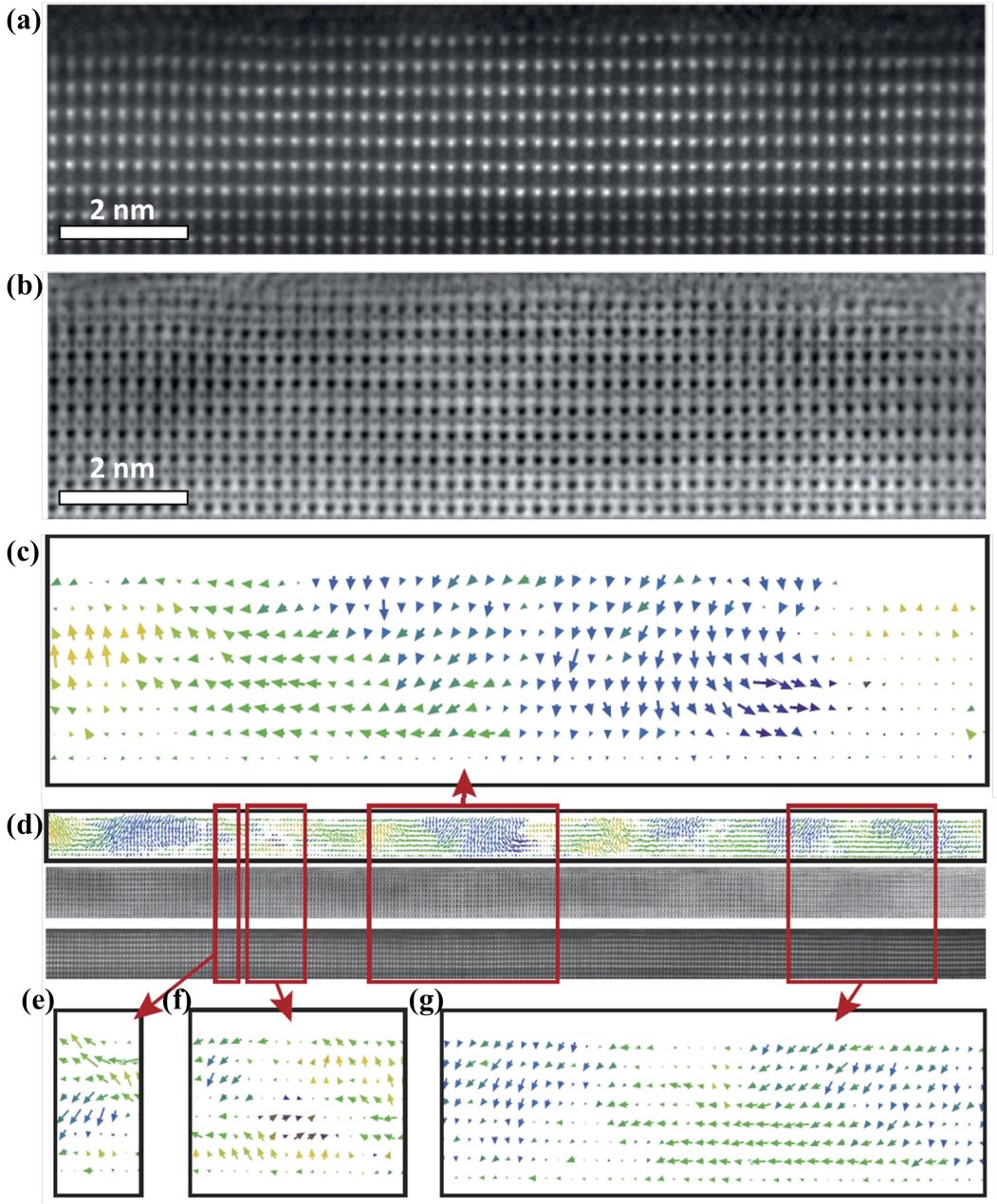


Figure 5.4: Atomic resolution images in: a) ADF and b) ABF modes of a 6 u.c. PTO film; c) corresponding plot quiver plot of the dipoles; d) large area analysis including a dipole map, ABF and ADF images with insets of the regions of interest in e-g); reproduced from [3].

### Domain structure in 6 u.c.-thick PTO barrier

Next, the domain structure in films thickness reduced to 6 u.c. with LSMO and Co electrodes is investigated. The high resolution ADF and ABF images highlight good crystal quality with defect free sharp interfaces (Figure 5.4). The quiver plot in figure 5.4 c shows the PTO film is still in a polarised state, but with significantly different domain pattern. Instead of the relatively well-defined domains with small vortices in 9 u.c. PTO, a combination of Landau-Lifshitz flux-closure domains and vortices is present. Large areas ($\sim$75 nm) reveal a high degree of disorder: areas where the polarisation switches throughout the thickness of the film (Figure 5.4 e), complex regions with curling (Figure 5.4 f) and (110) type domain walls forming $45^o$ with the interface (Figure 5.4 g), typical to thicker films. At the Co interface, the up to $\sim$8 nm domain width can be observed, larger than in 9 u.c. PTO ($\sim$6 nm) and it reduces to $\sim$4 nm at the LSMO interface. The domains with parallel walls forming $45^o$ with the interface have constant thickness throughout the film and can be as small as $\sim$3 nm. The average domain width is 5.3$\pm$0.7 nm, in agreement to the expected value of 5.2 nm obtained from the Kittel law for this thickness.
Some of the observed domain wall structures have been theoretically predicted for this thickness. Therefore closure at the LSMO interface could be caused by the electrode asymmetry [118]. Certainly the investigated PTO film is both ferroelectric and ferroelastic and for small thicknesses, additional parameters such as inhomogeneous electric fields might drive the system to a disordered phase described in literature as incommensurate, where ferroelastic systems no longer undergo a simple para-ferro phase transition [126]. Macroscopically, the effects of applying an external electric field is the appearance of the TER effect, as expected for proper ferroelectric films.

### Domain structure in 3 u.c.-thick PTO barrier

Decreasing the film thickness to 3 u.c. causes the domain structure to disappear (Figure 5.5). The polarisation shows a significant gradient through the film, pointing towards the LSMO bottom electrode with remanent curling. The polarisation value at the Co interface is 76$\pm$5 $\mu$C/cm$^2$, the same as its equivalent in 9 u.c. film and reduces to zero towards LSMO. This result suggests that 3 u.c. is the critical thickness for local ferroelectricity when grown under positive in-plane misfit strain. Measuring TMR effect in tunnel devices with 3 u.c. PTO barriers demonstrates that the film is functional. However the polarisation cannot be switched by means of PFM (absence of phase and amplitude contrast and of local hysteresis loop) and electrical measurements (absence of TER effect). This is most likely due to the

polarisation gradient associated to a gradient in electric field and therefore with free charges localised within the ferroelectric layer.
In this section it was shown how the domain structure varies with reducing the ferroelectric film thickness. At 9 u.c., PTO shows almost classic antiparallel domains with rougher walls that can exhibit paired opposing vortices. Reducing thickness to 6 layers of PTO, a disordered phase is observed with toroidal flux closure structures. By reducing the thickness to 3 u.c., polarisation oriented out of plane is observed. The results indicate the polarisation curling, the formation of vortex and flux-closure structures appear in ferroelectric ultrathin films despite the metallic electrodes. Moreover, they offer the possibility to control these structures using local electric field.

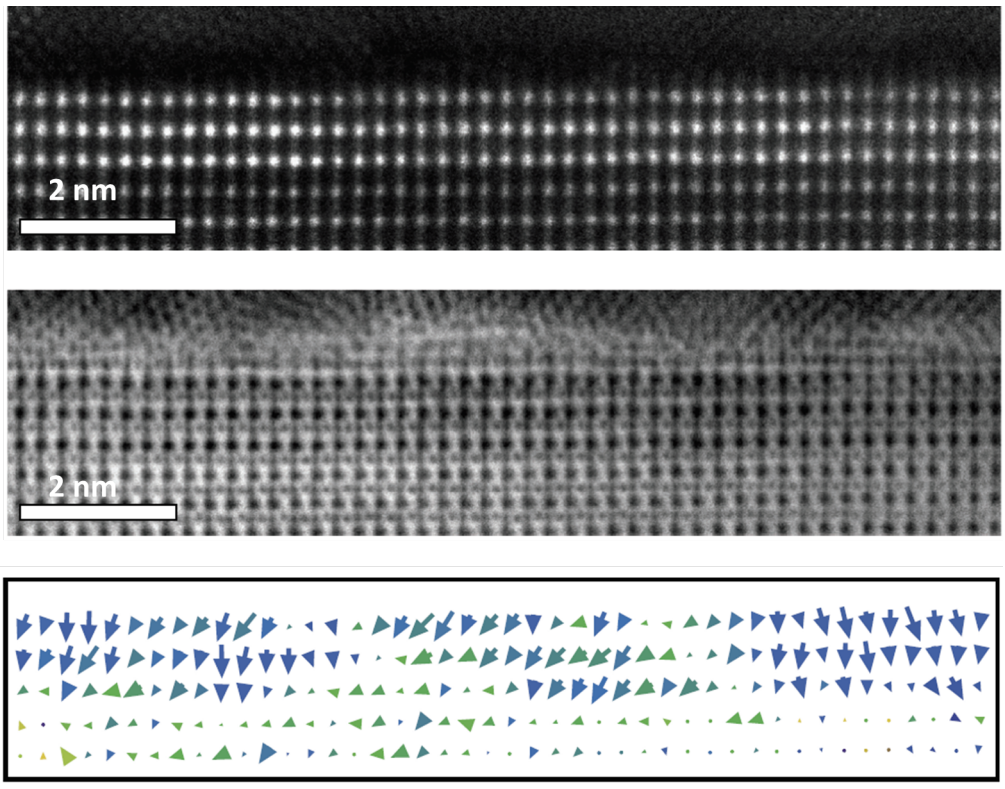


Figure 5.5: a) ADF and b) ABF atomic resolution images; c) corresponding quiver plot of the local dipoles in a 3 u.c. thick PTO film; reproduced from [3].

### 5.1.2 Critical thickness for ferroelectricity in STO/LSMO/PTO system

In real ferroelectric tunnel junction devices a switchable (yielding two resistive states) stable polarisation of the barrier is critical for their functionality. Because ferroelectricity is a collective phenomenon, in the case of thin films it is expected to be suppressed and even eliminated at a critical thickness which can depend on the nature and quality of the fabricated devices. The size effect on ferroelectricity of the lead titanate films is further investigated.

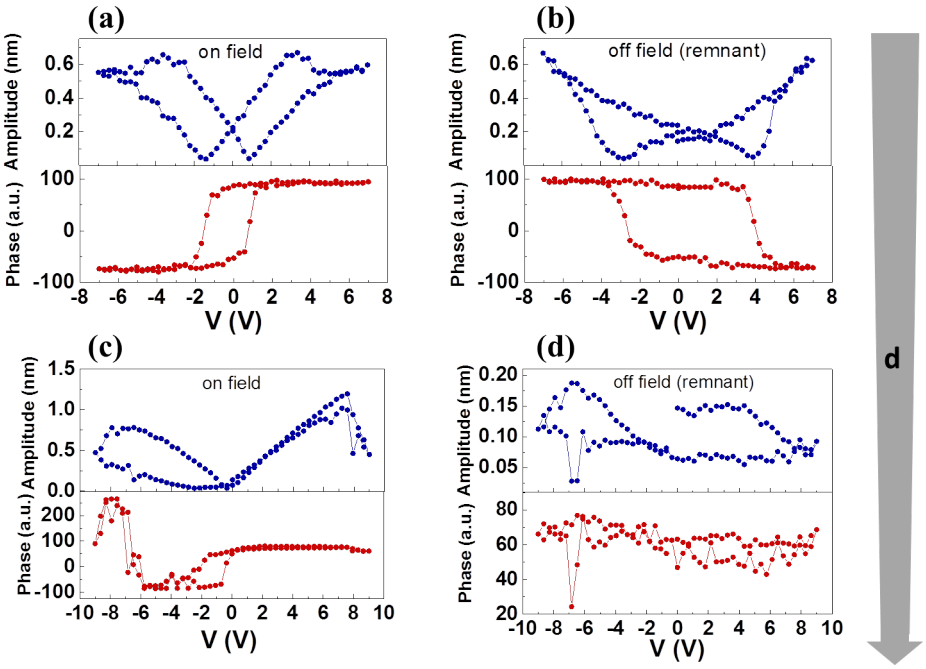


Figure 5.6: Local hysteresis loops for 6 u.c., a) and b) and 3 u.c., c) and d) PTO films; the amplitude and phase were measured by PFM with electric field applied on the conducting tip, a) and c) and in a remnant state after the field was removed, b) and d).

When investigating a device with a top electrode by PFM, generally the film piezoresponse decreases with the electrode thickness and at ∼35 nm Co, PTO domain features would not be clearly distinguished [127]. Therefore PFM analysis was performed on bare LSMO/PTO structures. The local amplitude and phase dependences on the applied voltage are shown in figure 5.6. It can be observed that ferroelectric properties degrade with reducing the PTO thickness from 6 u.c., where local hysteresis loops show polarization switching to 3 u.c., where switching cannot be detected. Figure 5.7 shows the amplitude and phase signals obtained for the 6 lay-

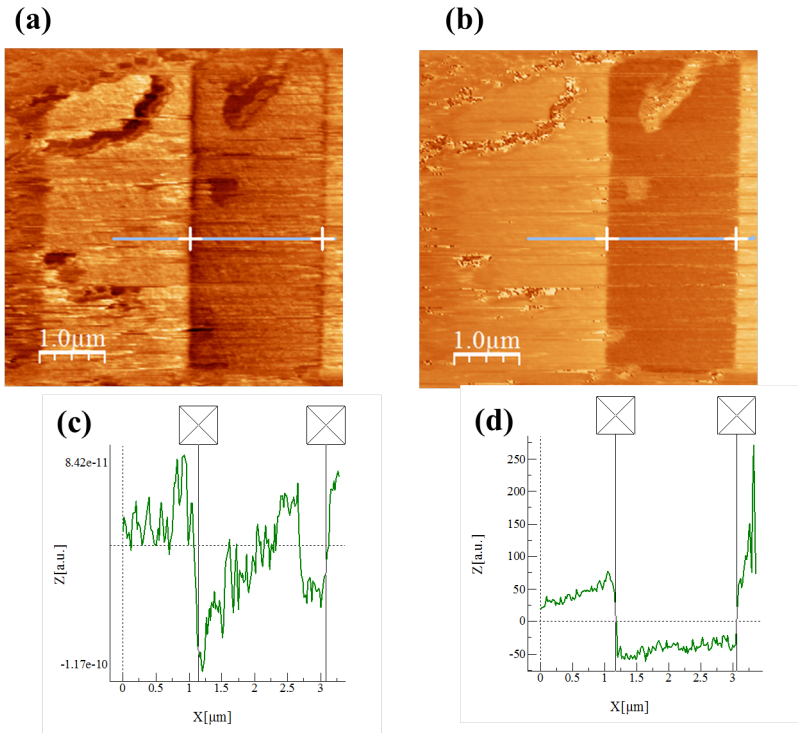


Figure 5.7: a) 5×5 $\mu$m$^2$ scan of 6 u.c. PTO film: a) PFM amplitude signal and b) PFM phase signal; c-d) line profile corresponding to the blue lines in the amplitude and phase scans.

ers PTO film. The polarisation was switched in the direction of the electric field by applying -6 V bias (P towards the film surface: P↑) through the tip and half way through the scanning it was changed to +6 V (P toward the LSMO interface: P↓). The 5×5 $\mu$m$^2$ scans in figures 5.7 a) and b) were read using 400 mV and exhibit both switched (2×4 $\mu$m$^2$ areas) and 'as grown' polarisation states. The separating domain walls are characterized by minimum values in the amplitude signal and zero values in the phase signal as seen in the line profile (Figures 5.7 c and d). It can be seen that the polarisation in the 'as grown' state of 6 u.c. PTO gives the same signal as the polarisation oriented towards LSMO.

In the case of stress-free (001) PTO films it was shown by first principle calculations that down to 3 u.c. thickness exhibit intrinsic perpendicular polarisation [128]. In 3 u.c. strained PTO in capacitor configuration, though shifts of the Ti and O ions relative to Pb were observed locally by TEM, the polarisation cannot be switched during PFM experiments. The different properties can be due to inefficient and inhomogeneous screening of the conductive tip in air which cannot reduce the depolarisation field in comparison with Co top electrode. The lack of ferroelectric

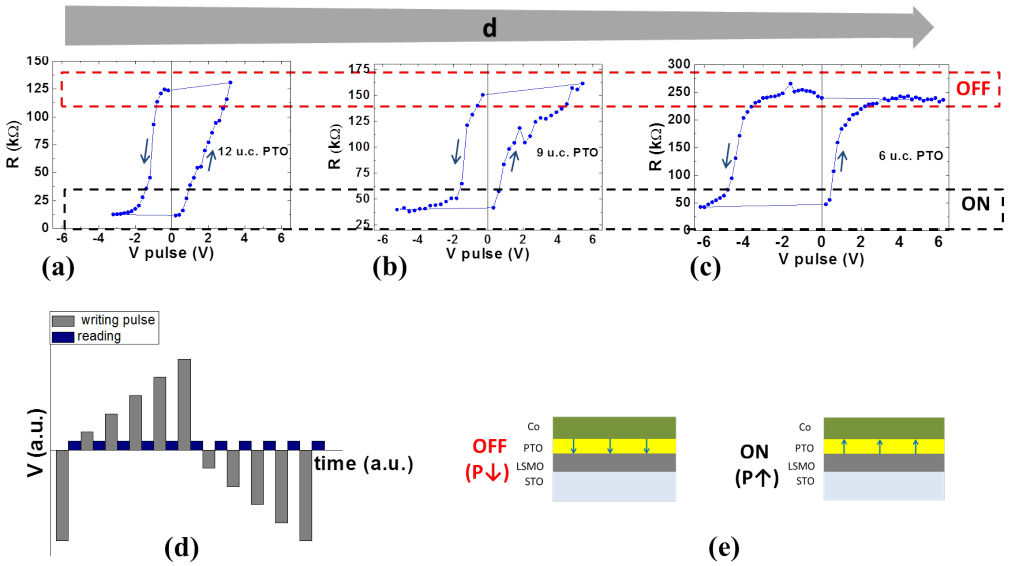


Figure 5.8: Hysteresis obtained by applying voltage pulses for LSMO/PTO/Co samples with a) 12 u.c.; b) 9 u.c. and c) 6 u.c. PTO barriers; d) sequence of writing and reading voltages; e) polarisation orientation in the ON and OFF states.

properties in the 3 u.c. PTO can be attributed to extrinsic effects originating from defects at ferroelectric/electrode interfaces and substrate-induced stress.
The transient current caused by polarisation switching is comparable to the tunnelling current which makes it difficult to directly investigate ferroelectricity at these barrier thicknesses. Based on the main characteristic of FTJ, information on the polarisation orientation is further determined from the effect of the polarisation on the resistance value. Applying a voltage pulse with amplitude higher than the coercive value switches the polarisation in the direction of the field. The resistance can then be measured at low voltages without affecting the polarisation direction. Resistance memory loops as a function of the pulse amplitude are presented and the ON and OFF states are highlighted in Figure 5.8. Tunnelling devices with 12, 9 and 6 u.c. thick PTO barrier and 40×40 $\mu$m$^2$ area were tested at room temperature. A voltage pulse with the amplitude $V_{pulse}$ and 50 $\mu$s width is applied on the Co electrode, then the resistance value is measured at 100 mV. The amplitude of the pulses was increased as shown with the arrows, until saturation was achieved. The ON state when the resistance is low and the polarisation is oriented towards the Co electrode can be obtained by applying negative voltages higher than the coercive value. The OFF state corresponds to higher resistance and polarisation oriented towards LSMO and results from applying high enough positive pulses. Multiple intermediate states

can be obtained when areas of opposite polarity coexist in the film which makes them suitable for applications in memory-resistor (memristor) devices [117]. The 6 u.c. PTO devices present a strong imprint which shows a higher stability in the P↓ state, and the resistive switching occurs at different field compared with the values of coercive field obtained by PFM. The imprint is caused by the asymmetric screening of the electrodes. The P↓ state is closer to the 'as grown' state and has a more stable polarisation which corresponds to the higher value obtained from the TEM analysis. The imprint is weaker for 9 u.c., while in the thickest sample it is also weak, but slightly shifted in the opposite orientation of the field. This could be due to the decreasing effect of the depolarising field. The TER values are within the same order of magnitude for all the thicknesses: 954% for 12 u.c. thick PTO, 304% for 9 u.c. and 453% for 6 u.c. Comparing the TER sign with devices having the same electrodes, it is in agreement with LSMO/PZT/Co [7], but opposite to LSMO/BTO/Co junctions [129].

## 5.2 Transport mechanisms in LSMO/PTO/Co tunnel junctions

In ferroelectric tunnel junctions it is essential for the barrier to be both thin enough to allow tunnelling and thick enough to exhibit ferroelectric properties. In this section particular attention will be given to the case of the critical thickness of PTO, 3 u.c.. Because it lacks a reversible macroscopic polarisation, but does exhibit local dipoles it is expected these devices do not display all the characteristics the thicker junctions do. This could happen because the two resistive states in FTJ (caused by polarisation reversal) can be achieved by applying voltage pulses higher than the coercive field of the film, but when the dielectric breakdown occurs at smaller fields, the polarisation is impossible to switch. In the following experiments, the polarisation is switched by applying voltage pulses with the suitable polarity on the Co electrode: towards the Co top electrode- negative pulses (P↑) and towards the LSMO bottom electrode- positive voltage amplitude (P↓). An AFG function generator is used to apply and set the pulse parameters: 100 s width and amplitudes higher than the corresponding coercive bias of the film. In order to identify the P↑ and P↓ states in the devices, current-voltage curves and current values are measured at low voltages, usually 100 mV, which does not affect the polarisation state.

### 5.2.1 Analysis of the I(V) curves

In this section the existence of genuine tunnelling process through the barriers is demonstrated and the direct and Fowler-Nordheim tunnelling contributions are identified as dominating mechanisms depending on voltage and temperature. First, the quality of the junctions is determined to ensure the measured current results from tunnelling processes through the barrier and not conducting pinholes. For this purpose, Rowell's criteria for MTJ are used [130, 131]:

- the tunnelling current has an exponential decrease with increasing barrier thickness
- parabolic dependence of the differential conductance curves which can be fit with a direct tunnelling model (in this case with Brinkman model for trapezoidal barriers)
- weak insulating-like dependence of the tunnelling current on temperature.

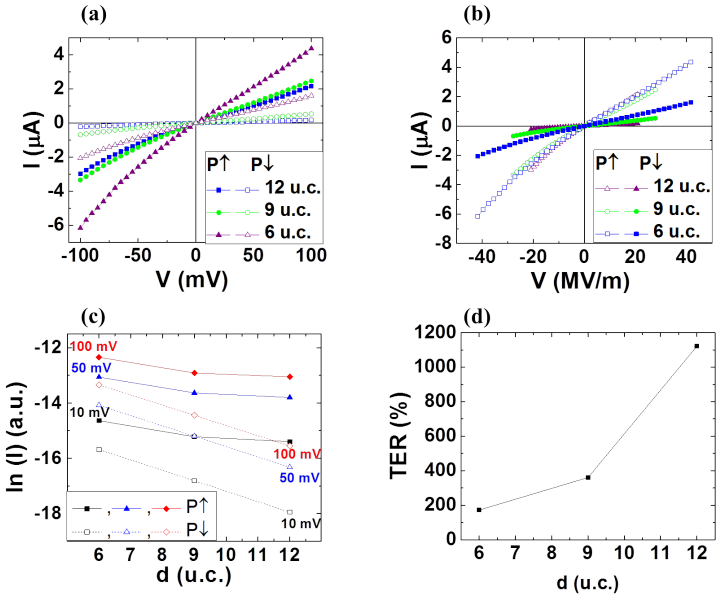


Figure 5.9: a) Current-voltage characteristics in the P↑ and P↓ states for 6, 9 and 12 u.c. PTO tunnel junctions; b) current as a function of applied electric field on the PTO films; c) exponential decrease of the tunnelling current with the barrier thickness at 10, 50 and 100 mV applied bias in P↑ and P↓ states; c) thickness-dependence of TER.

The tunnelling current dependence on the barrier thickness at low applied fields (up to ∼100 mV) and room temperature is extracted from the $I(V)$ curves in figure 5.9 a

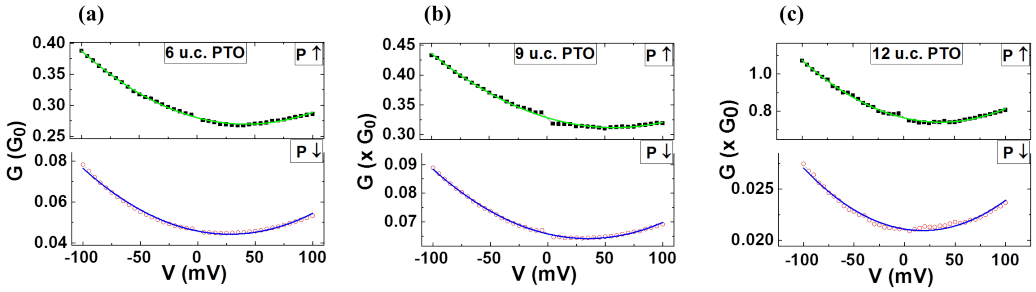


Figure 5.10: Parabolic dependence of the conductance in the two states for: a) 6 u.c., b) 9 u.c. and c) 12 u.c. thick PTO devices, where $G_0$=7.748×$10^{-5}$ S is the quantum conductance.

and shown in figure 5.9 b for the 6, 9 and 12 u.c. PTO samples. Tunnel junctions with 3 u.c. PTO are not included, due to the possibility that the high value of the measured current is determined by the presence of pinholes or film roughness. These cannot be excluded despite the TEM images showing local homogeneous growth because at this reduced thickness variations can have a great influence. Moreover, in junctions with 3 u.c. PTO, no TER effect could be measured. The exponential decrease of the current with the thickness at several fixed values of the voltage (10, 50 and 100 mV) is highlighted in the logarithmic plot of the current in figure 5.9 b. The faster decrease for the P↓ state leads to a higher TER value at higher thicknesses as predicted by theoretical model in [132]. The junction containing 6 layers of PTO yields a TER of ∼170% and increases in 9 u.c. (∼360%) and 12 u.c. PTO devices (∼1120%) (Figure 5.9 c).

The parabolic conductance dependence on the applied bias in the two polarisation orientation states are shown in figure 5.10 a-c up to 100 mV. At higher voltages Fowler-Nordheim tunnelling (FNT) is expected to dominate the tunnelling process [41]. FNT can be identified and distinguished from the direct tunnelling (DT) mechanism with the aid of a ln($J$)=f($d/V$) plot also called Fowler-Nordheim plot. The curved dependence at low voltage values in figure 5.11 is associated in literature with direct tunnelling, while the linear dependence is characteristic to FNT [133, 19]. The transition from direct tunnelling to Fowler-Nordheim tunnelling occurs at ∼1 V in 6 u.c., ∼0.8 V for 9 u.c. and ∼1.05 in 12 u.c. PTO, values obtained from the first derivative of the logarithmic function show the change in the slope. The values are in agreement with theoretical simulations for similar structures in [41] which predict the transition voltage is ∼1 V for thicknesses between 1.2 and 4.8 nm. For the 3 u.c. sample, the applied voltage was limited below 1 V to avoid damaging the barrier and FNT was not observed. The transition denotes the thinning of the

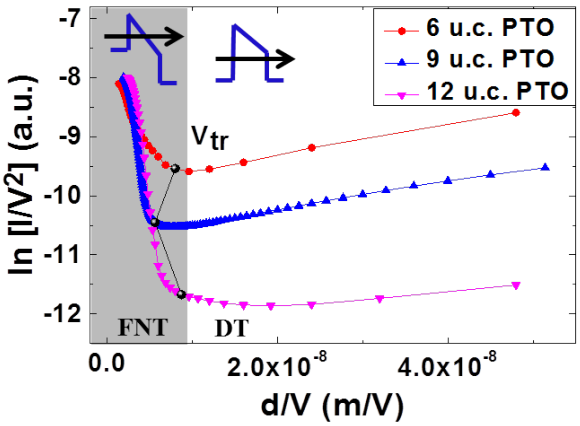


Figure 5.11: Logarithmic representation showing the transition from direct tunnelling to Fowler-Nordheim tunnelling for devices with 6, 9 and 12 u.c. thick PTO and schematic representation of the corresponding barriers and tunnelling process from the LSMO to the Co electrode; the black points represent the transition voltage from DT to FNT mechanisms.

effective barrier thickness. Due to the high applied voltage, as the barrier becomes triangular (shown schematically in figure 5.11 electrons tunnel with a higher rate leading to an increase of the measured current.

The ON and OFF states resultant from applying voltage pulses were investigated at small voltages corresponding to the direct tunnelling regime by acquiring $I(V)$ curves. Brinkman direct tunnelling model (Equation 2.29) provides a good fit for the experimental dependence of the current density on the applied voltage in figure 5.12 a-c. The barrier parameters (effective barrier thickness $d$, effective tunnelling mass $m$, barrier height at the Co and LSMO interfaces $\phi_1$ and $\phi_2$, mean barrier height $\overline{\phi}$ and asymmetry of the barrier $\triangle\phi$) are presented in Table 5.1 for both P↑ and P↓ state and used for the schematic representation of the barriers in figure 5.12 d-f. The parameters were obtained by using FindFit model within the Wolfram Mathematica software. The advantage is that constraints and initial values can be set to ensure the parameters keep their physical meaning within the direct tunnelling model, however, a drawback is the fit cannot consider experimental errors, weighting and does not provide information on the uncertainties.

The TER effect is caused by a few orders of magnitude difference between the low and high tunnelling current at polarisation reversal. The high resistance when the polarisation is oriented towards LSMO (P↓, high resistance, OFF state) is caused by the larger mean height of the barrier compared to when polarisation points towards Co (P↑, low resistance, ON state). One of the origins of the TER effect are

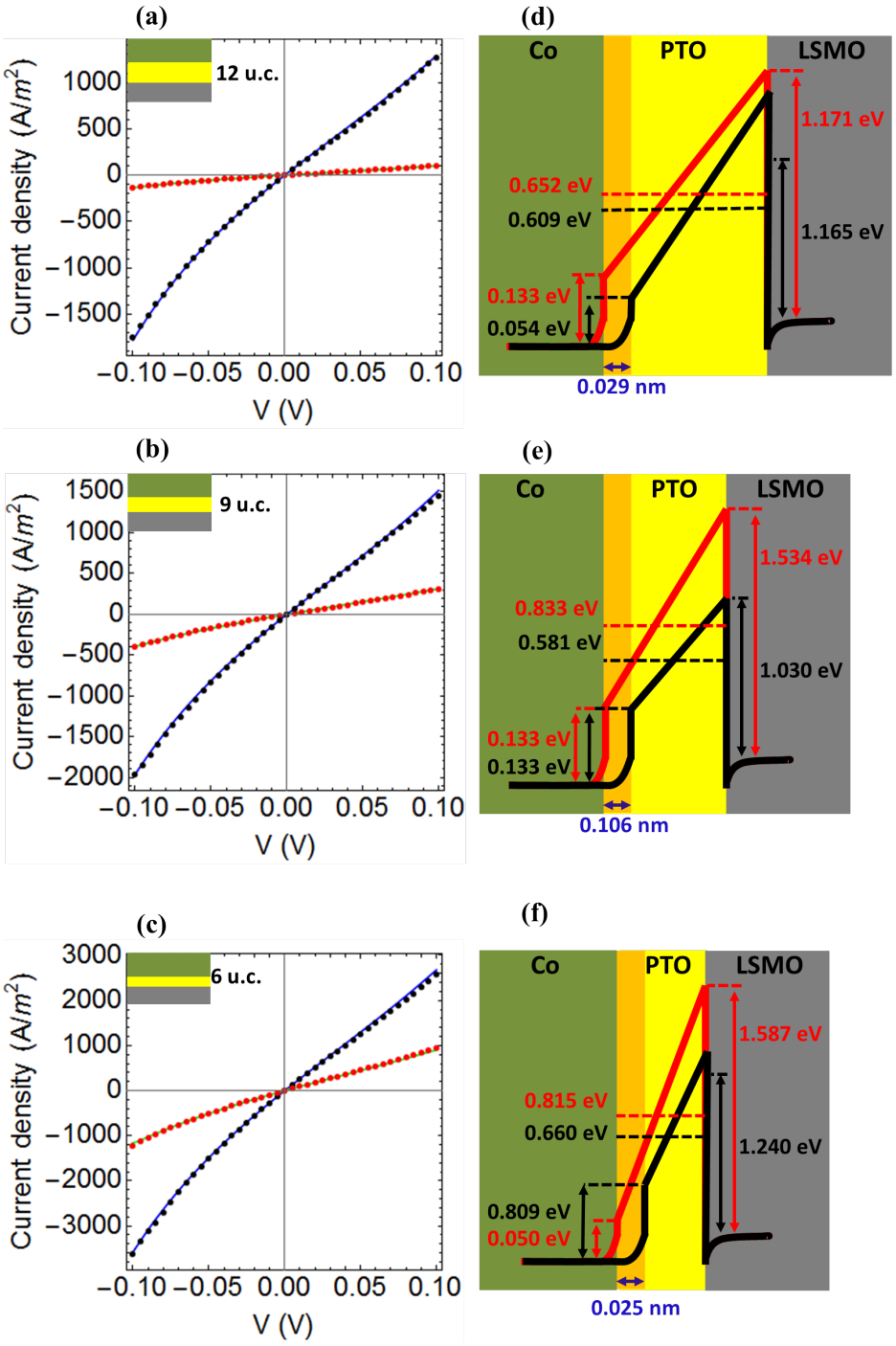


Figure 5.12: a-c) Direct tunnelling fit of the current-voltage characteristics with Brinkman model; d-f) schematics of the barrier profiles indicating the barrier parameters obtained from the fit (Table 5.1) for tunnel junctions containing 12, 9 and 6 u.c. PTO.

Table 5.1: Estimation of the barrier parameters from fitting with Brinkman model for direct tunnelling

| PTO thickness | d (nm) | $m_{eff}$ ($m_0$) | $\phi_1$ (eV) | $\phi_2$ (eV) | $\overline{\phi}(eV)$ |
|---|---|---|---|---|---|
| 12 u.c. P↑ | 4.682 | 0.281 | 0.054 | 1.165 | 0.609 |
| 12 u.c. P↓ | 4.711 | 0.331 | 0.133 | 1.171 | 0.652 |
| 9 u.c. P↑ | 3.605 | 0.506 | 0.133 | 1.030 | 0.581 |
| 9 u.c. P↓ | 3.711 | 0.393 | 0.133 | 1.534 | 0.833 |
| 6 u.c. P↑ | 2.342 | 1.107 | 0.080 | 1.240 | 0.660 |
| 6 u.c. P↓ | 2.367 | 0.987 | 0.050 | 1.587 | 0.818 |

the different electrode screening lengths ($\lambda_{LSMO} > \lambda_{Co}$) on the potential barrier profile [132]. The barrier effective thickness obtained from data fitting vary with 0.029 nm between the two orientations in the case of 12 u.c. PTO, 0.106 nm for 9 u.c. and 0.025 nm for 6 u.c. PTO barrier and cannot be not be solely due to the inverse piezoelectric effect (variation of the order 0.005 nm), but also due to metallisation of the last few layers of PTO [10]. Ab initio studies indicate that when the polarisation is switched up, due to the stronger hybridisation of the $3d$ electronic states of Co with the $3d$ states of Ti and $p$ states of intermediate O ions at the interface, the first layers of the PTO barrier become metallic. Thus the barrier is thicker and electrons tunnel with a lower rate in P↓ state compared to P↑.
Even though the Brinkman model is commonly used for characterising magnetic and ferroelectric tunnel junctions, the values of the barrier parameters can be trusted only to a certain extent. First, the fitting process implies the parameters are interdependent and sometimes can result in unphysical values [134]. Second, the fitting can be problematic due to the characteristics of the physical device such as interfacial roughness [135]. Even the obtained values for effective tunnelling mass are reasonable, their dependence on thickness is not very reliable and probably has no physical meaning.

### 5.2.2 Temperature dependent tunnelling mechanisms

Theoretically, the tunnelling current is independent of temperature, but in practice, thermally activated spin hopping through chains of localised states can influence the electron transfer. It was previously shown that the tunnelling current is voltage-dependent: direct tunnelling occurs at low voltages and by increasing the voltage, FNT becomes dominant. To investigate how the transition between the two mech-

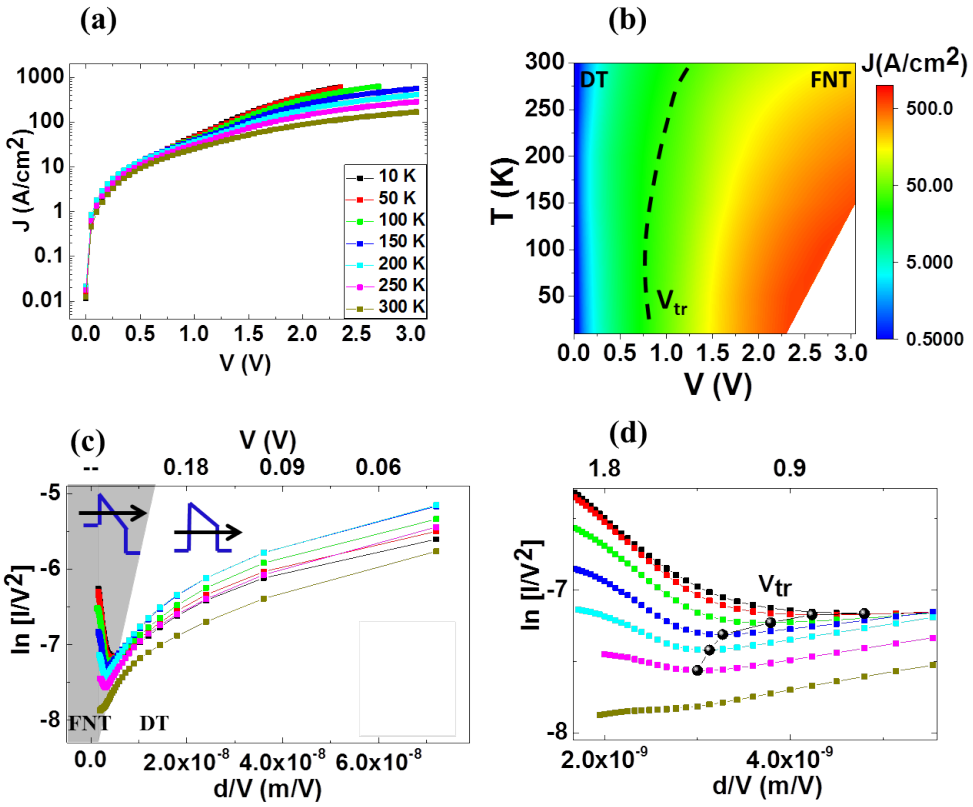


Figure 5.13: a) Logarithmic dependence of current density ($J$) on voltage at different temperatures; b) two-dimensional color map of J with applied voltage and temperature from a); c) logarithmic representation of $I/V^2$ as a function of $d/V$ highlighting direct tunnelling and Fowler-Nordheim tunnelling processes in a tunnelling junction having 9 u.c. PTO and d) magnified plot of c) where the black points represent the DT-FNT transition voltage.

anisms evolves with temperature, $I(V)$ curves acquired for the 9 u.c. PTO tunnel junction were investigated. A change in the slope of the current density can be observed in figure 5.13 a which implies different transport mechanisms at low and high voltages. Figure 5.13 b is the two-dimensional representation of the current density as a function of the applied voltage and temperature and it highlights the DT mechanism at low voltages (blue) and FNT at higher voltages (red) and a diffuse transition between the two. The FNT appears at higher voltages as the temperature reaches 300 K, as confirmed by the Fowler-Nordheim plot in figure 5.13 c. The linear dependence at high bias voltages confirms the Fowler-Nordheim tunnelling mechanism, while the dependence at low values is attributed to direct tunnelling. The FNT becomes dominant at the expense of direct tunnelling at higher voltages

as the temperature increases (0.7 V at 10 K compared to 1.2 V at 250 V). The inset offers a closer look at the transition voltages where the black points mark the values where the slope changes (obtained from the first derivative).

## 5.3 Tunnelling magnetoresistance

Half metallic LSMO is used in spintronic devices due to its high spin polarisation which would lead to a high TMR effect. Even so, the performance of manganite-based tunnel junctions was not very good over the time due to TMR vanishing at temperatures much lower than the Curie temperature of the ferromagnetic electrodes. Due to improvements in device fabrication processes, currently the TMR effect offers a better depiction of the electrodes' intrinsic properties, including at room temperature. In this section, the TMR effect is studied in tunnel junctions with LSMO and Co electrodes separated by 3, 6, 9 and 12 layers of PTO.

### 5.3.1 Low temperature tunnelling magnetoresistance

Ideally, the TMR effect is caused by spin scattering at the barrier/ferromagnets interfaces and is independent of the barrier thickness. In real devices, defects present in the bulk of the barriers and interface quality variation between samples can play an important role in spin transport. At low temperatures and small voltages, direct tunnelling is expected to be the dominant mechanism. This is highlighted by the Arrhenius plot in Figure 5.14 which shows significantly lower activation energy below ∼50 K compared to higher temperatures.

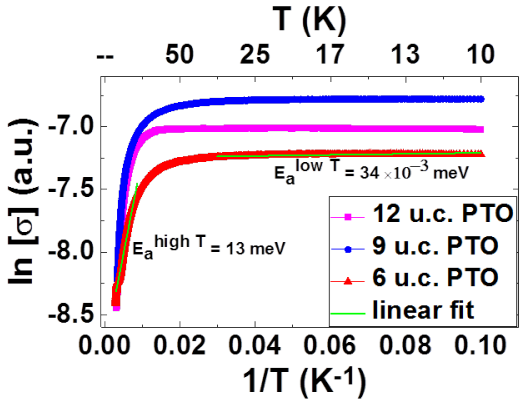


Figure 5.14: Logarithmic plot of the conductivity for devices with 6, 9 and 12 u.c. PTO with linear fit at low and high temperatures (green lines).

Electrical measurements were performed at 10 K on 40×40 $\mu$m$^2$ LSMO/PTO/Co

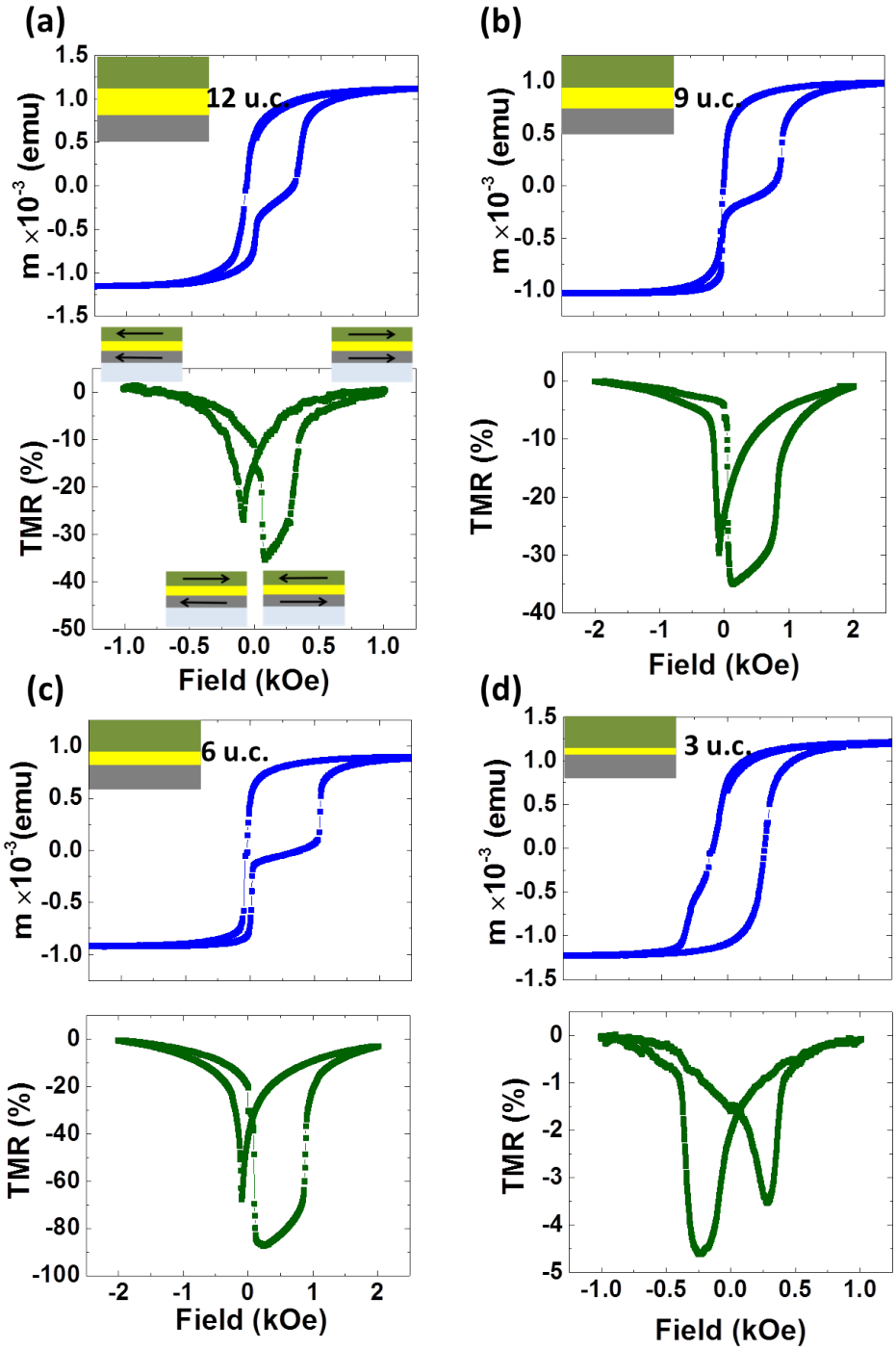


Figure 5.15: Magnetic hysteresis (blue-top) and TMR (green-bottom) measurements for structures with: a) 12; b) 9; c) 6 and d) 3 u.c. thick PTO; in the schematics in a) the arrows illustrate the magnetisation alignment of the electrodes.

devices using a TTP4 Lake Shore cryoprobing station. The current was acquired with a Keithley 6517 voltmeter while the voltage was maintained constant in the tunnelling regime and the magnetic field was sweeped using the superconductive magnet of the equipment. Figure 5.15 (bottom plots-green) shows the hysteretic dependence of the resistance with the magnetic field which outlines what is called an inverse (negative) TMR (calculated with the equation 2.33) for all the investigated thicknesses of lead titanate barrier: the resistance is higher when the electrode magnetisations are oriented parallel to each other ($R_p$) compared to the resistance in antiparallel configuration $R_{ap}$) as seen in figure 5.15. In this case tunnelling is attributed mainly to *d* band electrons instead of *s* electrons considered dominant in normal TMR.

In order to correlate the observed transport effect with the magnetic properties of the electrodes, the total magnetic moments of the entire 5×5 $mm^2$ trilayer samples were measured using a Quantum Design VSM (Figure 5.15, top plots-blue). To avoid differences due to history-dependent character which was observed in the samples, both measurements were performed after cooling the samples in -10 kOe magnetic field. From previous characterisation stages, the lower value of the coercive field is attributed to LSMO and the higher value to Co. Thus the resistance switching is directly caused by the alignment of the electrode magnetisations. The Co magnetic moment contribution is shifted along the positive magnetic field axis due to existing exchange bias in the system. The samples exhibit also a training effect observed in both magnetic and electric measurements which consists in a higher value of the $H_{EX}$ field for the first hysteresis cycling and then reducing and stabilizing for the following cycles [136, 137]. The exchange bias cannot be solely explained by the presence of CoO due to the exchange field variation with the spacer thickness which implies the existence of a coupling mechanism between LSMO and Co. Moreover, in samples with 3 layers PTO, despite the same field cooling history (with -10 kOe), the exchange bias field is negative, unlike in the thicker samples. Another experimental observation worth noting is that at higher temperatures differences between the coercive field values measured electrically on the micrometric tunnelling devices and measured magnetically on the entire samples appear and increase with the temperature.

From Julieres model, the negative TMR is caused by spin polarisations with opposite signs at the interfaces. Due to the robust spin polarisation of LSMO (almost completely polarised in LSMO/STO/LSMO junctions) plus the possible effects of the Co ions (hybridisation with other transition metal ions present in the barrier) at the interface, in LSMO/insulator/Co systems, inverse TMR and changes in the

Table 5.2: TMR sign in tunnel junctions containing LSMO and Co electrodes and Ti-based barriers

| Bottom electrode | Barrier | Top electrode | TMR Comments |
|---|---|---|---|
| $La_{0.67}Sr_{0.33}MnO_3$ | $TiO_2$ | $La_{0.67}Sr_{0.33}MnO_3$ | normal [138] |
| $La_{0.67}Sr_{0.33}MnO_3$ | $TiO_2$ | Co | inverse [138] |
| $La_{0.67}Sr_{0.33}MnO_3$ | $SrTiO_3$ (standard) | Co | inverse [139] |
| $La_{0.67}Sr_{0.33}MnO_3$ | $SrTiO_3$ (oxygen-deficient) | Co | normal [139] |
| $La_{0.67}Sr_{0.33}MnO_3$ | $SrTiO_3$ | $La_{0.67}Sr_{0.33}MnO_3$ | normal [140] |
| $La_{0.67}Sr_{0.33}MnO_3$ | $BaTiO_3$ | Co | inverse [141] |

TMR sign are attributed to the insulator/Co interface. Considering the high quality epitaxial growth of the perovskite films on the STO substrate having $TiO_2$ termination, it is most likely that the PTO film terminates also with $TiO_2$ layer. TMR in tunnel junctions having LSMO and Co electrodes and PTO barrier has the same sign as tunnel junctions with the same thickness $TiO_2$ barrier (Table 5.2) and strongly suggests that the inverse TMR might be the result of Ti-Co hybridisation at the interface and that the termination might be solely responsible for the TMR sign. The nature of the barrier also influences spin transport processes dictating the amplitude of the effect which is higher than in $TiO_2$ [138].

**TMR dependence on barrier thickness**

Ideally, when direct tunnelling is the main transport mechanism the TMR effect is determined by the surface density of states of the electrodes and should not be affected by the barrier thickness. In the case of the PTO barrier under study, the minimum TMR is seen for 3 u.c. ($\sim$-4.5%) PTO film and the maximum in 6 u.c. ($\sim$-87%) and similar intermediary values for 9 to 12 u.c. ($\sim$-36%). Considering there are variations between device performance within the same sample, the TMR is decreasing with the thickness (which is also confirmed in the following sections of the chapter) in junctions with functional ferroelectric barriers and might indicate the presence of additional transport channels apart from spin-dependent tunnelling. The magnitude of the TMR effect was shown to vary with the barrier thickness also in MTJ containing MgO, where it can present oscillations and low variations at small thicknesses [142, 143]. However in this case the sampling interval is not small enough for obtaining detailed information on the TMR dependence on thickness.

### 5.3.2 TMR variation with temperature

The spin dependent tunnelling is caused by the ferromagnetic nature of the electrodes thus it is expected to be directly related to the magnitude of the magnetizations. However, in the past, the TMR effect could not be measured up to the Curie temperature in tunnel junctions containing manganites [144, 145, 146]; an effect attributed to the quality of the fabricated devices which improved over time. TMR was measured in the as grown state for all the samples from 10 K to room temperature with an applied bias of 100 mV. The magnitude of the TMR effect decreases with increasing temperature for all the samples and the maximum value is measured on the 6 u.c. thick barrier sample, shown in detail in figure 5.16 c. The TMR decay with increasing temperature is shown in figure 5.16 for samples with all thicknesses. The plotted values were normalised to the TMR measured at T= 10 K (TMR(10K)). The decrease of TMR is linear and appears to vary little with the PTO spacer thickness, which can be attributed to defects that cause spin-flip scattering at the ferromagnet/barrier interfaces. The magnetization of Co, having a high Curie temperature, is expected to suffer negligible changes in the investigated temperature range [147, 148], therefore the lower TMR at high temperatures is caused by changes in the LSMO magnetisation. The reduced magnetization $M(T)/M(10\text{K})$ of a 5×5 $mm^2$ LSMO sheet from measurement using the SQUID magnetometer is plotted for comparison with normalized TMR in figure 5.16 b. The TMR temperature-dependence does not follow the magnetic moment behaviour due to a much faster decay of the moment at the surface which is where the tunnelling processes occur [149, 150]. Both the surface and the bulk magnetisation follow the Bloch law [151]:

$$M(T) \propto (1 - BT^{\frac{3}{2}}) \tag{5.3}$$

where $B$ is the Bloch coefficient and its value for the surface is generally higher compared to the bulk. The spin polarisation, due to its surface sensitivity, follows the same law causing the TMR to decrease at a higher pace when compared to the magnetisation in the bulk of the electrodes.

Room temperature is the most suitable for evaluating the devices for potential application as memory devices. TMR values are reduced below 10% for 6, 9 and 12 u.c. thick PTO barriers when increasing the temperature to 300 K. These values are in agreement with results in other manganite junctions [152], but lower than in MgO-based junctions [153, 154]. The existing TMR up to room temperature, near the Curie temperature of the LSMO electrode, proves the high quality of the epitaxially grown films and interfaces.

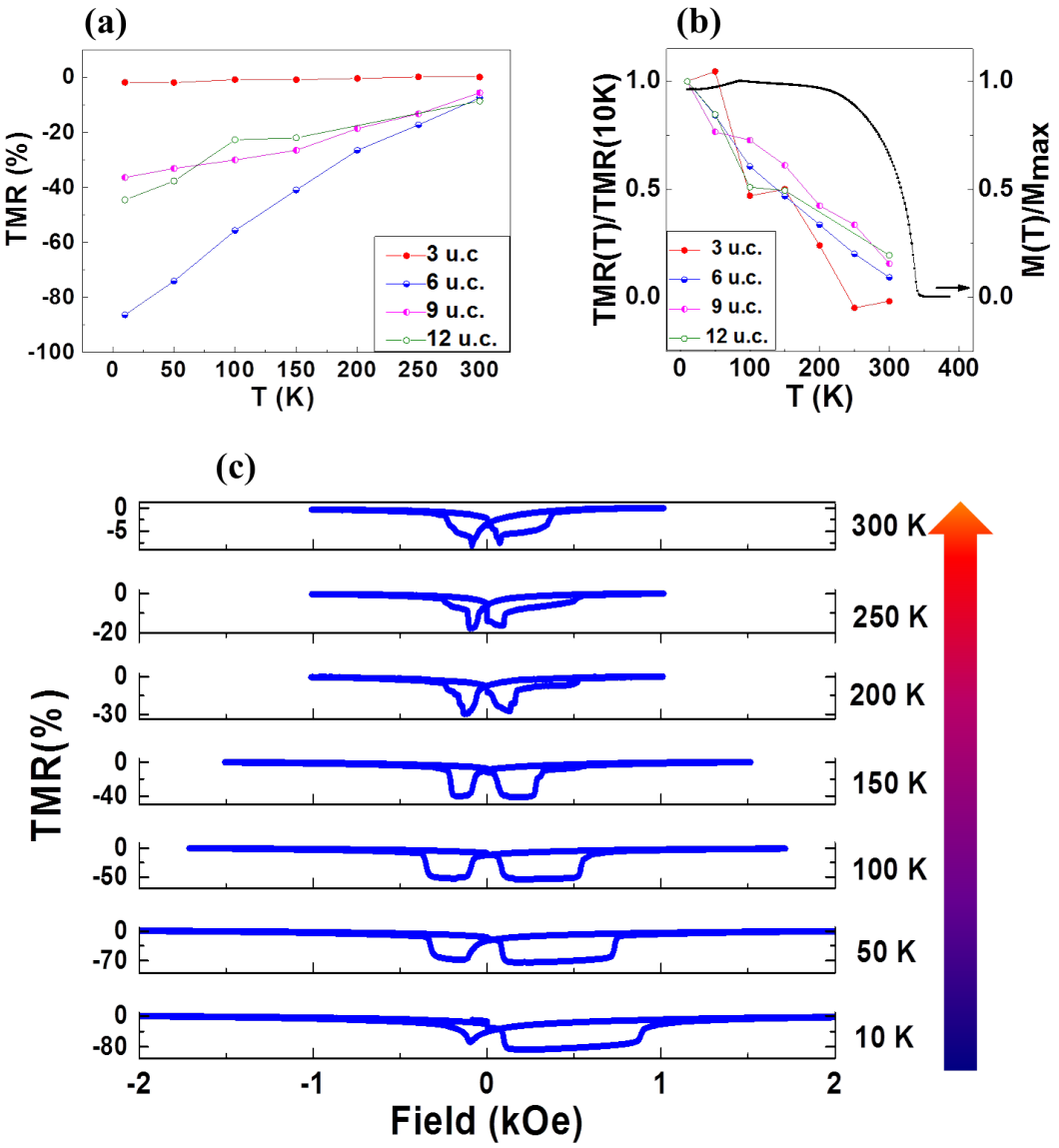


Figure 5.16: a) TMR effect in tunnel junctions with 3, 6, 9 and 12 u.c. PTO; b) reduced TMR values extracted from a) compared to the reduced magnetization of LSMO; c) TMR as a function of temperature for devices with 6 u.c. PTO barrier.

**LSMO/PTO/Co tunnel junctions with 3 u.c. thick barrier**

A different behaviour in terms of electronic transport was observed in junctions containing 3 monolayers of PTO, probably caused by existing conduction channels due to the small thickness combined with one unit cell roughness of the film. While the first two of Rowell's criteria can also be observed in MTJ containing pinholes, the differentiating characteristics from the insulating samples is the high conductance of the junction and its metallic temperature dependence. After attempts to switch a sample with 3 u.c. thick barrier causing dielectric breakdown, current through the junction was measured as a function of temperature resulting in a metallic-like behaviour (Figure 5.17 a). The resulting junction is formed of two ferromagnets connected through nanoscale metallic channels connected in parallel with the channel corresponding to tunnelling phenomena through the insulator [155]. A change in the magnetoresistance (MR) sign takes place at temperatures between 200 and 250 K. From inverse, typical to PTO barriers, the MR becomes normal. The high Curie temperature (325 K) determined from the total magnetic moment of the tri-layers measurements (Figure 5.17) excludes the influence of ferromagnetic-paramagnetic LSMO transition in this range. Moreover, the magnetoresistance measured at 300 K (0.03 % normal MR) is not characteristic to just Co (1.9 % inverse MR) [156, 157]. The behaviour can be described in the strong transmission tunnelling limit within Kim's model which predicts a change in the ballistic magnetoresistance at increasing temperature [158].

## 5.4 Influence of polarization orientation on tunnelling junction transport

Increasing the coupling of electric and magnetic order parameters is a long-standing scientific challenge with great implications in real devices. Small intrinsic coupling has been observed in multiferroic materials and at ferroelectric/ferromagnet interfaces. In multiferroic tunnel junctions this entails the control of electron spins by electric fields and represents a low-power alternative for magnetic writing in spintronic devices [7, 141, 6]. The originating coupling mechanism is an interplay between charge, spin and valency and it can be tailored with the choice of barrier and electrode materials [159].

In LSMO/PTO/Co junctions, the coupling is attributed to the interfacial Ti-Co ion hybridisation, similar to hybridisation processes observed in other systems containing Ti-based barriers and transition element electrodes (Table 5.2). Due to the

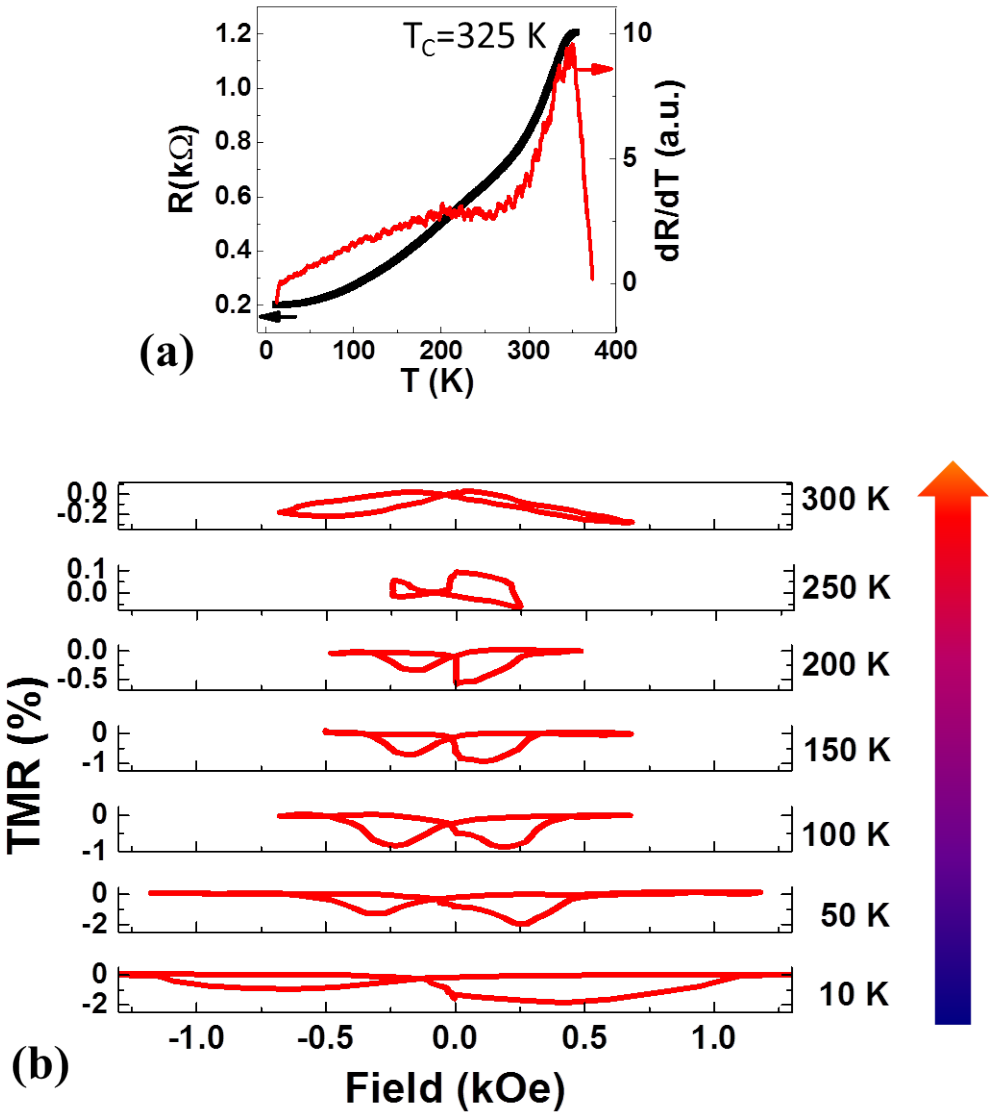


Figure 5.17: a) Resistance of 3 u.c. thick PTO barrier containing pinholes measured with the variation of temperature and b) magnetoresistance loops measured at different temperatures.

reduced number of studies on such devices, the microscopic cause is not fully understood and there is no generalised approach to predict the behaviour of a combination of materials. Thus the experimental measurements are confirmed from case to case by theoretical calculations.
Figure 5.18 illustrates the magnetoresistance curves in the P↑ and P↓ at 10 K which were obtained by applying negative and positive voltage pulses to the Co electrode. The four resulting resistive states are highlighted: 1-P↑ with antiparallel magnetisations, 2-P↑ with parallel magnetisations, 3-P↓ with antiparallel magnetisations and 4-P↓ with parallel magnetisations. The polarisation switching process consists of local displacement of Ti ions in the bulk of the barrier and in the $TiO_2$ layer termination. The Ti cations are shifted in the direction of the applied field and O anions in the opposite direction. Hybridisation of the Ti and Co ions occurs at the interface through the O ions which is affected by the shortening of the bond in the P↑ state and lengthening in the P↓ state and modifies the density of states of the electrodes at polarisation reversal. In the following section, the effect of the ferroelectric polarisation orientation on the spin transport is investigated purely from electric measurements.

### 5.4.1 Thickness and temperature dependence of electronic transport

Theoretically, the current resultant from tunnelling is independent of temperature, but in practice the measured current may vary with temperature due to the contribution of the electron hopping processes. In order to investigate how the ferroelectric polarisation influences the transport properties in the ON and OFF states, the temperature dependence of the resistance is measured. At 10 K, the polarisation was switched towards Co and towards LSMO by applying voltage pulses with suitable polarity. Then the resistances in figure 5.19 were aquired with 100 mV bias while heating the samples with 2 K/min rate. The obtained variations of the resistance are within the same order of magnitude which excludes the oxygen vacancies influence in transport properties according to [139]. The higher resistance in the P↓ state than in P↑ is caused by changes in height and effective thickness of the barrier (as seen in the barrier profiles at room temperature in figure 5.12) and density of states of the metals when the polarisation is reversed. The tunnelling current can be significantly influenced by the change of the barrier effective thickness as predicted theoretically by metallisation processes of superficial PTO layers [10]. Due to the proximity of Ti and Co when polarisation is pointing upwards, the charge transfer is enhanced and a reversible metallisation of the superficial layers in PTO occurs. This mechanism

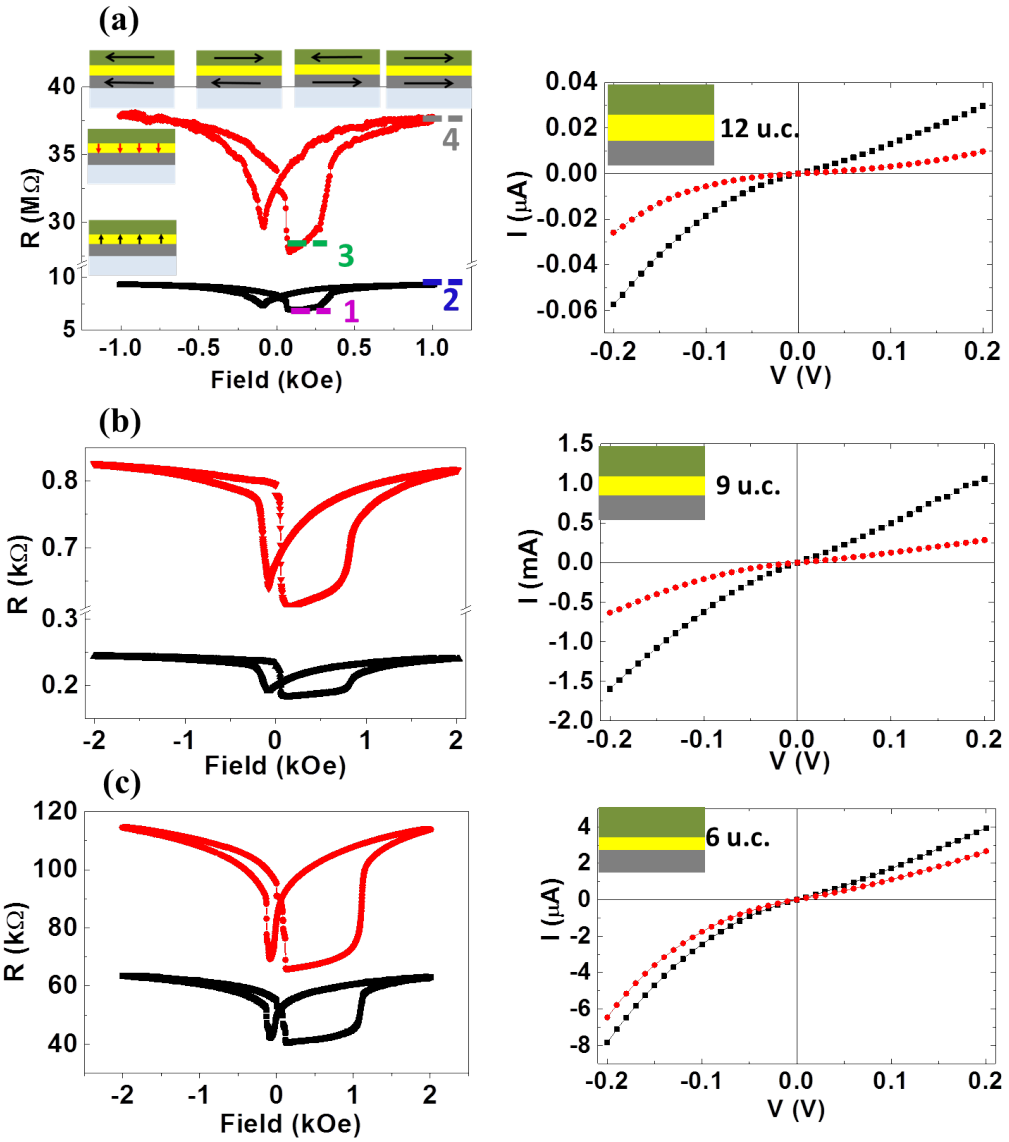


Figure 5.18: TMR measured in P↑ (black plots) and P↓ (red plots) states showing the coexistence of TER and TMR effect in tunnel junctions with a) 12 u.c.; b) 9 u.c.; c) 6 u.c. thick PTO barrier with the $I(V)$ characteristics corresponding to the two states.

may also contribute to the temperature dependence in P↑ state. The processes occurring at the LSMO/PTO interface cannot be excluded completely either. A carrier-mediated field effect has been observed in LSMO/ferroelectric stuctures: the temperature dependence of the LSMO resistivity differs in the accummulation (accummulation of holes when polarisation is pointing away from LSMO) and depletion (when the polarisation is pointing towards LSMO) states [159].

Due to the design of the devices with $40\times40$ $\mu$m$^2$ Co patches and continuous LSMO film, the electrical contacts for PPMS measurements were made by using Pt wires and conductive silver paste on the top Co electrode patch and at the edge of the LSMO film. This causes the current in a device to flow from the top Co electrode through the barrier and then laterally through the LSMO bottom electrode. In the circuit created by the resistances (of the wires, contacts, electrodes and across the barrier) connected in series, if the resistance of the junction is comparable or lower than the sheet resistance of the LSMO, the current could be limited by the electronic transport in LSMO. The shape of $R(T)$ plot in the P↑ state is indeed similar to the sheet resistance of LSMO electrode, with an increasing slope at higher temperatures which might indicate the metal-insulator transition. However, the junction resistance is higher with at least one order of magnitude than that of the LSMO sheet.

The resistance dependence in the OFF state is different for the investigated thicknesses: it peaks at ∼230 K in 6 u.c. PTO junctions, while 9 and 12 u.c. PTO exhibit a minimum below 200 K. The device with 6 u.c. has a metallic dependence up to 230 K where the resistance increases by 100%, then after a metal-insulator transition, the resistance decreases to a higher value than $R$(10 K) at room temperature. The value of $R$(10 K) is reached again at 314 K. The $R(T)$ plot is in agreement with the typical dependence obtained in manganite based tunnel junctions (LSMO/STO/LSMO in [140, 145, 160, 161]; LSMO/STO/Co in [139]; LSMO/$BaTiO_3$/LSMO in [115]; $Fe_3O_4$/STO/LSMO in [162]; $LaBaMnO_3$/STO/ $LaBaMnO_3$ in [163]), which is attributed to inelastic hopping of electrons and treated within the Glazman-Matveev model. A shoulder-like feature resembling the P↓ state dependence can be seen at a slightly higher temperature ∼250 K in the 6 u.c. junctions in P↑ state (Figure 5.19 d). In the 6 monolayers of PTO, two peaks (marked in figure 5.19 c) can be observed at a lower temperature (226 K) for polarisation oriented towards LSMO; and at higher temperature (251 K), fainter and overlapping with the metallic behaviour when polarisation points towards Co. This observation is consistent with the peak shifting of LSMO resistance in LSMO/ferroelectric structures in accumulation and depletion states [159, 164]. Obtained from the differences

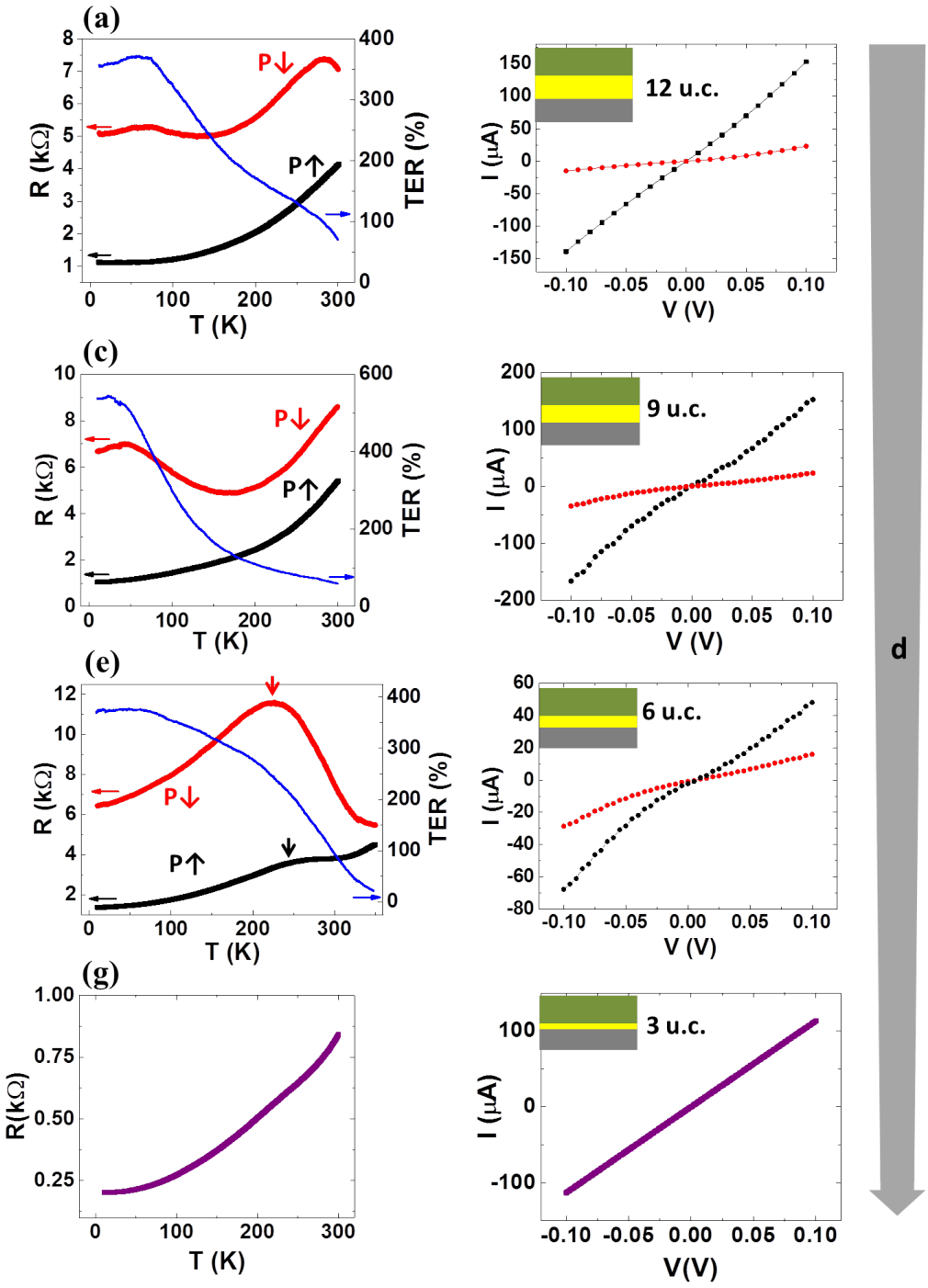


Figure 5.19: Temperature dependence of the junction resistance and calculated TER (left) and current-voltage dependences at 10 K (right) measured on tunnel junctions with a-b) 12 u.c.; c-d) 9 u.c.; e-f) 6 u.c. and g-h) 3 u.c. thick PTO barriers.

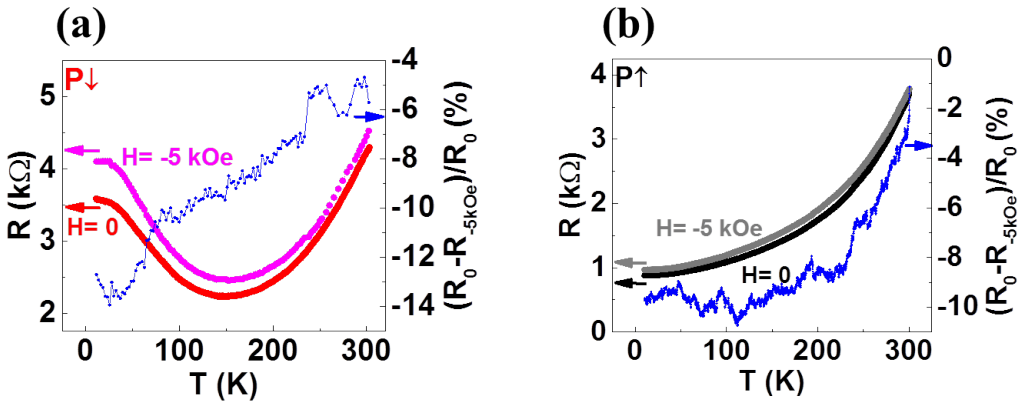


Figure 5.20: Resistance measured in: a) P↓ and b) P↑ states without field and in the parallel magnetisation state at -5kOe field.

between the two states, the TER effect is decreasing faster at high temperatures due to the junction in P↓ state becoming more conductive. In the OFF state, the devices with 9 and 12 layers of PTO exhibit three distinct temperature regimes: first a metallic behaviour up to 40-50 K with a slow increase of resistance; followed by an insulating character up to 150-180 K, more pronounced in the 9 u.c. device and then they have a metallic-like behaviour which almost imitates the dependence in the P↑ state in this range. In both cases, the TER is reduced from lower temperatures, probably due to the increasing role of density of defects in the bulk barrier.

In order to show the trend of $R(T)$ is not due to the states the electrodes settle in, they were also measured in the parallel magnetisation orientation of LSMO and Co under external magnetic field and are shown in figure 5.20 for a junction containing 9 layers of PTO. Due to the variation of the coercive field of both the electrodes with temperature, antiparallel orientation of the magnetisations cannot be continuously studied with temperature. Instead, TMR is reflected by the difference in conductivity at zero (after aligning the magnetisations antiparallel at 10 K) and -5 kOe applied field measured during heating with 2 K/min rate. In both P↑ and P↓ states, applying the field affects just the resistance value, with no significant difference to the overall behaviour compared to zero field measurements.

Usually in manganite magnetic tunnel junctions the tunnelling process is described as a combination of direct tunnelling and additional thermally activated inelastic processes where conduction occurs through chains of localised states within the barrier. Experimental data in this case is characterised with the Glazman-Matveev

(GM) model for the temperature-dependence of the conductance [165, 166]:

$$G = G_{DT} + \sum_{N=1}^{\infty} a_N T^{(N-\frac{2}{N+1})} \tag{5.4}$$

Where $a_N \propto \exp[-2d/(N+1)\alpha]$ are constants depending on the radius of the localised states $\alpha$ and the barrier $d$ and $G_{DT}$ is the direct tunnelling conductance. According to the GM model, direct tunnelling and tunnelling through a single channel (resonant tunnelling) result in elastic tunnelling current, while hopping through $N \geq 2$ channels results in inelastic tunnelling current. In order to investigate the contributions of the inelastic tunnelling channels with the thickness, temperature dependencies of the currents were measured. Limitations such as $eV \ll k_B T$ and also $eV$ and $k_B T$ lower than the barrier height are necessary for $G(T)$ to be valid. Thus low applied voltage (5 mV) in relatively low temperature intervals (10 to 350 K) were used for the experimental determination of conductance for 6, 9 and 12 u.c. PTO junctions (Figure 5.21) which display the same trend as measured with 100 mV (Figure 5.19). The conduction increase is fitted with the GM model and inelastic multistep tunnelling through a different number of impurity levels within the barrier is obtained (Table 5.3). The best fit for the experimental data was found with FindFit using the Mathematica software to allow setting resonable constraints for the parameters. The 6 u.c. PTO barrier can be fitted in good agreement to the model above ~260 K. The number of hopping channels resulting from the fit is $N$=7, indicating a high density of localised states in the barrier. The value is the same as obtained in thicker PZT in (10 u.c. in [9]). The thicker samples exhibit a conductance increase at low temperature which was fitted starting with N=3 and then decreasing to N=2, which is the opposite of the expected behaviour where the contributions of the inelastic channels are increasing with available thermal energy [167, 168]. The low temperature dependence is reproducible for heating and cooling, but no significant conclusion can be drawn since data can be affected by different heating/cooling rates at the extremities of the sampling interval. It is possible that inelastic processes similar to the one observed in 6 u.c. PTO are activated also in thicker samples, above the temperature measurement range. The radius of the localised states is one order of magnitude lower in the sample containing 6 layers PTO ($10^{-2}$ nm) compared to the thicker ones ($10^{-1}$ nm).

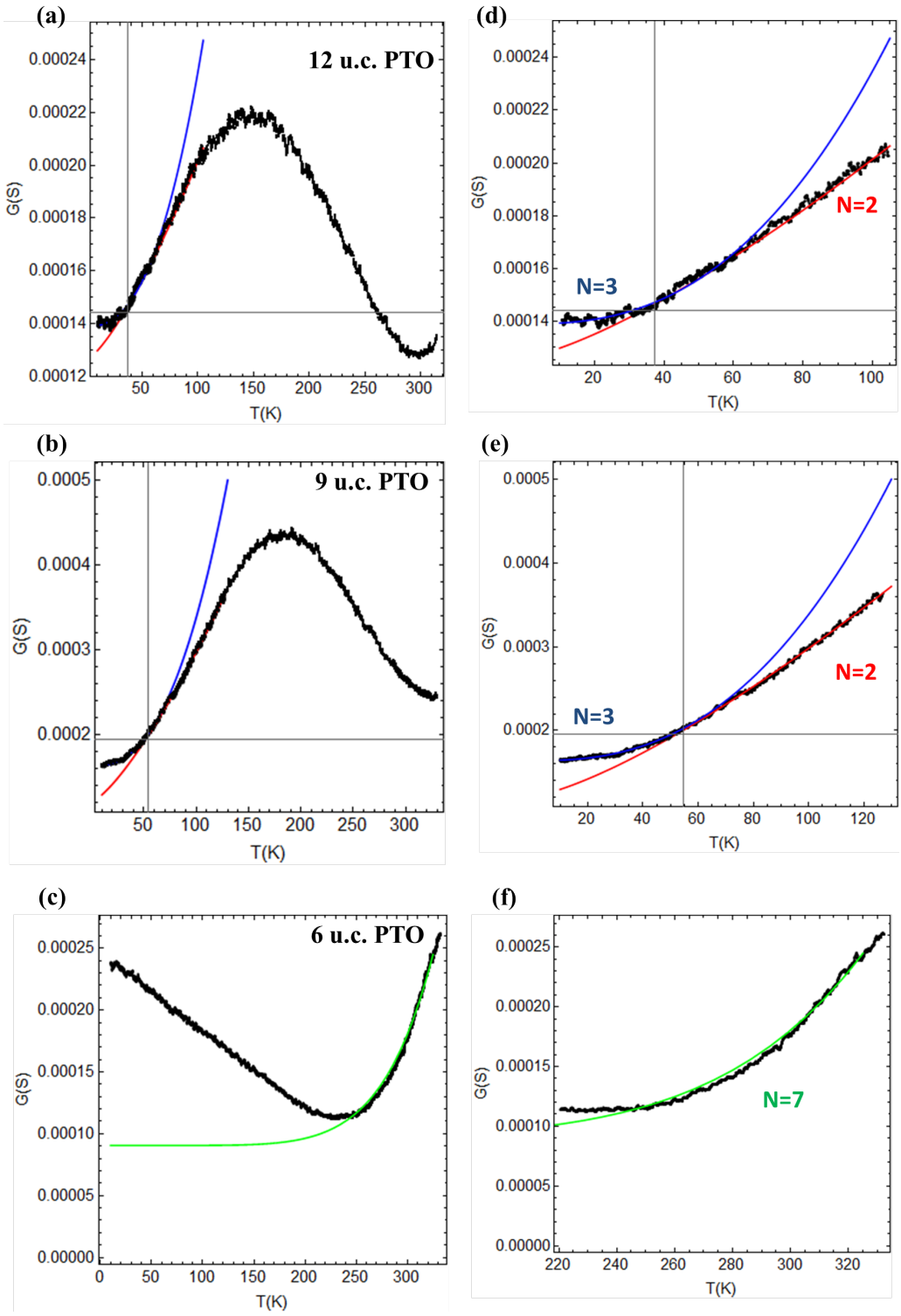


Figure 5.21: Tunnelling current dependence on temperature measured at 5 mV fit with the Glazman-Matveev (GM) model (left) in a) 6, b) 9 and b) 12 u.c. thick PTO devices in the P↓ state; d-f) (right) detailed view indicating the number of channels resulting from the fit.

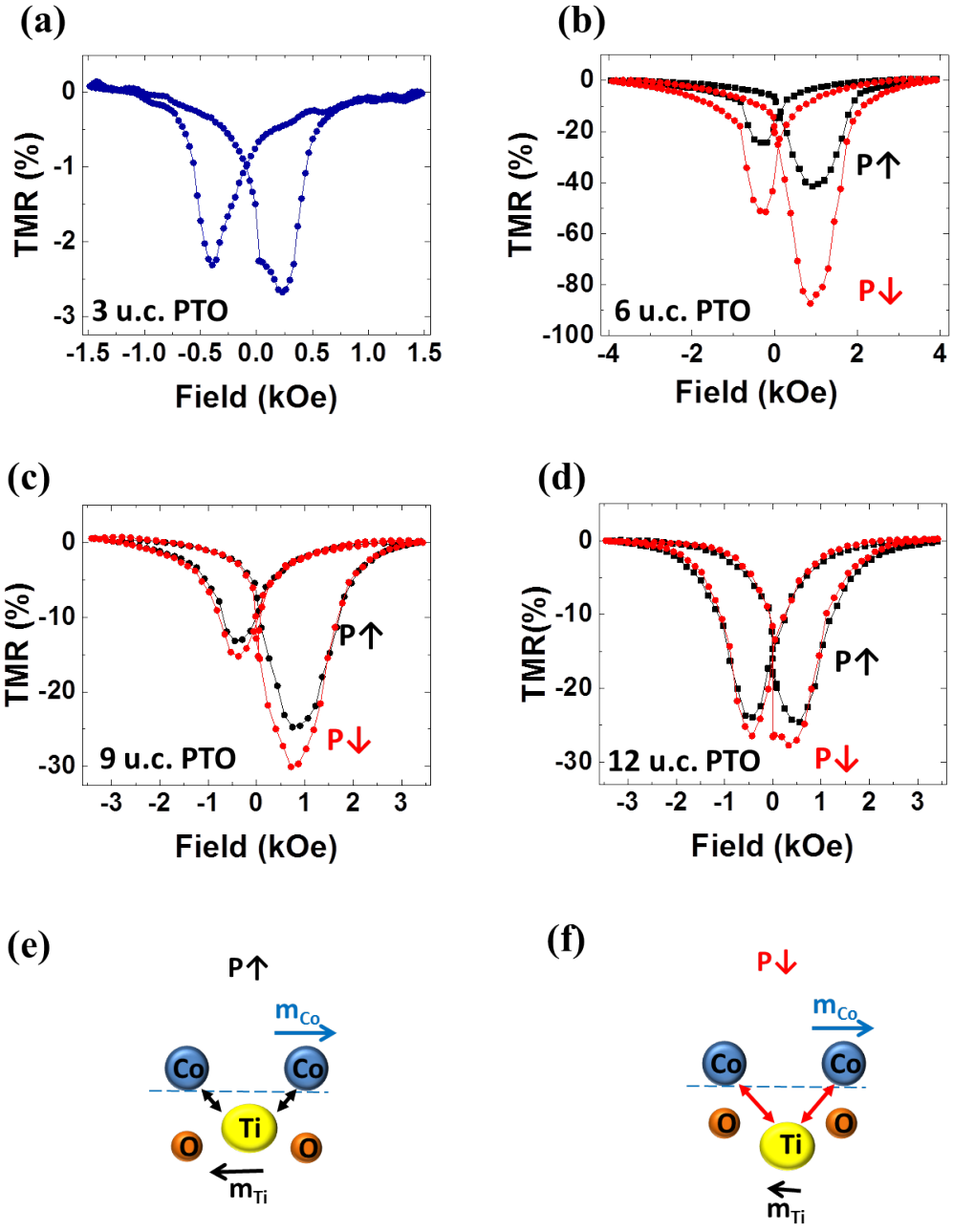


Figure 5.22: TMR loops for a) 3 u.c. (as grown state), b) 6 u.c., c) 9 u.c. and d) 12 u.c. thick PTO in the P↑ and P↓ states; e-f) one of the possible mechanisms to cause polarisation dependent TMR: different magnitudes of the induced magnetic moment on Ti by Co in the two states.

Table 5.3: Estimations of the parameters from fitting with the Glazman-Matveev model

| PTO thickness (u.c.) | $\alpha(m)$ | N | $G_{DT}(\Omega^{-1})$ |
|---|---|---|---|
| 12 | $1.15\times10^{-10}$ | 3 | $1.38\times10^{-4}$ |
| 12 | $2.04\times10^{-10}$ | 2 | $1.26\times10^{-4}$ |
| 9 | $8.92\times10^{-10}$ | 3 | $1.64\times10^{-4}$ |
| 9 | $1.62\times10^{-10}$ | 2 | $1.21\times10^{-4}$ |
| 6 | $1.27\times10^{-11}$ | 7 | $9.05\times10^{-5}$ |

### 5.4.2 Size effect of magnetoelectric coupling

The TMR loops were obtained for the two resistance values corresponding to P↑ and P↓ at 10 K with 100 mV applied voltage (Figure 5.22). A significantly increased negative TMR is obtained in samples with switchable polarisation when it is oriented towards the LSMO electrode. Due to the half-metallicity of LSMO, the robust spin polarisation of the LSMO/PTO interface is less likely than PTO/Co to cause this change. Considering the high crystallinity of the LSMO and PTO films grown on B-site terminated STO substrate, there is a high probability they have the same termination. The local ionic displacement characteristic to ferroelectric polarisation in the lead titanate barrier occurs also for the outermost Ti ions in the $TiO_2$ termination which contributes to interfacial effects (Figure 5.22 e and f). When polarisation is oriented towards the Co electrode (P↑), interfacial Ti ions shift closer to the first layer of Co, the Ti-Co bond shortens causing *d* orbitals to overlap to a larger extent, thus enhancing the *d* orbital hybridisation. The Ti-Co (*d*-*d*) hybridisation is believed to cause the inverse TMR. When the polarisation is reversed (P↓), Ti ions shift away from Co and the bonds become longer and weaker. However, in the studied structure, the magnitude of the TMR effect increases (becomes more negative) as the Ti ions are shifted away from the Co ions in P↓ state.

Experiments and theoretical calculations performed on Ti cations when combined with transition-metal electrodes are summarised in table 5.4. In the case of Ti-Co bonds, Co induces an antiparallel magnetic moment in Ti ($m_{Ti}$). The proximity of Ti to Co increases the magnitude of the magnetic moment [9, 169] and thus the spin polarisation; which would mean measuring a higher TMR in P↑ state compared to P↓. This is noticeable in other MFTJ devices [170], but quite the opposite in the junctions under study. At the LSMO/PTO interface, the innermost Mn ions induce

Table 5.4: Experimentally determined magnetic moment coupling of Ti ions induced by Mn ions from LSMO and Co ions.

| structure | interaction |
|---|---|
| $La_{0.7}Sr_{0.3}MnO_3/BaTiO_3$ | antiparallel moment induced by Mn [174] |
| $La_{0.7}Sr_{0.3}MnO_3/SrTiO_3$ | antiparallel moment induced by Mn [175] |
| $Co/PbTiO_3$ | moment induced by Co ($m_{P\uparrow} > m_{P\downarrow}$) [9] |

an antiparallel magnetic moment on Ti, too. Ferroelectric/LSMO interfaces have been studied with polarisation reversal, but focused just on the orbital degeneracy of Mn ions [171, 172]. Generally it is assumed that no subtantial change occurs at the LSMO/barrier interface in a tunnelling junction. However, a carrier-mediated field effect was observed in LSMO/ferroelectric stuctures: when polarisation is oriented away from LSMO, charge accumulation induces antiferromagnetism in the interfacial LSMO layers [159, 173]. This supports the hypothesis that a higher spin scattering due to antiferromagnetic superficial LSMO layers in the accumulation (P↑) state overcomes the influence of $m_{Ti}$. In this case, PTO would have an increased effect on the Mn ions than BTO due to the higher ferroelectric polarisation [172].
There are no general rules to predict how the exchange (ferromagnetic or antiferromagnetic) coupling of the ions at the electrode/barrier interface affects the spin polarisations. For example, antiferromagnetic exchange can characterise both positive and negative spin polarisations. In LSMO/$SrTiO_3$ and LSMO/$BaTiO_3$, Mn induces an antiparallel magnetic moment on Ti (Table 5.4), LSMO/STO being commonly used as a reference for the positive robust spin polarisation in LSMO/FE/FM tunnel junctions. The hybridisation process of the $Ti^{4+}$ ions causes a non-zero occupation of the $d$ orbitals which otherwise would have the electron configuration of Ar. At the same time, at interfaces containing Ti and other more than half-filled $d$ orbital ions (PZT/Co, BTO/Fe) the antiparallel magnetic moment induced on Ti is associated with a negative spin polarisation used for explaining the inverse TMR. Therefore, a generalised model is needed to predict the type of interaction and TMR in a tunnel junction device. For this purpose, the Goodenough-Kanamori rules [176, 177, 178] can be used if the tunnelling process is seen as a virtual electron transfer through the junction. They consider the wave function of the $d$ orbital ions extending into the neighbouring ions which leads to exchange interaction. Depending on the occupation of the $d$ orbitals in the magnetic ion-ligand-magnetic ion (in this case Ti-O-Co), a parallel or antiparallel magnetic moment can be induced through hybridisation.

However, the electronic occupation of the orbitals at the interface is non-intuitive and the rules can offer sensible explanations only when combined with more investigations [171, 172]. In the junctions under study, during parallel alignment of the magnetisations, at the Co/PTO interface, Ti (with less than half-filled $d$ shell in $Ti^{2+}$ state and empty $d$ shell in $Ti^{4+}$ state) spin ordering would favour the transfer of an electron with antiparallel spin from Co (having more than half filled $d$ shell), determining a larger value of the resistance in parallel than in antiparallel alignment. Even though the rules provide a simplistic explanation for interface effects, they can not explain the inverse TMR in tunnelling devices without deeper understanding of energy level occupation. The sensitivity of TMR on polarisation orientation can be quantified using the tunnelling electro-magnetoresistance:

$$TEMR = \frac{TMR(P\downarrow) - TMR(P\uparrow)}{TMR(P\uparrow)} \tag{5.5}$$

where TMR($P\downarrow$) is the absolute value of the TMR when the polarisation is pointing towards the bottom LSMO electrode and TMR($P\uparrow$) corresponds to polarisation towards the top Co electrode. The values in the LSMO/PTO/Co structure are lower compared to MFTJs containing barium titanate (450% in [6]): TEMR ratio reaches a higher value in the thinnest functional MFTJ (higher than 100%) compared to values for 9 u.c. (21.5%) and 12 u.c. PTO junctions (14.1%).

### 5.4.3 Tunnelling magnetoresistance dependence on applied bias

Comparison of the spin transport properties between the samples with different barrier thicknesses was made by TMR measurements acquired with 100 mV applied dc voltage. However, the TMR can be affected [179] and even reversed [20, 139, 180] by the reading voltage. Moreover, by making use of the high theoretical spin polarisation of LSMO, the voltage-dependence of the magnetoresistance can be used to probe density of states of Co near the Fermi level [35]. In order to investigate this aspect, TMR values were extracted from magnetic field sweeps performed at fixed voltages and plotted in figure 5.23.

In devices containing 3 u.c. PTO films, the TMR is slightly asymmetric and decreases in magnitude with increasing amplitude of the voltage. The voltage-dependence resembles the symmetry observed in MgO-based junctions [179], LSMO/ALO/STO/Co [180] and in oxygen defficient LSMO/STO/Co tunnel junctions [139], while the thicker samples have a similar behaviour to the standard LSMO/STO/Co junctions for both polarisation orientations. The latter dependence usually infers the tunnelling process is dominated by $d$ electrons. In the case of 6 monolayers PTO

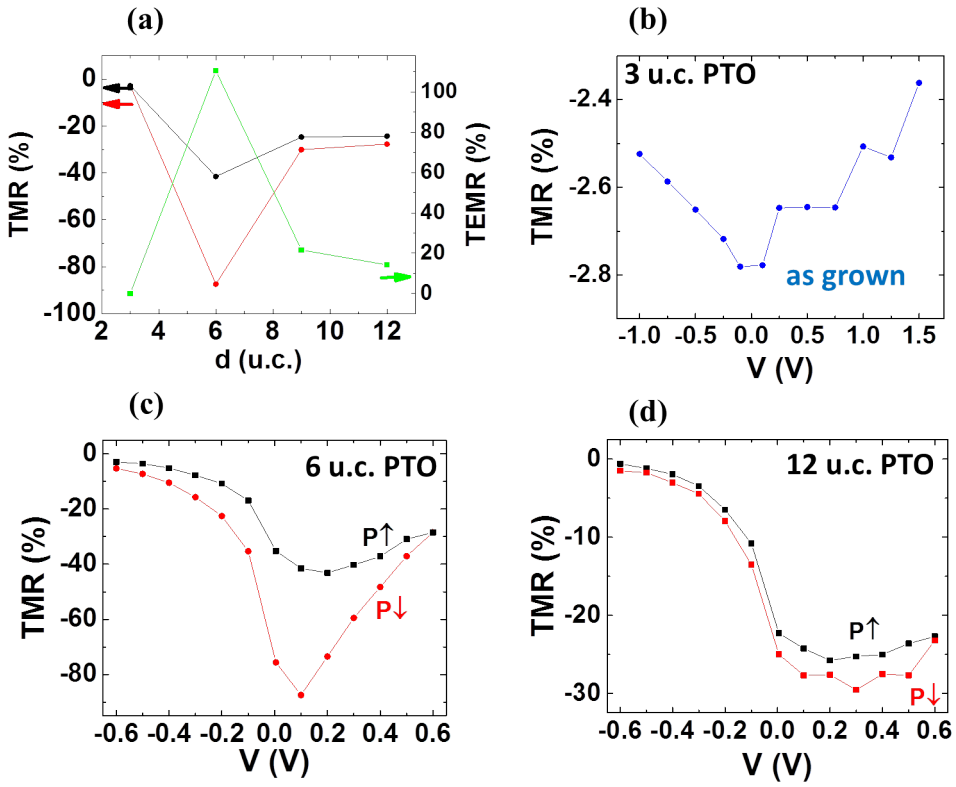


Figure 5.23: a) TMR magnitude in P↑ (black) and P↓ (red) states depending on barrier thickness at 10 K (left) and calculated TEMR (right-green); voltage-dependence of TMR for: b) 3 u.c., c) 6 u.c. and d) 12 u.c. thick PTO.

devices, it can be seen in figure 5.23 c that the TMR reaches the largest magnitude at ∼100 mV for all polarisation orientation configurations. In the antiparallel magnetisation state, at low voltages the tunnelling occurs between the LSMO $e_g$ majority spin band and the Co $d$ minority band, determining the inverse TMR. The maximum TMR is attributed to tunnelling with a high probability between the LSMO majority spin band and the peak in the DOS in the Co minority spin band [180]. The TMR dependence is slightly broader and the maximum value is obtained at higher value in the thickest samples, 300 mV compared to 150 mV in 6 u.c. PTO. TMR dependence on applied voltage is very similar in the two orientations of ferroelectric polarisation.

The effect of partial switching of the polarisation is investigated on spin transport properties in the case of the functional device with thinnest and thickest PTO. The polarisation is gradually reversed by applying pulses with increasing amplitude in order to obtain intermediary resistive states and then the resistance is measured

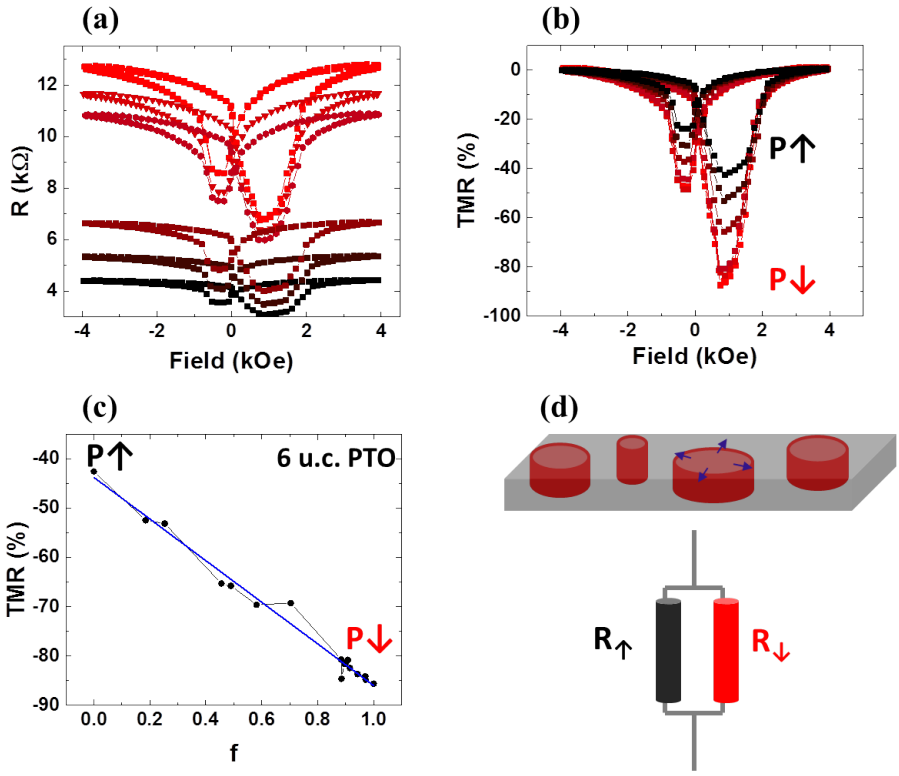


Figure 5.24: a) Intermediary resistance states after partial polarisation switching with increasing voltage amplitude pulses in devices with 6 u.c. PTO barrier; b) variation of TMR between P↑ and P↓; c) TMR as a function of f-the fraction of domains having polarisation towards LSMO electrode, fitted with a linear function (blue line); d) schematics of the contribution of domains to the junction resistance during switching, as resistances connected in parallel.

at 100 mV (Figure 5.24 a) for 6 u.c. PTO. The amplitude is increased so there is a noticeable change in the resistance until the polarisation in the junction is completely switched. The large TEMR effect in the junction containing 6 u.c. PTO makes the variation of TMR evident during polarisation reversal. The initial stages of polarisation switching process, nucleation and forward fast growth of the domains across the ultra-thin film most likely occur within the first applied pulse. Then the slower sideways growth of the domains directly causes the Ti-Co bonds to elongate at the interface on expanding areas proportional to the P↓ fraction (Figure5.24 d). It is assumed that $180^o$ domains coexist, with minimum contribution from vortices and complex structures and when the domains are switched progressively from P↑ ($f$=0) to P↓ ($f$=1), the intermediary states are characterised by a certain fraction $f$ and limited by the ON and OFF states [181]. The junction resistance is equivalent

to domain resistances in P↑ state (R↑) and P↓ state (R↓) connected in parallel (Figure 5.24 d). In figure 5.24 b the TMR effect increases from the value characteristic to the P↑ state to the maximum value in P↓ (Figure 5.24 b and c).

$$\frac{1}{R} = \frac{f}{R\downarrow} + \frac{1-f}{R\uparrow} \tag{5.6}$$

The TMR magnitude represents a cumulative effect of the Co-Ti bonds with different lengths over the entire interface and is proportional to the fraction $f$ of the switched areas. This result shows that the TMR can be tuned by manipulating the ferroelectric domains in the barrier.

### 5.4.4 Temperature-dependent magnetoelectric coupling

Analysis of the temperature-dependent tunnelling properties and magnetoelectric coupling are performed on devices with 9 u.c. barrier. The magnetic field-dependence of the resistance is determined from 10 K to room temperature in 50 K steps (Figure 5.25). The polarisation is switched by applying 50 $\mu$s wide pulses with 5 V amplitude, then the low and high resistances are measured in the direct tunnelling range with 100 mV. TMR magnitude decreases with increasing temperature down to 2% at room temperature and becomes negligible at T=330 K, near the Curie temperature. The values of the coercive fields of both Co and LSMO given by the resistance switching become lower at room temperature ($H_{Co}^{electric}$=140 Oe) but they are significantly higher compared to the ones obtained from SQUID magnetic measurements ($H_{Co}^{magnetic}$=30 Oe). The four resistive states (determined by parallel and antiparallel magnetisation alignment in combination with the polarisation oriented towards LSMO or Co) corresponding to the presented TMR loops are summarised in figure 5.25 b.

Figure 5.25 c presents the decay of the TMR effect with the temperature for the P↑ and P↓ states in devices with 6 u.c. and 9 u.c. thick PTO barrier. As demonstrated previously at low temperatures, the spin polarisation can be modulated by the ferroelectric polarisation. As the temperature rises, the two samples behave differently, suggesting the influence of polarisation becomes weaker when approaching room temperature in the thicker sample, while in the thinnest its effect increases. The TEMR increases from 21% at 10 K, peaks at 150 K (940%) and then decreases to 4% at room temperature. The peak of the TEMR coincides with the broader minimum corresponding to the temperature dependence of the resistance in the P↓ state. As the temperature increases, the Ti ions are shifted on smaller distances in the unit cell [182], thus the fading of the effect.

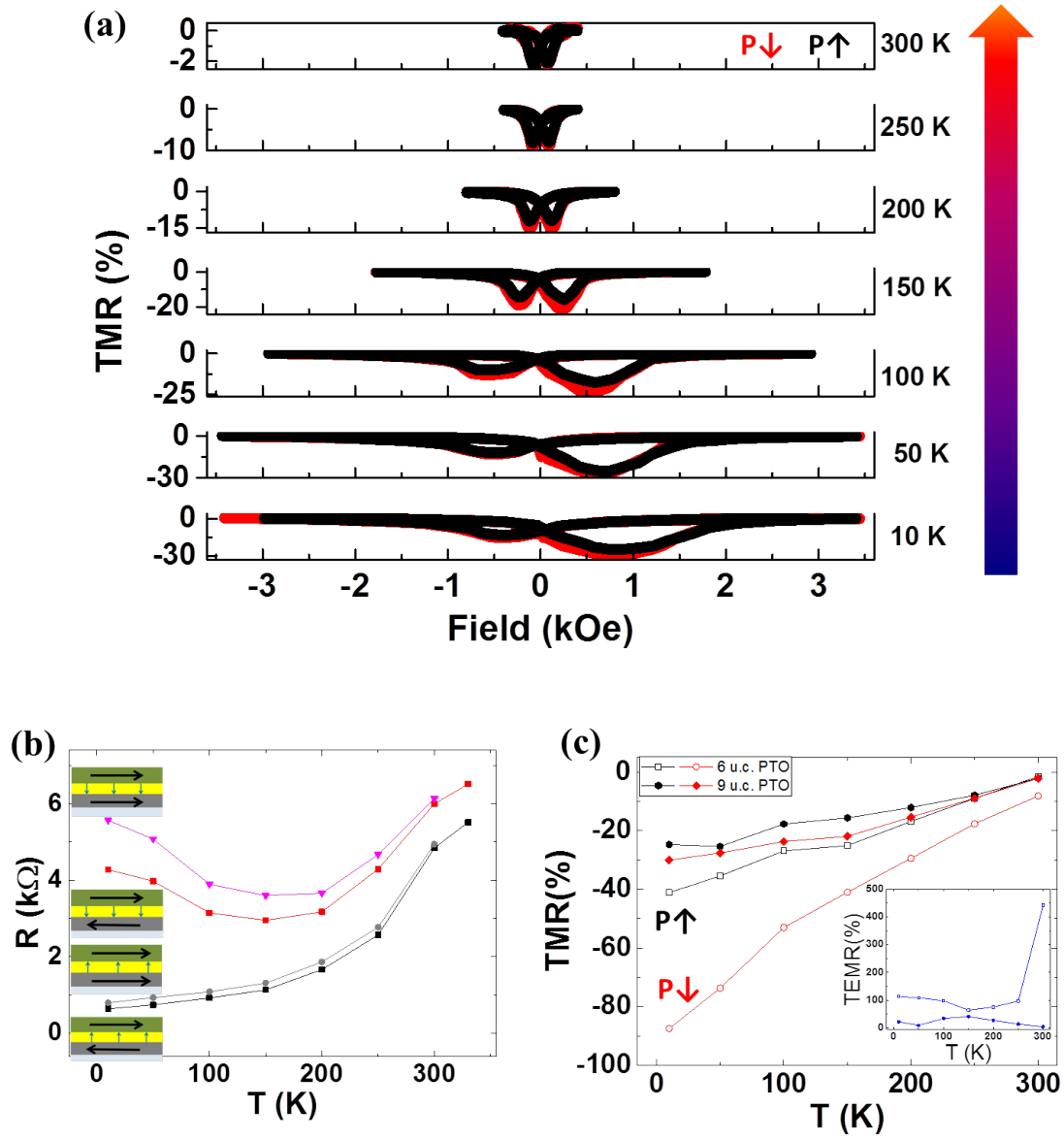


Figure 5.25: a) TMR curves measured in the P↑ (black) and P↓ (red) states with increasing temperature for tunnel junctions with 9 monolayers of PTO; b) variation of the resistive states (orientation of magnetisation and polarisation shown schematically) corresponding to the TMR in a) and c) TMR in P↑ and P↓ states of 9 u.c PTO (filled symbols) compared to 6 u.c. PTO (empty symbols); inset: TEMR variations with temperature for the two samples.

## 5.5 Summary

This chapter highlights the size effect in LSMO/PTO/Co multiferroic tunnel junction properties using films with 3, 6, 9 and 12 monolayers of PTO. Changes in the domain structure were observed with reducing thickness of the PTO barrier by analysing the ionic displacements, and local polarisation was observed down to 3 u.c.. However, in real devices containing 3 layers of PTO, the polarisation cannot be switched, which indicates this is the critical thickness of PTO in the case of positive in-plane strain imposed by the STO substrate.

Four resistive states characteristic of multiferroic tunnel junctions were obtained in the 6, 9 and 12 u.c. thick PTO: two states due to the switching of the polarisation orientation in the barrier and two additional states due to the relative orientations of the electrode magnetisations (also in 3 u.c.). The TER and TMR effects reduce with increasing temperature, but both can still be measured at room temperature (near the Curie temperature of LSMO) due to the good film and interface quality. Polarisation-dependent spin transport is observed and weakens at high temperatures and in thick samples. Partial polarisation switching results in an intermediary TMR value between the TMR corresponding to ON and OFF states. From experimental observations, the mechanism that allows tuning the TMR by polarisation reversal is due to charge accumulation effects at the LSMO/PTO interface, rather than to the magnitude of the induced magnetic moment on Ti at Co/PTO interface.

The TMR obtained in LSMO/PTO/Co tunnel junctions is inverse to that in LSMO/$TiO_2$/Co junctions, underlining the importance of the barrier termination on the TMR sign, but also the importance of the barrier nature on its magnitude. In comparison with LSMO/PZT/Co, the mechanism acts contrary to the expectations of TMR modulation with polarisation reversal. Separate investigations on the influence of Zr ions are necessary for understanding the contributions of Zr and Ti ions in PZT.

# Chapter 6

# Multiferroic tunnel junctions with PZO barrier

Bulk lead zirconate ($PbZrO_3$, PZO) is a typical antiferroelectric. Due to its field-induced ferroelectric polarisation, when used as a thin tunnelling barrier, the mechanisms present in ferroelectric tunnel junctions should also dictate its behaviour. There are no reports so far on tunnelling junctions containing PZO barriers, even their characteristics could lead to obtaining devices with novel properties. This chapter presents original work on $La_{0.7}Sr_{0.3}MnO_3$(LSMO)/$PbZrO_3$(PZO)/Co antiferroelectric tunnel junctions (AFTJ) which at high fields exhibit a high tunnelling electroresistance (TER) effect determined by the non-polar (AFE) to polar (FE) and polar to non-polar transitions, equivalent to the polarisation switching in FTJ. Indeed, further improvements on the stability and reliability of the junctions are necessary in order for antiferroelectric tunnel junctions to be considered for applications on a larger scale.

Experiments have shown that multiferroic interfaces can be obtained when titanate barriers are combined with ferromagnetic electrodes containing transition elements [6, 170, 173], but the mechanisms are not fully understood. For example, control of spin transport was achieved using the ferroelectric polarisation of $PbZr_{0.2}Ti_{0.8}O_3$ (PZT) in LSMO/PZT/Co and was attributed to the interaction between the interfacial Ti and Co ions [7]. To understand the contribution of the Zr-Co interaction, the influence of polarisation switching in LSMO/PZO/Co junctions on spin transport is investigated at low temperatures. Zr ions are suggested as the origin of the observed effect, as a magnetoelectric coupling is detected which affects the TMR value and sign similar to PZT and much different than in PTO junctions.

## 6.1 Antiferroelectric tunnel junctions at room temperature

In magnetic tunnel junctions TMR effects of the order of $10^3$% [1] can be obtained which are modulated by the magnetisation orientation of the ferromagnetic electrodes. If the oxide barrier is replaced with a ferroelectric, its spontaneous polarisation will influence the ferroelectric/electrode interfaces and therefore the electronic transport through the junction. By switching the polarisation orientation, ON/OFF current ratios of $10^4$ and TER effects of $10^6$% can be measured [115, 183]. By using simultaneously ferromagnetic electrodes and a ferroelectric barrier, both TER and TMR concepts are present in the same device which by its four resistive states enables encoding of additional information. In FTJ the ferroelectric polarisation is typically controlled by electric field and in MTJ the magnetisations are controlled by magnetic field, while in the resulting multiferroic tunnel junctions an interfacial magnetoelectric coupling was observed which could lead to multi-field control over the junction resistive states [6].

Antiferroelectrics, similar to antiferromagnets, posses the order parameter at a microscopic level. The neighbouring stack of opposite dipoles cancel each other and in the absence of external fields result in zero macroscopic polarisation and magnetisation, respectively. When an external electric field is applied, above a certain value the dipoles orient in the direction of the field and the AFE phase becomes FE. The process is characterised by a double hysteresis $P(E)$ loop. Due to their volatile nature, both antiferroelectrics and antiferromagnets have not been considered for data storage, until the recent successful case of antiferromagnets [184]. Even though antiferroelectrics have been used as artificial terminations in FTJ to reduce fatigue and increase the TER effect, no results have been reported so far on self-standing AFE tunnel junctions [185, 8].

In this section it is shown that the non-polar AFE to polar FE transition driven by applied electric field determines the existence of a double-hysteresis loop in the tunnelling current, leading to a TER effect of seven orders of magnitude. The amplitude of the effect is determined by the low current density in the OFF state associated with a high barrier height and a considerably higher ON current density caused by polarisation-induced changes in the barrier profile.

Similar to the ferroelectric case, when the AFE barrier is thin enough, tunnelling current can be measured though the junction at low fields. This occurs due to the zero macroscopic polarisation which would cause negligible polarisation-induced lowering of the electronic barrier, as described in [132]. At the value of the for-

ward bias where the AFE-FE transition is induced the local dipoles are oriented in the direction of the field determining a net macroscopic polarisation. In this process surface charges at the now ferroelectric surface are created and screened by the electrodes, affecting the electrode/barrier interface and lowering the effective electronic barrier [186]. The concept is shown schematically in figure 6.1. The double hysteresis loop where the forward and backward bias are associated with the current switches to ON (high current) and OFF (low current) states. While in ferroelectrics the ON and OFF states are remnant, antiferroelectrics are in OFF state at low voltages and the ON state is volatile. In orded to prove this concept,

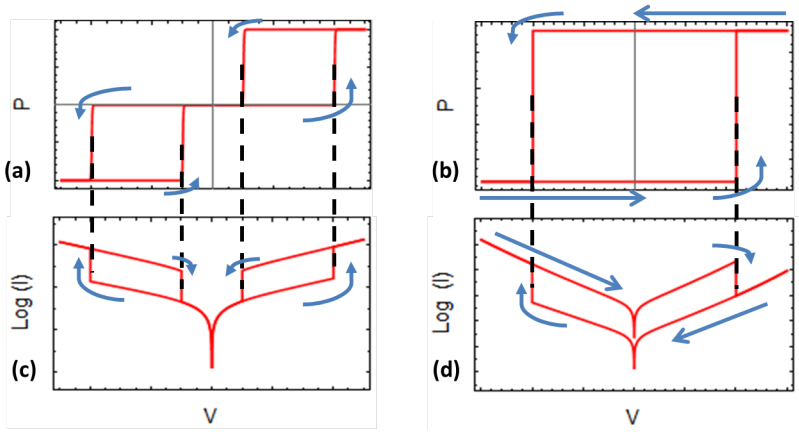


Figure 6.1: Schematics of: a) antiferroelectric double $P(E)$ hysteresis loop in analogy with b) ferroelectric $P(E)$ hysteresis loop; c) expected TER effect caused by polarisation orientation in antiferroelectrics and d) in ferroelectrics.

$La_{0.7}Sr_{0.3}MnO_3/PbZrO_3/Co$ antiferroelectric tunnel junctions were fabricated with different thicknesses ranging from 11 u.c. to 27 u.c. Thicker PZO films were also grown to ensure the obtained properties are in line with previous work on thicker films [187]. Figure 6.2 shows the current-voltage dependences in AFTJ with PZO barriers having 11, 16, 22 and 27 u.c. measured using a Keithley 2635A source meter. The current is low, in the OFF state at low voltages. As the field increases the AFE-FE forward transition is induced causing the tunnelling current to increase several orders of magnitude. At this point, the polarisation in PZO is oriented by the applied electric field and induces a significant change of the electronic barrier at the interfaces. The changes of current between the two states are induced by the forwards (AFE-FE) and backwards (FE-AFE) switching in a manner resembling the predicted shape from figure 6.1. TER values of $10^9$% and ON/OFF current ratios of $10^7$ are obtained from tunnelling current density rising from $10^{-6}$ A/cm$^2$ in the AFE state to 10 A/cm$^2$ in the FE state. This value is much higher than

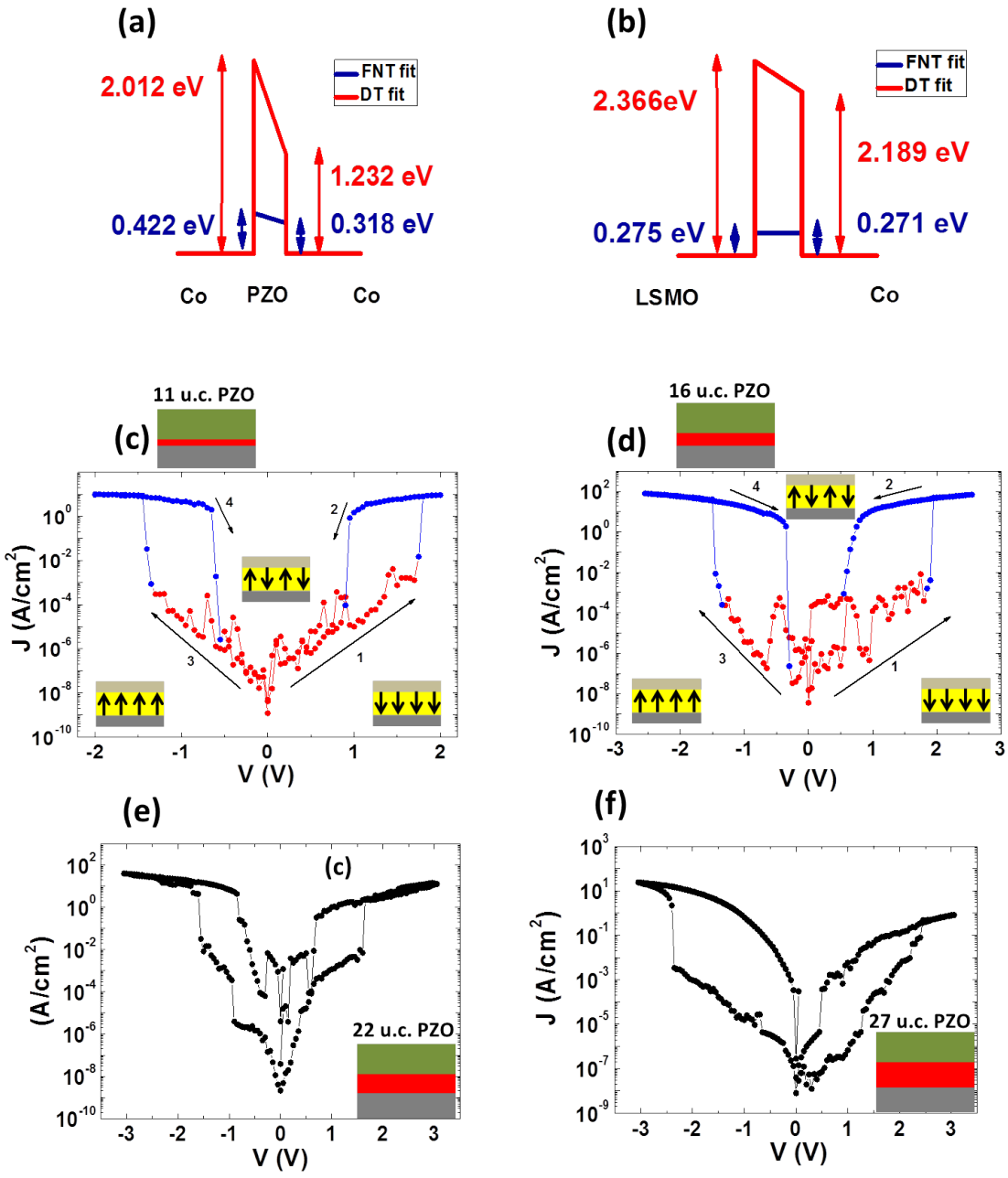


Figure 6.2: a-b) Barrier profiles for the 11 u.c. and 16 u.c. PZO devices corresponding to c-d); $I(V)$ characteristics for c) 11 u.c., d) 16 u.c. and e) 22 u.c.; f) 27 u.c. thick PZO barriers.

observed from resistive switching in PZO single crystal at high temperatures [188]. The resistance-area (RA) product is in the ranges $10^7\Omega\mu m^2$ and $10^{12}\Omega\mu m^2$, higher than reported in [179] for memory applications.

The specific shape of the current-voltage dependence excludes the formation of conducting filaments (which is the typical mechanism in unipolar and bipolar resistive switching [189]) since it is nonlinear and has a threshold resistive switching-like behaviour. The threshold resistive switching has been reported mainly in binary oxides and chalcogenides such as $VO_2$, $TiO_2$ and GeSe [190] in which the resistive switching might be caused by a temperature-induced metallic phase [191], a non-stoichiometric phase induced by migration of oxygen ions and Magnéli phases [192]. However, there are no reports of the threshold resistive switching in perovskite oxide junctions. In this case, PZO does not present complex phases like Magnéli phases nor highly conductive phases. Therefore it is reasonable to attribute the resistive switching in the current and the very high TER values to a genuine electronic origin which is a field-induced non-polar to polar phase transition consequently modifying the electronic barriers at both AFE-metal electrode interfaces.

The heights of the barriers at the two interfaces can be determined by fitting the experimental data with a direct tunnelling model and Fowler-Nordheim tunnelling model on the appropriate voltage intervals which are determined from a Fowler-Nordheim plot $\ln(j_{FNT}) = f(1/E)$:

$$j_{FNT} = \frac{e^2 m_e}{8\pi h m_e^* \Phi_{B,i}} E^2 \exp\left[-\frac{8\pi\sqrt{2m_e^*}}{3he}\frac{\Phi_{B,i}^{3/2}}{E}\right] = C_1 E^2 \exp\left(\frac{C_2}{E}\right) \tag{6.1}$$

Where $e$ is the electron charge, $m_e$ is the electron mass, $h$ is Planck's constant, $\Phi_{B,i}$ is the barrier height at the electrode, $E = V/d$ is the electric field on the barrier with the thickness $d$ and $m_e^*$ is the effective tunnelling mass of electrons. In figure 6.3 a and b the $2^{nd}$ and $4^{th}$ $I(V)$ branches are plotted. The FNT mechanism is highlighted by the linear dependence at the high voltages (low $1/E$ values) and the height of the barrier at the electrodes can be determined from the slope of the logarithmic plot:

$$\ln\left(\frac{j_{FNT}}{E^2}\right) = C_1 + C_2\left(\frac{1}{E}\right) \tag{6.2}$$

Where

$$\Phi_{B,i} = \left(\frac{3h}{8\pi\sqrt{2m_e^* C_2}}\right)^{(2/3)} \tag{6.3}$$

The dependence at low voltages (higher $1/E$ values) is associated in the literature with direct tunnelling and was fitted accordingly up to 1 V with the Brinkman

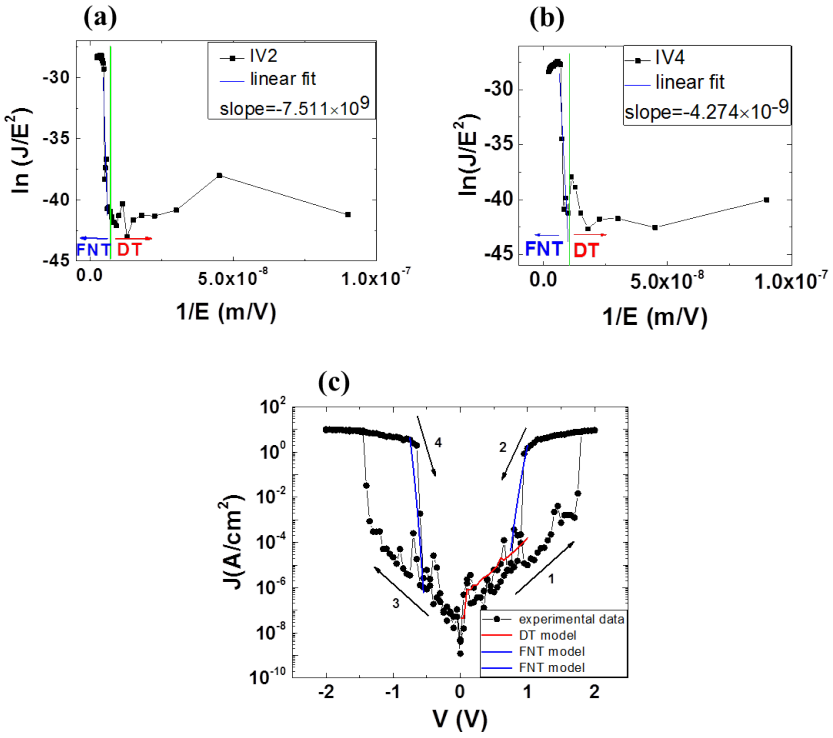


Figure 6.3: a-b) Fitting with the Fowler-Nordheim tunnelling mechanism on the $2^{nd}$ and $4^{th}$ $I(V)$ dependences; c) experimental data with direct tunnelling model (red line) and FNT model (blue lines) dependencies.

model (Equation 2.29). Figure 6.3 shows the experimental data and the fits of the proposed DT and FNT models.

In the AFE phase where the average polarisation is zero, the barrier is high, 2.012 eV at the PZO/Co interface and 1.232 eV at PZO/LZMO in 4.5 nm PZO (Figure 6.2 a). When the polarisation is induced by the applied field, the height of the barrier drops to 0.422 eV and 0.318 eV at the PZO/Co and PZO/LSMO, respectively. The crossover from direct tunnelling to FNT is highly probable due to applied voltages comparable with the barrier height and this too can induce very high values of TER as predicted for FTJ [41]. In the AFE phase, when applying low voltages, the tunnelling current is still sizeable despite the high barriers.

The size effect on AFE can be inferred from tunnelling currents. The effects on the coercivity of the AFE can be seen in figure 6.4. The voltage where the AFE-FE forward transition occurs ($2V_C$) increases with the thickness, from ~3V for 11 u.c. thick PZO to more than 3.5 V for 27 u.c. and reaches higher values ($2E_C$ in figure 6.4) of the field than determined in single crystal PZO [193]. Simultaneously, the

backward FE-AFE transition coercive voltage decreases dramatically being consistent with qualitative observations [194]. The bi-stability of the tunnelling current seen at low voltages could be caused by weak FE contributions of small remnant polarisation coexisting with the dominant AFE properties [69]. At reduced thicknesses it is largely suppressed, most probably due to large depolarising fields. In order to check ferroelectricity locally, a local piezoloop of the thinest sample (4.5 nm) was attempted with dual frequency resonance tracking PFM; the contact resonance at the surface was not detectable, supporting that it is non-ferroelectric.

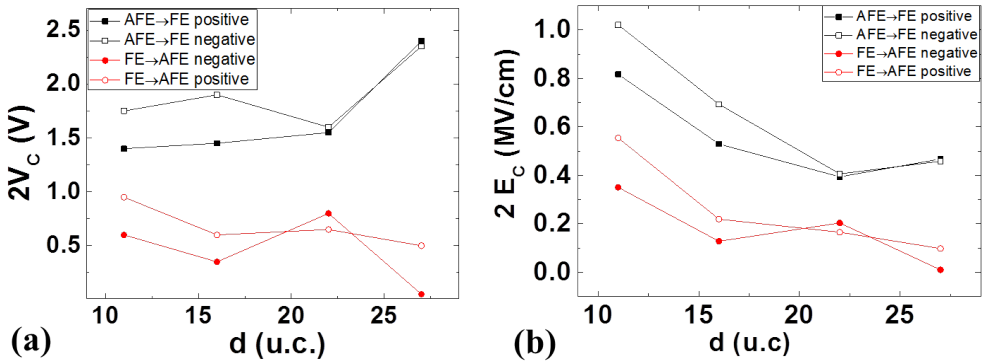


Figure 6.4: Variation of coercive AFE-FE (forward) and FE-AFE (backward) a) voltage and b) field with PZO thickness for positive and negative values of the voltage.

At room temperature, AFTJ shows a certain instability: after a relatively small number of cycles, the ferroelectric behaviour becomes dominant. After this point, two resistive non-volatile states can be obtained by switching the polarisation by applying electric pulses. Critical thickness studies available so far have been performed on broad thickness ranges with relatively large sampling intervals, so there are no details on the AFE-FE transition and coexistence of the two phases in small increment thickness variation for comparison. Considering the increasing effect of the depolarising field on polarisation when reducing the film thickness, it might be that at thicknesses ranging over a few unit cells, complex polarisation curling structures could take place, similar to the ferroelectric case [3]. Moreover, the 230$^o$C Curie temperature in the bulk might be significantly lowered in ultra-thin films, destabilising the AFE phase [193, 195]. In any case, further work is necessary to understand the size effects on AFE films which could lead to obtaining tunable, reliable and stable AFTJ devices.

In this section the study of antiferroelectric tunnel junctions is reported for the first time. PZO films with thicknesses down to ∼4 nm were shown to still have an AFE

behaviour, close to the theoretically predicted values [70]. The significant TER effect comes most probably from the combination of the non-polar AFE-polar FE and polar-non-polar transitions with the crossover from direct tunnelling to Fowler-Nordheim tunneling as the applied voltage increases. Due to the volatile nature of the AFTJ, they would not be suitable for information storage, rather would play the role of a complementary resistive switching device. The genuine electronic switching of the present antiferroelectric junctions, along with its ferroelectric counterpart, means they could be good candidates for multi-state and programable memristors with applications in cognitive computing [116, 117].

## 6.2 Temperature dependent electric measurements

Due to the ferromagnetic nature of the electrodes, TMR effect is expected to be present at low temperatures. Figure 6.5 shows the TMR measured at 10 K after cooling in -10 kOe magnetic field the samples having 4.5 nm and 6.5 nm thick PZO barriers. In the initial (as grown) state inverse TMR was obtained, similar to LSMO/PTO/Co tunnel junctions, but with lower values ($\sim$1.5%), rather comparable to the magnitude of the TMR effect in LSMO/PZT/Co junctions [8, 186]. The total magnetic moment measured on the samples using the SQUID magnetometer proves a direct correspondence between the resistance change and magnetisation switching in the electrodes. The existence of the TMR effect highlights that most of the current through the junctions is attributed to tunnelling processes.
Bulk lead zirconate has a complex structural phase diagram in electric fields [193] and the transition temperatures could vary significantly in the case of ultra-thin films, similar to ferroelectric materials. While the junctions present a certain bistability at room temperature, decreasing the temperature to 10 K produces irreversible changes in the junction properties. At low temperatures the junctions are more stable and the ferroelectric phase becomes dominant. This observation is in agreement with previous studies reporting thickness-induced ferroelectricity in PZO films [187, 69, 68]. By applying positive (negative) voltage pulses on the Co electrode, a high (low) resistance state can be obtained. Measuring the temperature-dependence of the junction resistance provides information on the tunnelling mechanisms. The data in figure 6.6 was acquired from a 6.5 nm thick PZO tunnel junction during heating from 10 K at 2 K/min in the states characterised by the minimum (P$\uparrow$) and maximum (P$\downarrow$) values. The junction resistance in the ON state (plotted in the inset) rises tenfold due to electron scattering at higher temperatures. Quite the opposite, in the OFF state, the junction resistance suffers two orders of magnitude

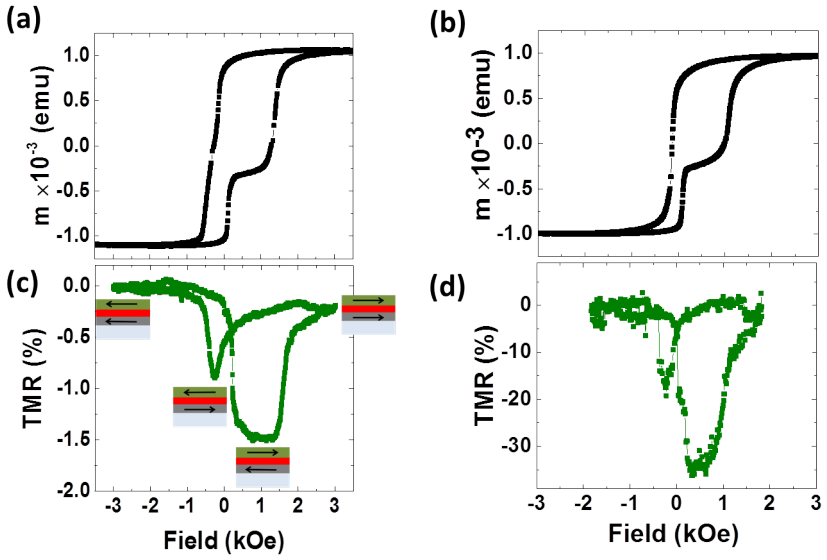


Figure 6.5: a-b) Magnetic moment dependence on the external magnetic field correlated with; c-d) tunnelling magnetoresistance effect for 11 and 16 u.c. PZO junctions, respectively; the schematic arrows indicate the parallel and antiparallel orientations of the LSMO and Co magnetisations when sweeping the magnetic field.

decrease with increasing temperature which also affects the TER. The magnitude of the TER varies from $10^5$% at 10 K to $10^2$% at 300 K and exceeds by three orders of magnitude the values measured in junctions containing PTO barriers (see previous chapter).

Ti and Zr ions, on one hand, are expected to behave similarly, both having less than half-filled $d$ shells. On the other hand, the dissimilarities in ionic size, shapes of the $3d$ and $4d$ orbitals could influence greatly the hybridisation with the interfacial Co ions. Evidently, the changes in Zr interactions with Co when the polarisation is reversed determine a much larger TER effect. Increasing TER effect up to similar values was also reported in LSMO/PTO/Co junctions by introducing at the PTO/Co interface a PZO monolayer in [9]. Therefore the high TER effect may be attributed to the interface, rather than the nature of the barrier itself.

The presence of inelastic processes are investigated in the OFF state (P↓), by investigating the temperature-dependence of the junction conductance near zero applied voltage (V=5 mV). In figure 6.7 two different behaviours can be observed for low and high temperatures. First, the conductivity increases slowly with $\sim$ 50% up to 200 K. Then inelastic hopping of electrons might be thermally activated causing a four-fold increase at room temperature. The overall temperature dependence is similar to the one observed in [163] and at high temperatures it behaves like

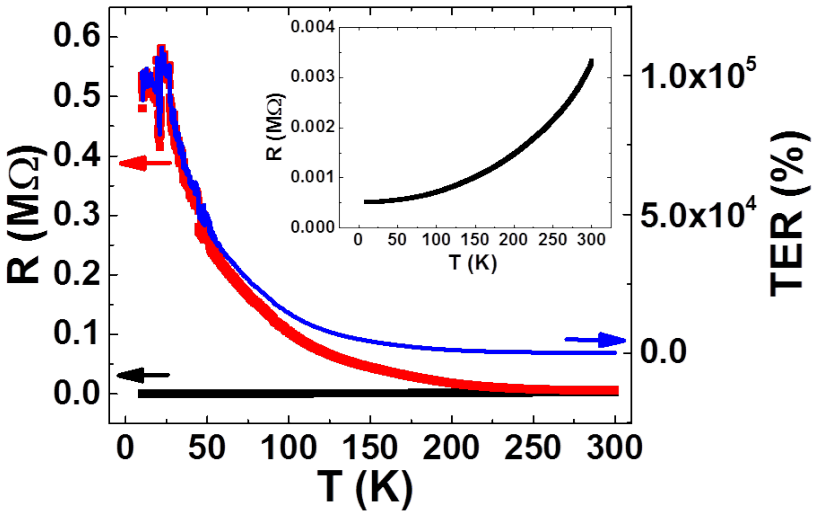


Figure 6.6: Temperature-dependence of minimum (ON state-black plot) and maximum (OFF state- red plot) resistance values measured at 100 mV and the resulting TER (blue plot) for a tunnel junction with a 6.5 nm thick PZO barrier; inset: zoom on the resistance in the OFF state.

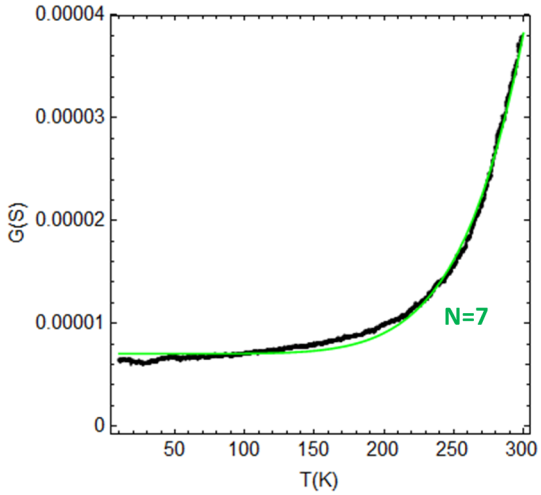


Figure 6.7: Conductance of a tunnel junction containing 6.5 nm PZO in the OFF state, measured with temperature at 5 mV and fitted with Glazman-Matveev model (green line).

the LSMO/PTO(6 u.c.)/Co junction. The experimental data is in good agreement with the Glazman-Matveev model, thus the transport at high temperatures might be dominated by the inelastic hopping of electrons through localised states. The dependence is fit using the FindFit model in Mathematica which allows setting reasonable constraints for the parameters, so they keep their physical meaning. The resultant parameters are estimated values, as the model does not provide information on the uncertainty. The obtained values are N=7 hopping channels, the same as in 6 u.c. PTO and the radius of the localised states inside the barrier $\alpha = 3.3 \times 10^{-2}$ nm, almost three times the value obtained in the PTO junction.

## 6.3 Influence of ferroelectric polarisation on spin transport

Zr and Ti ions have the same number of electrons in their $3d$ and $4d$ shells, thus their hybridisation with Co ions, according to the Goodenough-Kanamori rules should give rise to the same type of interaction. So far there are no experimental reports on the spin polarisation of lead zirconate. However, magnetic interaction between Zr and other transition ions at tunnel junction interfaces has been predicted theoretically in PZT/Co [169]. In the following section, the influence of the PZO polarisation on the spin transport is investigated by means of electric measurements.

At low temperatures the tunnel junctions present two stable non-volatile resistive states caused by the ferroelectric polarisation orientation. Negative and positive pulses were applied on the top Co electrode to switch the polarisation towards the Co and LSMO electrode, respectively. Figure 6.8 a shows the two reversible states obtained after subsequent switching of the polarisation by applying negative (P↑, ON state) and positive voltage pulses (P↓, OFF state). The corresponding $I(V)$ characteristics are shown in figure 6.8 b and are in good agreement with the direct tunnelling model. The resistance variation with applied magnetic field is measured at 100 mV and shown in figure 6.8 c. An inverse (negative) TMR is obtained when the polarisation is oriented towards the Co electrode (ON), the same as in LSMO/PTO/Co and LSMO/PZT/Co with the same orientation [7]. A normal TMR is obtained by reversing the polarisation towards the bottom LSMO electrode (OFF). The sign is also consistent with the LSMO/PZT/Co junctions. Within the Julliere model, the change in the TMR sign is produced by a change in the spin polarisation at one of the interfaces. The half-metallicity of LSMO is generally associated with a robust spin polarisation in magnetic tunnel junctions that should not suffer significant changes when the polarisation switches, thus the change occurs

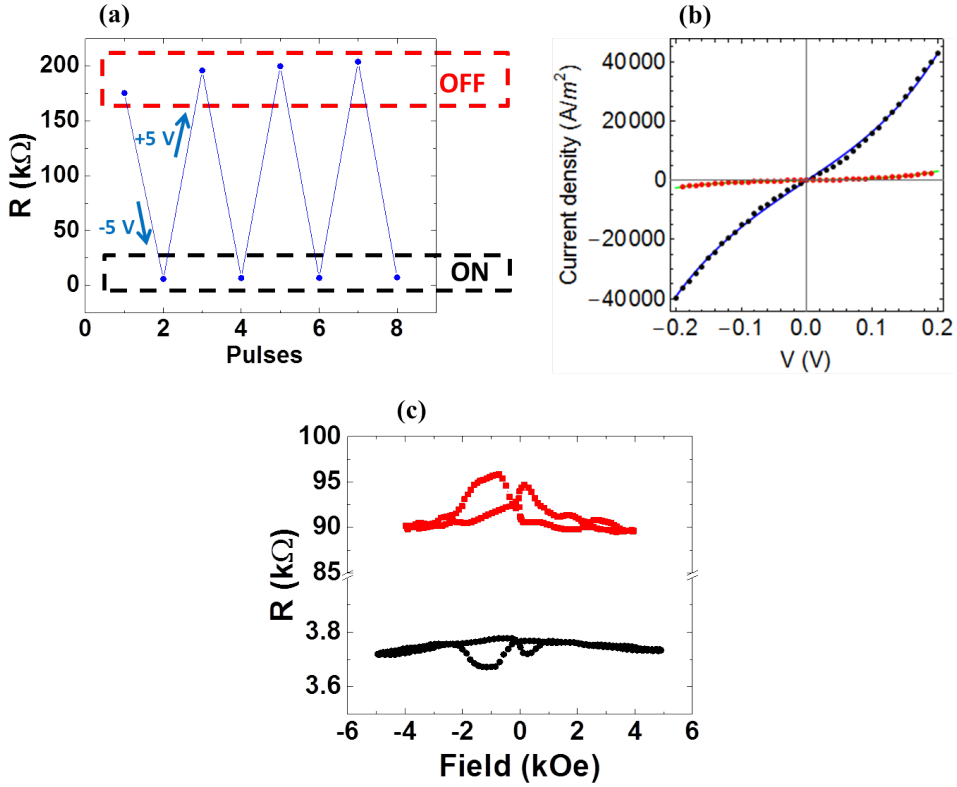


Figure 6.8: a) The two reversible resistive states (ON-black plot and OFF- red plot) of tunnel junctions with 6.5 nm PZO at $T$=10 K; b) the corresponding current-voltage curves fitted with a direct tunnelling model; c) resistance dependence on applied magnetic field in the two states.

at the PZO/Co interface. It is worth mentioning that negative TMR is obtained also in LSMO/PTO/PZO/Co junctions where just one monolayer of PZO is grown on top of the PTO ferroelectric barrier [9]. At barrier polarisation reversal, even the Zr ions seem to affect other interface-dependent parameters such as the TER, no significant change is observed in TMR. This could be due to no significant displacement of Zr ions occuring under applied electric field, but cannot exclude completely a possible effect of the LSMO/PTO interface.

In analogy with the better known Ti/Co interfaces, some hypotheses can be formulated about the Zr-Co interactions at the PZO/Co interface. First principle calculations are useful in understanding this effect. In LSMO/PZT/Co [169], they predict Co is antiferromagnetically coupled with Zr (Co induces an antiparallel magnetic moment on Zr, -0.04$\mu_B$/atom) when the ions are in immediate vicinity (P↑). This would determine, in analogy with PTO/Co interface, a negative spin polarisation and inverse TMR. When the ions are driven apart (P↓), the bond weakens, causing

a ferromagnetic coupling between the Zr and Co ions (parallel magnetic moment, $0.03\mu_B$/atom).

### 6.3.1 Voltage-dependence of tunnelling magnetoresistance

Due to its half-metallicity, LSMO is used as a spin analyser in probing the $d$ band of Co from the voltage dependence of TMR [196]. The TMR effect was measured at fixed dc voltages in low (P↑) and high (P↓) resistive states. The dependence of the resistance on the applied voltage is different for the two polarisation orientations as seen in figure 6.9. At negative measuring voltages, the values of the TMR are positive and similar in both states and at positive measuring voltage, TMR remains positive in P↑ and becomes negative in P↓ state. In the P↑ state, the maximum absolute value of TMR, which infers the highest density of states, occur at similar values of $V$ with LSMO/PTO/Co junctions.
There are several mechanisms which can be responsible for the TMR change of sign, driven by the device properties or by intrinsic properties of the barrier:

1. Extrinsic effects:

    - Magnetic reordering can be induced by electrostatic charge modulation. The superficial layers of LSMO are known to modify their magnetic properties at the interface with a ferroelectric. The charge accumulation in P↑ state is equivalent to a higher hole doping and induces antiferromagnetic alignment of the spins in the first layer. In the depletion state (P↓), ferromagnetic alignment with spins in the bulk of the LSMO electrode is favoured [159].
    - Different active atoms can be probed in the device. Due to the slightly rougher interfaces the LSMO/PZO/Co junctions, defects cannot be excluded so that in the two polarisation orientations, different atom channels can become responsible for conduction in the device. Bias-crafted bistability through oxygen vacancies was reported before in non-ferroelectric $SrTiO_3$ junctions, including a change of TMR sign in the two induced states [197].

2. Interface effects given by the intrinsic barrier properties:

    - At the PZO/Co interface, by shifting the Zr ions closer (P↑) to the Co ions at the PZO/Co interface, their $d$ orbitals overlap to a larger extent and determine a strong Zr-Co hybridisation resulting mainly in $d$ type tunnelling

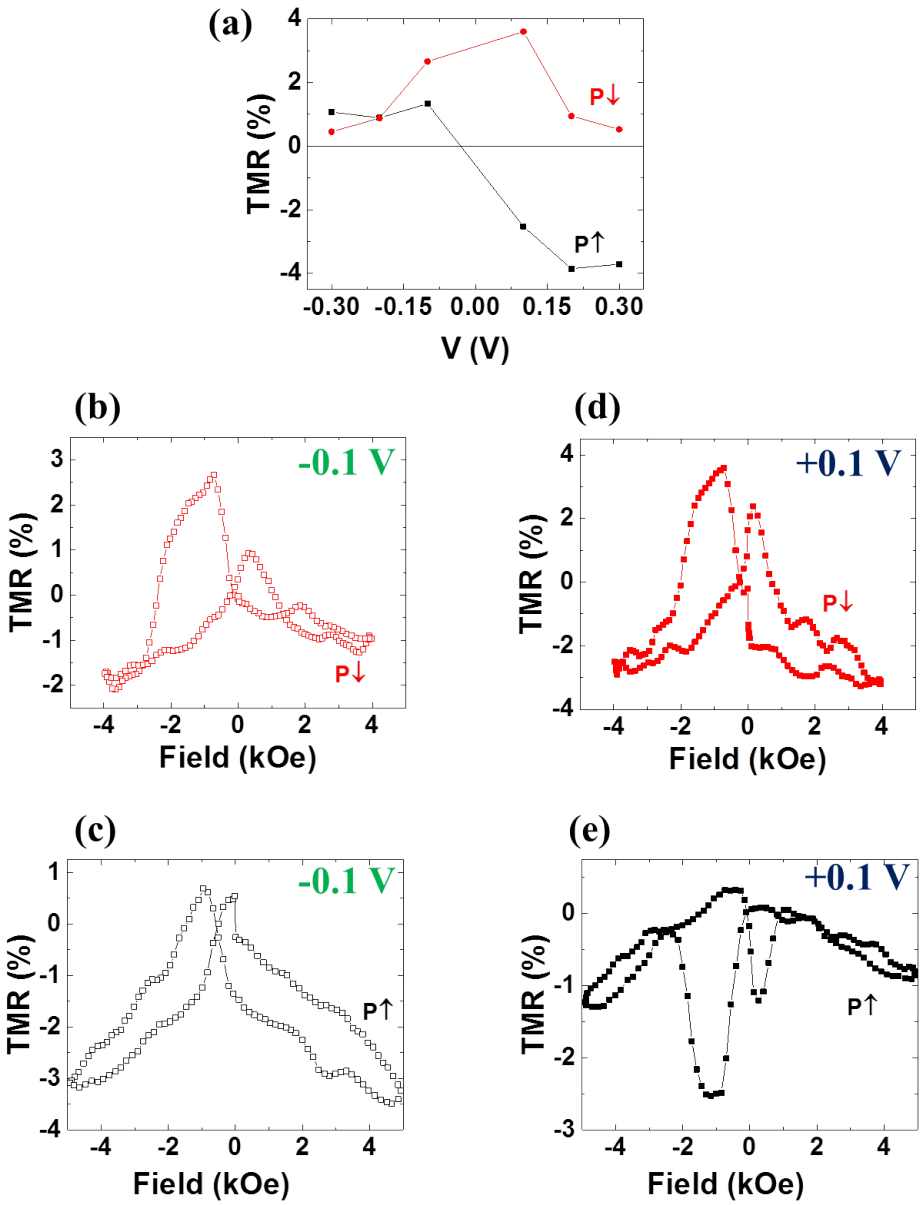


Figure 6.9: a) TMR as a function of the applied voltage in P↑ (black) and P↓ (red) states measured at 10 K for a tunnel junction with 6.5 nm thick PZO barrier; b-c) TMR measured at -0.1V; d-e) TMR measured at 0.1 V highlighting the change from normal to inverse with polarisation reversal.

electrons. By separating the Zr and Co ions (P↓), the $d$ orbital hybridisation is suppressed, favouring the Co-O hybridisation and the tunnelling is more likely to be dominated by the delocalised $s$ and $p$ states [198]. In figure 6.9, the TMR($V$) highlights the changes in the density of states at the PZO/Co interface with polarisation reversal. In prior theoretical studies it has been shown that the spin polarisation determined solely by $s$ orbitals has the opposite sign from the spin polarisation resulting from $s$, $p$ and $d$ orbitals combined [199]. In this case, the positive TMR in P↓ appears to be caused by $s$ orbitals, the TMR($V$) symmetrically decreases with increasing measuring voltage, similar to the $s$ hybridisation mechanism induced by AlO (ALO) in LSMO/STO/ALO/Co [35, 180]. Overall, TMR($V$) appears to be characterising different sub-bands of Co, depending on the polarisation orientation as depicted in figure 6.10. $d$ type electrons dominate the tunnelling process in the P↑ state, when Zr-Co bond is stronger, Co inducing an antiparallel magnetic moment on Zr. $s$ type electrons are dominating in the P↓ state, where the orbital overlapping is suppressed and a smaller parallel magnetic moment is induced on Zr. However, this suggested behaviour has yet to be confirmed in tunnel junctions with pure PZO barriers by means of theoretical calculations and synchrotron measurements of the interface magnetism.

- At the PZO/LSMO interface a similar mechanism cannot be completely excluded, but is generally considered not to change the spin polarisation sign due to its robust half-metallicity. There are reports of weak exchange interaction between Ti and Mn in $SrTiO_3$ [175] and $BaTiO_3$ [174], but no systematic studies on the effect of the polarisation reversal have been done.

### 6.3.2 Tunnelling magnetoresistance in devices with 6.5 nm thick PZO barrier

TMR was measured at 10 K by applying 100 mV in a junction containing a 6.5 nm thick PZO film. The state with the most significant TMR effect was studied with temperature (Figure 6.11). The states characterised by parallel and antiparallel magnetisations can be distinguished up to 150-200 K, then the TMR effect becomes negligible and disappears at lower temperatures than in the PTO junctions (where TMR of a few % can still be measured at room temperature). This might be due to the higher decaying rate of the interface magnetism and spin polarisation at the PZO/LSMO interface compared to the electrode bulk magnetic properties. From

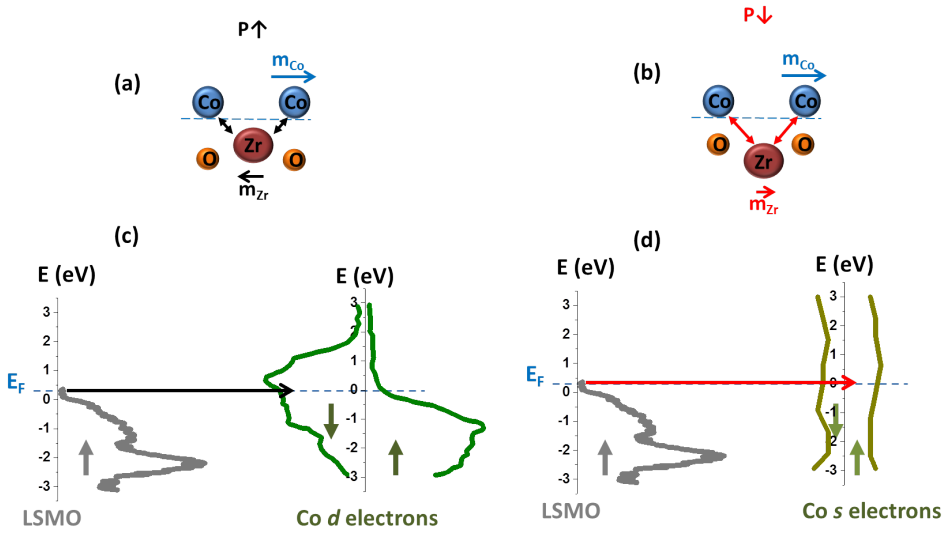


Figure 6.10: a-b) Schematics of Zr and O ions position relative to Co in P↑ and P↓ states; tunnelling in: c) P↑ state-electrons tunnel from the majority $d$ orbital of LSMO to the majority $d$ orbital of Co and d) P↓ state- electrons tunnel from the majority $d$ orbital of LSMO to the $s$ orbital of Co; adapted from [35].

the TEM analysis, PZO junctions exhibit a higher density of defects through the barrier and less sharp interfaces with the electrodes compared to PTO junctions. Therefore the TMR decay can be caused by the interface defects where significantly more inelastic scattering processes occur. Within the Glazman-Matveev model, the vanishing TMR at 200 K is related to the inelastic scattering channels which affect the conductance significantly above this temperature as seen for the OFF state previously.

In comparison, the tunnelling magnetoresistance is measured in a device with 4.5 nm PZO barrier presenting highly conductive channels (after dielectric breakdown) in parallel with the tunnelling channels. This device no longer obeys the Rowell criteria [130, 131], having an ohmic $I(V)$ characteristic and a metallic temperature-dependence of the resistance. Therefore, measuring a TMR effect is not sufficient to prove the functionality of a multiferroic tunnel junction. In this case, even though there is a measurable TMR in conductive junctions (Figure 6.12), its magnitude is significantly lower ($\sim 0.2\%$) than in functional tunnel junctions (a few % at 10 K in PTO and PZO junctions). Moreover, the TMR($V$) is symmetric, which is not characteristic of the expected $d$ orbital behaviour.

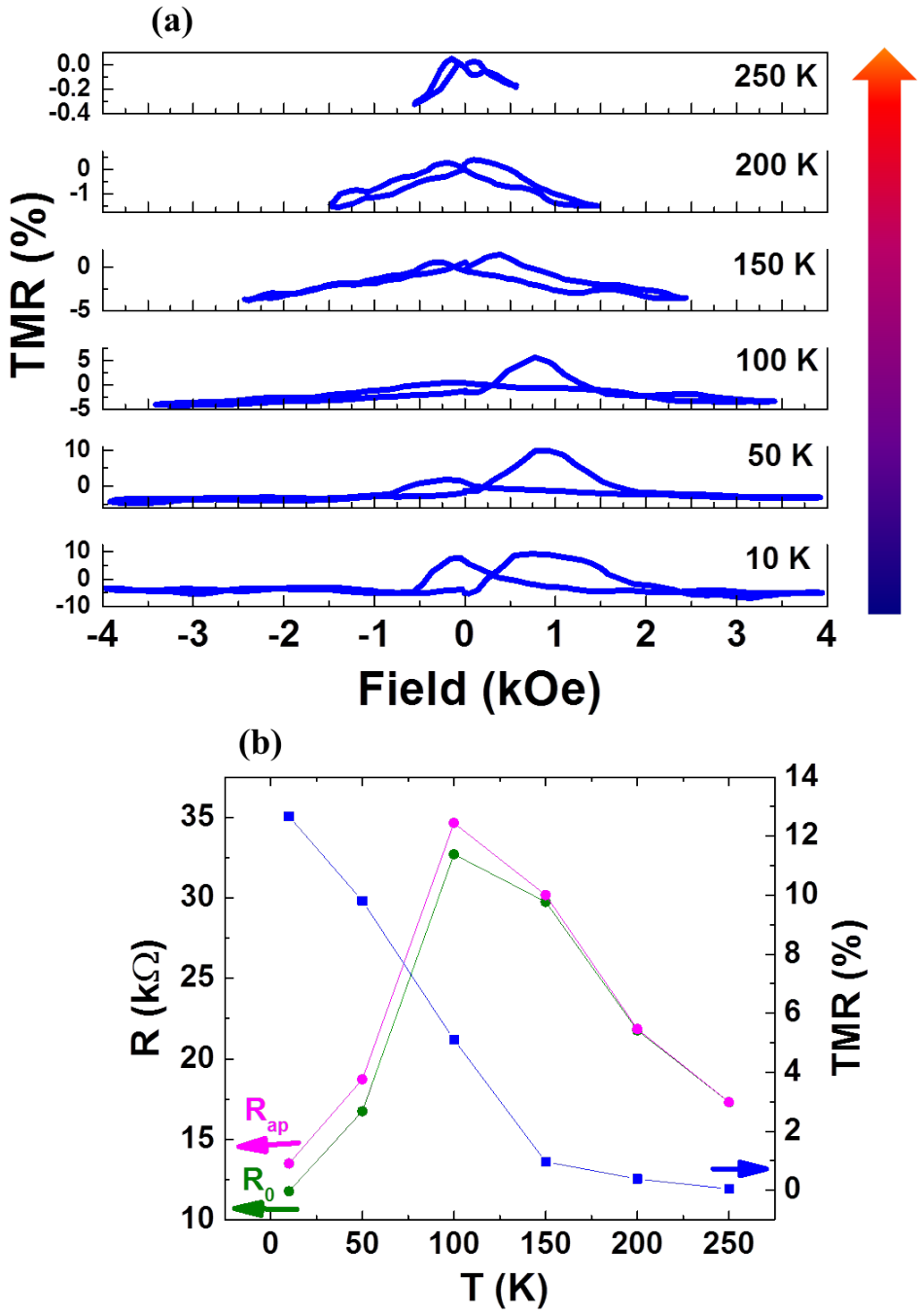


Figure 6.11: a) Normal TMR loops measured at different temperatures in junctions containing 6.5 nm PZO barrier and b) temperature-variation of the resistance in parallel and antiparallel alignment and TMR values.

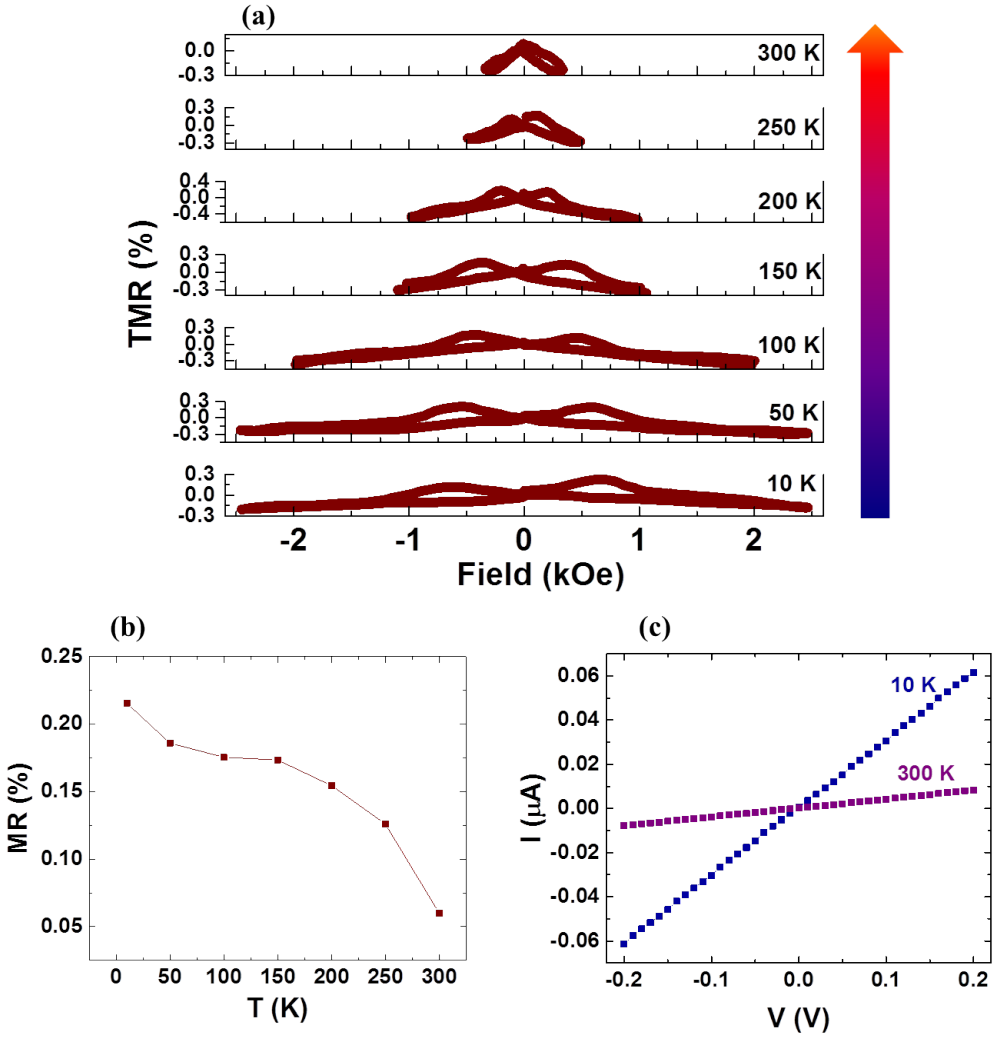


Figure 6.12: a) TMR loops at different temperatures of a conducting PZO junction; b) temperature-dependence of TMR with the values from a); c) Ohmic $I(V)$ characteristic of the junction at 10 and 300 K.

## 6.4 Summary

In this chapter, the study of antiferroelectric tunnel junctions is reported for the first time. It is shown experimentally that at room temperature, lead zirconate films can exhibit AFE properties down to a few nanometers thickness, at values approaching the theoretical predictions. The obtained AFTJ yield a TER effect with ON/OFF ratio of $10^7$, however, a certain instability is observed at room temperature where after a small number of cycles a ferroelectric-like behaviour is observed. One of the aims of this chapter is to present the proof of concept of antiferroelectric tunnel junctions, whose high TER value can be exploited once the stablity and reliability issues of the devices are solved.

At low temperatures, PZO exhibits a ferroelectric behaviour with two nonvolatile resistive states which determine a TER effect reaching $10^5\%$, with 3 orders of magnitude higher than the tunnel junctions containing PTO presented in the previous chapter. The polarisation orientation presents also a strong influence on the TMR: when polarisation is oriented towards the LSMO bottom electrode, the measured TMR is normal, while when it is oriented towards the Co electrode, the TMR is negative. The TMR($V$) dependencies indicate that different sub-bands might contribute to the tunnelling process in the two states. The magnetoelectric effect at the interface was predicted by first principle calculations, but here its influence is reported for the first time in experiments containing tunnel junctions with PZO barriers.

The results resemble the TMR modulation observed experimentally in LSMO/PZT/Co junctions and imply that the PZT response is dictated by the Zr ions.

# Chapter 7

# Conclusions

This last chapter summarises the content of the thesis and draws the main conclusions from the experimental observations and correlates them with existing information in literature. Further experiments and calculation on the $La_{0.7}Sr_{0.3}MnO_3$/ $PbTiO_3$/Co and $La_{0.7}Sr_{0.3}MnO_3$/$PbZrO_3$/Co systems are suggested in order to gain a broader view on spin transfer in tunnelling junctions with barriers and electrodes containing $3d$ and $4d$ orbital ions.

## 7.1 Summary

The aim of this thesis is to present the fabrication and characterisation of LSMO/PTO/ Co and LSMO/PZO/Co multiferroic tunnel junctions which combine the advantages of both magnetic tunnel junctions (MTJ) and ferroelectric tunnel junctions (FTJ) in single four-state memory devices. Chapter 1 presents the motivation behind the chosen materials and investigations.

In Chapter 2, the basic concept of electron tunnelling through a potential barrier is illustrated to set the base for understanding the experimental chapters. The functionality of quantum process is explained in real devices, highlighting the evolution of spintronic applications and defining the parameters which dictate their performance.

Chapter 3 presents the principles of the experimental methods used in the fabrication and characterisation of the tunnelling devices, while Chapter 4 presents the optimised parameters used in the fabrication process and step-by-step characterisation of the samples in order to obtain highly crystalline functional tunnel junctions and to understand the overall properties of the final devices. Apart from the characteristic four resistive states, the junctions present other interesting and distinct

behaviours given by the barrier properties.
In Chapter 5 LSMO/PTO/Co multiferroic tunnel junctions were investigated with reducing thickness. In this positive strain system, even though a local out of plane polarisation was detected, the micron-sized devices do not exhibit switchable polarisation at 3 unit cells (u.c.) thickness. Above this critical thickness, the domain pattern changes locally, going through a disordered phase with toroidal flux closure domains at 6 u.c and displays almost classic antiparallel domains with rough walls in 9 u.c. films. From 6 layers PTO, polarisation can be switched between two states: towards Co (P↑) and towards LSMO (P↓) by applying voltage pulses, giving rise to the TER effect ($\sim 10^2\%$). The ferroelectric polarisation affects the spin polarisation properties and the effect appears to weaken with increasing thickness and temperature.
In Chapter 6, the fabrication and characterisation of LSMO/PZO/Co tunnel junctions is reported for the first time. At room temperature, the junctions behave as antiferroelectric tunnel junctions, with a TER effect of $\sim 10^7\%$ determined by forward nonpolar-polar and backward polar-nonpolar transitions. One drawback is that after a relatively small number of cycles a dominant ferroelectric behaviour is activated. At low temperatures PZO exhibits ferroelectricity. The TER effect is higher with 3 orders of magnitude than in PTO junctions, which can be promising for applications once the stability and reliability of these junctions are improved.

## 7.2 Outlook

The ferroelectricity-controlled TMR in LSMO/PTO/Co and LSMO/PZO/Co can be discussed in relation to $PbZr_{0.2}Ti_{0.8}O_3$ (PZT) solid solution, as $PbTiO_3$ (x=1) and $PbZrO_3$ (x=0) are its component materials. Thus pure lead titanate and lead zirconate barriers are used to generalise the role of Ti and Zr ions, including in the TMR sign change from inverse (P↑) to normal (P↓) with polarisation reversal [7] in LSMO/PZT/Co. The polarisation orientation in the barrier influences the spin transfer by changes in the spin polarisation (density of states) at the barrier/electrode interface.
The TMR measured in LSMO/PTO/Co junctions is inverse as observed in junctions containing LSMO/$TiO_2$/Co [138], which coincides with the expected termination at the Co interface. It counter-intuitively decreases when P↑ state (creating shorter and stronger Ti-Co bonds) compared to P↓ state (longer and weaker Ti-Co bonds) and its values can be tailored between the two extremes by partially switching the polarisation. The TMR sign is given by the character of the tunnelling electrons

which depends on the type of magnetic interaction between ions at the interfaces. In both orientations, TMR($V$) implies that $d$ type electrons are responsible for tunnelling. The results are in partial agreement with theoretical predictions: the induced magnetic moment by Co on Ti preserves its orientation, but increases in magnitude when approaching the Co ions which would lead to a stronger hybridisation and higher TMR effect. This might indicate a different mechanism involved in Ti-Co hybridisation than in other systems containing 3d transition elements [6, 141] or a greater influence of the LSMO/PTO interface on the tunnelling properties.
In devices with PZO barriers, both normal and inverse TMR were measured at low temperatures by switching its polarisation. A normal TMR is obtained in the P↓ state (longer and weaker Zr-Co bonds) and an inverse TMR when the polarisation is reversed in P↑ state (shorter and stronger Zr-Co bonds). The voltage-dependent TMR implies $d$ character electrons are responsible for tunnelling in P↑ and $s$ and $p$ character electrons in P↓ state [180], depending on the Zr-Co hybridisation at the interface. This appears to be the same effect as in LSMO/PZT/Co junctions. It is worth mentioning that when PTO barrier is engineered with a PZO monolayer termination which cannot be ferroelectric, an inverse TMR is obtained which keeps its sign when polarisation is switched. In this case the great importance of the interface in ferroelectric tunnel junctions is inferred by the increased value of the TER.
This thesis shows that Ti and Zr $d$ shell electrons in the barrier have different effects on the spin transport properties in multiferroic tunnel junctions, despite their similar electron configurations. This can occur due to the different behaviours of magnetic moments induced by Co or due to the different degree of strain in the systems which can affect the orbital preference in LSMO through the Jahn-Teller effect.

## 7.3 Future work

The common behaviour of PZO and PZT might be caused by the Zr content, since the Ti ions produce a significantly different effect in PTO. The results indicate the TMR modulation with the ferroelectric polarisation observed in LSMO/PZT/Co is caused by the presence of Zr ions. Quantitative experimental confirmations of the results can be made by the determination of locally induced magnetic moment on Ti and Zr ions. For this purpose, X-ray absorbtion spectrum (XAS) and X-ray magnetic circular dichroism (XMCD) spectra are commonly used due to their sensitivity to the interface magnetisation and detection of small magnetic moments [141, 9, 200].

A detailed study would focus on the measurement of magnetic moments induced on Ti and Zr ions by Mn and Co at both barrier/ferromagnet interfaces in 'as grown' (unpoled), P↑ and P↓ states. From the presented results and other existent data, the magnetic moment induced on Ti and Zr should be robust (antiparallel to Mn ions in LSMO [175]) at the insulator/LSMO interface. The Ti-Co magnetic exchange was studied in several systems already: unpoled LSMO/$BaTiO_3$/Fe [141], LSMO/PTO/Co with for both polarisation orientations [9]. Thus it is expected that the magnitude of the magnetic moment induced on Ti by Co remains antiparallel, but smaller when Ti shifts downwards. So far, no experimental results are reported on Zr interaction with other *d* shell ions, but the change in the moment orientation is predicted at the PZT/Co interface [169] and expected at PZO/Co. A complementary study on these interfaces should be performed by theoretical calculations in the same conditions as the local moment measurements, in order to identify the contributions of the mechanisms proposed in Chapter 6. By understanding the multiferroic tunnel junctions, tailoring of their properties can be achieved, which along with improvements on stability and reliability can lead to performing multifunctional spintronic devices.

# Bibliography


[1] Y. Lee, J. Hayakawa, S. Ikeda, F. Matsukura, and H. Ohno, Applied Physics Letters **90**, 2507 (2007).

[2] A. Yadav, C. Nelson, S. Hsu, Z. Hong, J. Clarkson, C. Schleputz, A. Damodaran, P. Shafer, E. Arenholz, L. Dedon, et al., Nature **534**, 138 (2016).

[3] J. J. P. Peters, G. Apachitei, R. Beanland, M. Alexe, and A. M. Sanchez, Nature Communications (2016).

[4] B. Bein, H.-C. Hsing, S. J. Callori, J. Sinsheimer, P. V. Chinta, R. L. Headrick, and M. Dawber, arXiv preprint arXiv:1502.07632 (2015).

[5] F. Y. Bruno, S. Boyn, S. Fusil, S. Girod, C. Carrétéro, M. Marinova, A. Gloter, S. Xavier, C. Deranlot, M. Bibes, et al., Advanced Electronic Materials (2016).

[6] V. Garcia, M. Bibes, L. Bocher, S. Valencia, F. Kronast, A. Crassous, X. Moya, S. Enouz-Vedrenne, A. Gloter, D. Imhoff, et al., Science **327**, 1106 (2010).

[7] D. Pantel, S. Goetze, D. Hesse, and M. Alexe, Nature materials **11**, 289 (2012).

[8] A. Quindeau, I. Fina, X. Marti, G. Apachitei, P. Ferrer, C. Nicklin, E. Pippel, D. Hesse, and M. Alexe, Scientific reports **5** (2015).

[9] A. Quindeau, *Multiferroic tunnel structures (phd thesis), martin-luther-universitat halle-wittenberg, halle (saale), germany* (2015).

[10] A. Quindeau, V. Borisov, I. Fina, S. Ostanin, E. Pippel, I. Mertig, D. Hesse, and M. Alexe, Physical Review B **92**, 035130 (2015).

[11] S. Liang, *Quantum Tunneling and Field Electron Emission Theories*, EBL-Schweitzer (World Scientific Publishing Company Pte Limited, 2014), ISBN 9789814440226.

[12] J. Mamidala, R. Vishnoi, and P. Pandey, *Tunnel Field-effect Transistors (TFET): Modelling and Simulation* (Wiley, 2016), ISBN 9781119246282.

[13] E. H. Rhoderick and R. H. Williams, *Metal-Semiconductor Contacts (Second Edition)* (Clarendon Press, 1988).

[14] J. G. Simmons, Journal of applied physics **34**, 2581 (1963).

[15] J. G. Simmons, Journal of applied physics **34**, 1793 (1963).

[16] W. Brinkman, R. Dynes, and J. Rowell, Journal of applied physics **41**, 1915 (1970).

[17] A. Gruverman, D. Wu, H. Lu, Y. Wang, H. Jang, C. Folkman, M. Y. Zhuravlev, D. Felker, M. Rzchowski, C.-B. Eom, et al., Nano letters **9**, 3539 (2009).

[18] L. W. Nordheim, Proceedings of the Royal Society of London. Series A, Containing Papers of a Mathematical and Physical Character **121**, 626 (1928).

[19] R. H. Fowler and L. Nordheim, in *Proceedings of the Royal Society of London A: Mathematical, Physical and Engineering Sciences* (The Royal Society, 1928), vol. 119, pp. 173–181.

[20] D. Pantel, *(phd thesis: Multiferroische tunnelkontakte (multiferroic tunnel junctions)), martin-luther-university halle-wittenberg, halle, germany* (2011).

[21] M. N. Baibich, J. M. Broto, A. Fert, F. N. Van Dau, F. Petroff, P. Etienne, G. Creuzet, A. Friederich, and J. Chazelas, Phys. Rev. Lett. **61**, 2472 (1988).

[22] G. Binasch, P. Grünberg, F. Saurenbach, and W. Zinn, Phys. Rev. B **39**, 4828 (1989).

[23] A. Fert, *Handbook of spin transport and magnetism, Editors: E. Y. Tsymbal, I. Žuti* (Taylor  Francis Group, LLC, 2012).

[24] D. Tarling and F. Hrouda, *Magnetic Anisotropy of Rocks* (Springer Netherlands, 1993), ISBN 9780412498800.

[25] H. Kronm?ller and M. F?hnle, *Micromagnetism and the Microstructure of Ferromagnetic Solids*, Cambridge studies in magnetism (Cambridge University Press, 2003), ISBN 9780521331357.

[26] S. Srivastava, U. of Minnesota. Material Science, and Engineering, *Epitaxial Growth and Characterization of Multifunctional Heterostructures: Integrating Ferromagnets, Ferroelectrics, Insulators and III-V Semiconductors* (University of Minnesota, 2008), ISBN 9780549468349.

[27] M. Francombe and R. Hoffman, *Physics of Thin Films: Advances in Research and Development* (Elsevier Science, 2013), ISBN 9781483144931.

[28] I. Kézsmárki, S. Bordács, P. Milde, E. Neuber, L. Eng, J. White, H. M. Rønnow, C. Dewhurst, M. Mochizuki, K. Yanai, et al., Nature materials **14**, 1116 (2015).

[29] W. H. Meiklejohn and C. P. Bean, Physicsl Review **105**, 904 (1956).

[30] J. Nogués and I. K. Schuller, Journal of Magnetism and Magnetic Materials **192**, 203 (1999).

[31] W. Thomson, Proceedings of the Royal Society of London **8**, 546 (1856).

[32] T. Miyazaki and H. Jin, *The Physics of Ferromagnetism*, Springer Series in Materials Science (Springer-Verlag Berlin Heidelberg, 2012), ISBN 978-3-642-25583-0.

[33] S. S. P. Parkin, K. P. Roche, M. G. Samant, P. M. Rice, R. B. Beyers, R. E. Scheuerlein, E. J. OSullivan, S. L. Brown, J. Bucchigano, D. W. Abraham, et al., Journal of Applied Physics **85**, 5828 (1999).

[34] J. M. Slaughter, Annual Review of Materials Research (2009).

[35] J. M. De Teresa, A. Barthélémy, A. Fert, J. P. Contour, F. Montaigne, and P. Seneor, Science **286**, 507 (1999).

[36] E. Y. Tsymbal and H. Kohlstedt, Evgeny Tsymbal Publications p. 22 (2006).

[37] B. Yin and S. Qu, Journal of Applied Physics **114**, 063703 (2013).

[38] H. Kohlstedt, N. Pertsev, and R. Waser, in *Materials Research Society Symposium Proceedings* (Warrendale, Pa.; Materials Research Society; 1999, 2002), vol. 688, pp. 161–172.

[39] E. Tsymbal, A. Gruverman, V. Garcia, M. Bibes, and A. Barthélémy, MRS bulletin **37**, 138 (2012).

[40] I. Vrejoiu, G. Le Rhun, L. Pintilie, D. Hesse, M. Alexe, and U. Gösele, Advanced Materials **18**, 1657 (2006).

[41] D. Pantel and M. Alexe, Physical Review B **82**, 134105 (2010).

[42] R. Nelmes and W. Kuhs, Solid State Communications **54**, 721 (1985).

[43] *Fiz karlsruhe icsd*, `http://icsd.cds.rsc.org/viscalc/jsp` (accessed September 5, 2016).

[44] Y. A. Abramov, V. G. Tsirelson, V. E. Zavodnik, S. A. Ivanov, and I. D. Brown, Acta Crystallographica Section B **51**, 942 (1995).

[45] S. A. Chambers, S. Thevuthasan, R. F. C. Farrow, R. F. Marks, J. U. Thiele, L. Folks, M. G. Samant, A. J. Kellock, N. Ruzycki, D. L. Ederer, et al., Applied Physics Letters **79**, 3467 (2001).

[46] A. Urushibara, Y. Moritomo, T. Arima, A. Asamitsu, G. Kido, and Y. Tokura, Physical Review B **51**, 14103 (1995).

[47] H. Fujishiro, M. Ikebe, and Y. Konno, Journal of the Physical Society of Japan **67**, 1799 (1998).

[48] Y. Suzuki, H. Y. Hwang, S.-W. Cheong, and R. B. van Dover, Applied Physics Letters **71**, 140 (1997).

[49] S. Majumdar and S. van Dijken, Journal of Physics D: Applied Physics **47**, 034010 (2013).

[50] A. Haghiri-Gosnet and J. Renard, Journal of Physics D: Applied Physics **36**, R127 (2003).

[51] H. Hwang, S. Cheong, N. Ong, and a. B. Batlogg, Physical Review Letters **77**, 2041 (1996).

[52] K. L. Crispin and J. A. Van Orman, Physics of the Earth and Planetary Interiors **180**, 159 (2010).

[53] A. Vailionis, H. Boschker, W. Siemons, E. P. Houwman, D. H. A. Blank, G. Rijnders, and G. Koster, PHYSICAL REVIEW B **83**, 064101 (2011).

[54] J.-H. Park, E. Vescovo, H.-J. Kim, C. Kwon, R. Ramesh, and T. Venkatesan, Nature **392**, 794 (1998).

[55] M. Bowen, M. Bibes, A. Barthélémy, J.-P. Contour, A. Anane, Y. Lemaıtre, and A. Fert, Applied Physics Letters **82**, 233 (2003).

[56] I. Mazin, Physical Review Letters **83**, 1427 (1999).

[57] D. Schumacher, *Interplay Between Magnetic and Dielectric Phenomena at Tranistion Metal Oxide Interfaces*, vol. 56 (Forschungszentrum Jülich, 2013).

[58] P. Siwach, H. Singh, and O. Srivastava, Journal of Physics: Condensed Matter **20**, 273201 (2008).

[59] X. Hong, A. Posadas, A. Lin, and C. Ahn, Physical review B **68**, 134415 (2003).

[60] X. Hong, A. Posadas, and C. Ahn, Applied Physics Letters **86**, 142501 (2005).

[61] D. Pantel, S. Goetze, D. Hesse, and M. Alexe, ACS nano **5**, 6032 (2011).

[62] S. Pramanik, B. Pingguan-Murphy, and N. A. A. Osman, Int. J. Electrochem. Sci **8**, 8863 (2013).

[63] B. Noheda, D. Cox, G. Shirane, J. Gonzalo, L. Cross, and S. Park, arXiv preprint cond-mat/9903007 (1999).

[64] K. Nishida, S. Kasai, K. Tanaka, Y. Sakabe, F. Ishii, and T. Oguchi, Japanese Journal of Applied Physics **40**, 5806 (2001).

[65] R. E. Cohen, Nature **358**, 136 (1992).

[66] E. Salje, *Phase Transitions in Ferroelastic and Co-elastic Crystals*, Cambridge Topics I (Cambridge University Press, 1993), ISBN 9780521429368.

[67] J. Phillips and M. Thorpe, *Phase Transitions and Self-Organization in Electronic and Molecular Networks*, Fundamental Materials Research (Springer US, 2001), ISBN 9780306465680.

[68] K. Boldyreva, L. Pintilie, A. Lotnyk, I. Misirlioglu, M. Alexe, and D. Hesse, Ferroelectrics **370**, 140 (2008).

[69] A. R. Chaudhuri, M. Arredondo, A. Hähnel, A. Morelli, M. Becker, M. Alexe, and I. Vrejoiu, Physical Review B **84**, 054112 (2011).

[70] B. Mani, C.-M. Chang, S. Lisenkov, and I. Ponomareva, Physical review letters **115**, 097601 (2015).

[71] H. Fujishita and S. Katano, Ferroelectrics **237**, 209 (2000).

[72] H. B. Michaelson, Journal of Applied Physics **48**, 4729 (1977).

[73] S. Zhang, Physical review letters **83**, 640 (1999).

[74] L. Martin, Y.-H. Chu, and R. Ramesh, Materials Science and Engineering: R: Reports **68**, 89 (2010).

[75] J. Schou, Applied Surface Science **255**, 5191 (2009).

[76] D. H. A. Blank, M. Dekkers, and G. Rijnders, Journal of Physics D: Applied Physics **47**, 034006 (2014).

[77] J. A. Greer, Journal of Physics D: Applied Physics **47**, 034005 (2014).

[78] F. Träger, *Springer Handbook of Lasers and Optics* (Springer Berlin Heidelberg, 2012), ISBN 9783642194092.

[79] L. Su and T. U. of Texas at Arlington. Materials Science & Engineering, *Surface Patterning of Biodegradable Polymer in Tissue Engineering by Applying Photolithography* (University of Texas at Arlington, 2007), ISBN 9780549319955.

[80] M. Madou, *Fundamentals of Microfabrication: The Science of Miniaturization, Second Edition* (Taylor & Francis, 2002), ISBN 9780849308260.

[81] M. Hrouzek, *(phd thesis: Atomic force microscopy, modeling, estimation and control, universite joseph fourier-grenoble and brno university of technology, grenoble, france* (2007).

[82] P. Braga and D. Ricci, *Atomic Force Microscopy: Biomedical Methods and Applications*, Biomed Protocols (Humana Press, 2004), ISBN 9781592596478.

[83] I. Horcas, R. Fernandez, J. M. Gomez-Rodriguez, J. Colchero, J. Gomez-Herrero, and A. M. Baro, Review of Scientific Instruments **78**, 013705 (2007).

[84] A. Gruverman and A. Kholkin, Reports on Progress in Physics **69**, 2443 (2006).

[85] S. V. Kalinin, A. N. Morozovska, L. Q. Chen, and B. J. Rodriguez, Reports on Progress in Physics **73**, 056502 (2010).

[86] S. Jesse, *Asylum research webpage*, `https://www.asylumresearch.com/Applications`(accesed October 27, 2016).

[87] D. Williams and C. Carter, *Transmission Electron Microscopy: A Textbook for Materials Science*, no. v. 2 in Cambridge library collection (Springer, 2009), ISBN 9780387765006.

[88] J. P. P. Peters, *(phd thesis: Structure and ferroelectricity at the atomic level in perovskite oxides) at the university of warwick, coventry, uk* (2017).

[89] *Paderborn university, department of physics*, `https://physik.uni-paderborn.de/en/lindner/research/temstem/` (accessed August 4, 2016).

[90] L. Giannuzzi and N. University, *Introduction to Focused Ion Beams: Instrumentation, Theory, Techniques and Practice* (Springer US, 2006), ISBN 9780387233130.

[91] D. Jiles, *Introduction to Magnetism and Magnetic Materials, Third Edition* (CRC Press, 2015), ISBN 9781482238884.

[92] J. Barratt, M. R. Lees, G. Balakrishnan, and D. McK Paul, Applied Physics Letters **68**, 424 (1996).

[93] R. Cabassi, F. Bolzoni, and F. Casoli, Measurement Science and Technology **21**, 035701 (2010).

[94] M. Sawicki, W. Stefanowicz, and A. Ney, Semiconductor Science and Technology **26**, 064006 (2011).

[95] A. Quindeau, I. Fina, X. Marti, G. Apachitei, P. Ferrer, C. Nicklin, E. Pippel, D. Hesse, and M. Alexe, Scientific reports **5** (2015).

[96] M. Kawasaki, K. Takahashi, T. Maeda, R. Tsuchiya, M. Shinohara, O. Ishiyama, T. Yonezawa, M. Yoshimoto, and H. Koinuma, Science **266**, 1540 (1994).

[97] M. Huijben, L. W. Martin, Y.-H. Chu, M. B. Holcomb, P. Yu, G. Rijnders, D. H. A. Blank, and R. Ramesh, Phys. Rev. B **78**, 094413 (2008).

[98] D. Pesquera, G. Herranz, A. Barla, E. Pellegrin, F. Bondino, E. Magnano, F. Sanchez, and J. Fontcuberta, Nature Communications **3** (2012).

[99] L. Ranno, A. Llobet, R. Tiron, and E. Favre-Nicolin, Applied Surface Science **188**, 170 (2002).

[100] A. Haghiri-Gosnet, J. Wolfman, B. Mercey, C. Simon, L. P., M. Korzenski, M. Harvieu, R. Desfeux, and G. Baldinozzi, Journal of Applied Physics **88**, 4257 (2000).

[101] C. Kwon, M. Robson, K.-C. Kim, J. Gu, S. Lofland, S. Bhagat, Z. Trajanovic, M. Rajeswari, T. Venkatesan, A. Kratz, et al., Journal of Magnetism and Magnetic Materials **172**, 229 (1997).

[102] M. Mathews, F. M. Postma, J. Cock Lodder, R. Jansen, G. Rijnders, and D. H. A. Blank, Applied Physics Letters **87**, 242507 (2005).

[103] A. Urushibara, Y. Moritomo, T. Arima, A. Asamitsu, G. Kido, and Y. Tokura, Phys. Rev. B **51**, 14103 (1995).

[104] Y. Tokura, A. Urushibara, Y. Moritomo, T. Arima, A. Asamitsu, G. Kido, and N. Furukawa, Journal of the Physical Society of Japan **63**, 3931 (1994).

[105] K. Boldyreva, *(phd thesis: Growth and structure relations of epitaxial antiferroelectric/ferroelectric oxide multilayers, martin-luther-university halle-wittenberg and max planck institute for microstructure, halle, germany* (2007).

[106] W. H. Meiklejohn and C. P. Bean, Physical review **102**, 1413 (1956).

[107] M. Gierlings, M. Prandolini, H. Fritzsche, M. Gruyters, and D. Riegel, Physical Review B **65**, 092407 (2002).

[108] I. I. Naumov, L. Bellaiche, and H. Fu, Nature **432**, 737 (2004).

[109] M. Stachiotti and M. Sepliarsky, Physical review letters **106**, 137601 (2011).

[110] R. McQuaid, L. McGilly, P. Sharma, A. Gruverman, and J. Gregg, Nature communications **2**, 404 (2011).

[111] Y. Tang, Y. Zhu, X. Ma, A. Borisevich, A. Morozovska, E. Eliseev, W. Wang, Y. Wang, Y. Xu, Z. Zhang, et al., Science **348**, 547 (2015).

[112] C.-L. Jia, K. W. Urban, M. Alexe, D. Hesse, and I. Vrejoiu, Science **331**, 1420 (2011).

[113] C. Chappert, A. Fert, and F. N. Van Dau, Nature materials **6**, 813 (2007).

[114] D. Pantel, H. Lu, S. Goetze, P. Werner, D. J. Kim, A. Gruverman, D. Hesse, and M. Alexe, Applied Physics Letters **100**, 232902 (2012).

[115] Y. Yin, J. Burton, Y. M. Kim, A. Y. Borisevich, S. J. Pennycook, S. Yang, T. Noh, A. Gruverman, X. Li, E. Tsymbal, et al., Nature materials **12**, 397 (2013).

[116] J. P. Velev, C.-G. Duan, J. Burton, A. Smogunov, M. K. Niranjan, E. Tosatti, S. Jaswal, and E. Y. Tsymbal, Nano letters **9**, 427 (2008).

[117] A. Quindeau, D. Hesse, and M. Alexe, Frontiers in Physics **2**, 7 (2014).

[118] S. Prosandeev and L. Bellaiche, Physical Review B **75**, 172109 (2007).

[119] G. Catalan, J. Scott, A. Schilling, and J. Gregg, Journal of Physics: Condensed Matter **19**, 022201 (2006).

[120] C.-L. Jia, S.-B. Mi, K. Urban, I. Vrejoiu, M. Alexe, and D. Hesse, Nature materials **7**, 57 (2008).

[121] A. B. Yankovich, B. Berkels, W. Dahmen, P. Binev, S. Sanchez, S. Bradley, A. Li, I. Szlufarska, and P. M. Voyles, Nature communications **5** (2014).

[122] Y.-M. Kim, J. He, M. D. Biegalski, H. Ambaye, V. Lauter, H. M. Christen, S. T. Pantelides, S. J. Pennycook, S. V. Kalinin, and A. Y. Borisevich, Nature materials **11**, 888 (2012).

[123] J. Junquera and P. Ghosez, Nature **422**, 506 (2003).

[124] A. Glazer and S. Mabud, Acta Crystallographica Section B: Structural Crystallography and Crystal Chemistry **34**, 1065 (1978).

[125] D. Fong, C. Cionca, Y. Yacoby, G. Stephenson, J. Eastman, P. Fuoss, S. Streiffer, C. Thompson, R. Clarke, R. Pindak, et al., Physical Review B **71**, 144112 (2005).

[126] H. Pöttker and E. K. Salje, Journal of Physics: Condensed Matter **28**, 075902 (2016).

[127] L. Wang, Y. Dai, L. Yang, J. Xu, L. Zou, B. Tian, and D. Huang, Journal of Physics D: Applied Physics **45**, 505302 (2012).

[128] P. Ghosez and K. Rabe, arXiv preprint cond-mat/9911354 (1999).

[129] H. Yamada, A. Tsurumaki-Fukuchi, M. Kobayashi, T. Nagai, Y. Toyosaki, H. Kumigashira, and A. Sawa, Advanced Functional Materials **25**, 2708 (2015).

[130] B. J. Jonsson-Akerman, R. Escudero, C. Leighton, S. Kim, I. K. Schuller, and D. A. Rabson, Applied Physics Letters **77**, 1870 (2000).

[131] E. Burstein and S. Lundqvist, *Tunneling Phenomena in Solids: Lectures Presented at the 1967 NATO Advanced Study Institute at Risö, Denmark* (Plenum Press, 1969).

[132] M. Y. Zhuravlev, R. F. Sabirianov, S. Jaswal, and E. Y. Tsymbal, Physical Review Letters **94**, 246802 (2005).

[133] M. Müller, G.-X. Miao, and J. S. Moodera, EPL (Europhysics Letters) **88**, 47006 (2009).

[134] V. Shelke, D. Mazumdar, S. Faleev, O. Mryasov, S. Jesse, S. Kalinin, A. Baddorf, and A. Gupta, arXiv preprint arXiv:1010.0604 (2010).

[135] C. W. Miller, Z.-P. Li, I. K. Schuller, R. Dave, J. Slaughter, and J. Åkerman, Physical Review B **74**, 212404 (2006).

[136] J. Nogués and I. K. Schuller, Journal of Magnetism and Magnetic Materials **192**, 203 (1999).

[137] A. Hochstrat, C. Binek, and W. Kleemann, Physical Review B **66**, 092409 (2002).

[138] M. Bibes, M. Bowen, A. Barthélémy, A. Anane, K. Bouzehouane, C. Carrétéro, E. Jacquet, J. Contour, and O. Durand, Applied physics letters **82**, 3269 (2003).

[139] I. V. Marún, F. Postma, J. Lodder, and R. Jansen, Physical Review B **76**, 064426 (2007).

[140] J.-S. Noh, T. K. Nath, C.-B. Eom, J. Z. Sun, W. Tian, and X. Pan, Applied Physics Letters **79**, 233 (2001).

[141] S. Valencia, A. Crassous, L. Bocher, V. Garcia, X. Moya, R. Cherifi, C. Deranlot, K. Bouzehouane, S. Fusil, A. Zobelli, et al., Nature materials **10**, 753 (2011).

[142] J. Mathon and A. Umerski, Phys. Rev. B **63**, 220403 (2001).

[143] J. Hayakawa, I. S., F. Matsukura, H. Takahashi, and H. Ohno, Japanese Journal of Applied Physics **44**, L587 (2005).

[144] Y. Lu, X. W. Li, G. Q. Gong, G. Xiao, A. Gupta, P. Lecoeur, J. Z. Sun, Y. Y. Wang, and V. P. Dravid, Phys. Rev. B **54**, R8357 (1996).

[145] M. Viret, M. Drouet, J. Nassar, J. P. Contour, C. Fermon, and A. Fert, EPL (Europhysics Letters) **39**, 545 (1997).

[146] H. Béa, M. Bibes, S. Cherifi, F. Nolting, B. Warot-Fonrose, S. Fusil, G. Herranz, C. Deranlot, E. Jacquet, K. Bouzehouane, et al., Applied Physics Letters **89**, 242114 (2006).

[147] M. D. Kuz'min, Phys. Rev. Lett. **94**, 107204 (2005).

[148] F. Körmann, A. Dick, T. Hickel, and J. Neugebauer, Phys. Rev. B **83**, 165114 (2011).

[149] J.-H. Park, E. Vescovo, H.-J. Kim, C. Kwon, R. Ramesh, and T. Venkatesan, Phys. Rev. Lett. **81**, 1953 (1998).

[150] H. Y. Hwang and S.-W. Cheong, Nature **389**, 942 (1997).

[151] U. Gradmann, Journal of magnetism and magnetic materials **100**, 481 (1991).

[152] Y. Ogimoto, M. Izumi, A. Sawa, T. Manako, H. Sato, H. Akoh, M. Kawasaki, and Y. Tokura, Japanese journal of applied physics **42**, L369 (2003).

[153] S. Yuasa, A. Fukushima, T. Nagahama, K. Ando, and Y. Suzuki, Japanese Journal of Applied Physics **43**, L588 (2004).

[154] D. D. Djayaprawira, K. Tsunekawa, M. Nagai, H. Maehara, S. Yamagata, N. Watanabe, S. Yuasa, Y. Suzuki, and K. Ando, Applied Physics Letters **86**, 092502 (2005).

[155] S. Mukhopadhyay and I. Das, Physical review letters **96**, 026601 (2006).

[156] J. S. Moodera, L. R. Kinder, T. M. Wong, and R. Meservey, Phys. Rev. Lett. **74**, 3273 (1995).

[157] A. Sarkar, R. Adhikari, and A. Das, Physica B: Condensed Matter **407**, 4148 (2012).

[158] T.-S. Kim, Physical Review B **72**, 149901 (2005).

[159] C. Vaz, J. Hoffman, Y. Segal, J. Reiner, R. Grober, Z. Zhang, C. Ahn, and F. Walker, Physical review letters **104**, 127202 (2010).

[160] J. Sun, L. Krusin-Elbaum, P. Duncombe, A. Gupta, and R. Laibowitz, Applied physics letters **70**, 1769 (1997).

[161] Y. Ishii, H. Yamada, H. Sato, H. Akoh, Y. Ogawa, M. Kawasaki, and Y. Tokura, Applied physics letters **89**, 042509 (2006).

[162] J. Sun, K. Roche, and S. Parkin, Physical Review B **61**, 11244 (2000).

[163] Y. Lu, Journal of Applied Physics **102**, 123906 (2007).

[164] D. Preziosi, I. Fina, E. Pippel, D. Hesse, X. Marti, F. Bern, M. Ziese, and M. Alexe, Physical Review B **90**, 125155 (2014).

[165] Z. Wen, L. You, J. Wang, A. Li, and D. Wu, Applied Physics Letters **103**, 132913 (2013).

[166] L. Glazman and K. Matveev, Sov. phys. jetp **67**, 1276 (1988).

[167] Y. Xu, D. Ephron, and M. Beasley, Physical Review B **52**, 2843 (1995).

[168] Y. Lu, M. Tran, H. Jaffrès, P. Seneor, C. Deranlot, F. Petroff, J.-M. George, B. Lépine, S. Ababou, G. Jézéquel, et al., Physical review letters **102**, 176801 (2009).

[169] O. Vlasin, R. Jarrier, R. Arras, L. Calmels, B. Warot-Fonrose, C. Marcelot, M. Jamet, P. Ohresser, F. Scheurer, R. Hertel, et al., ACS applied materials & interfaces **8**, 7553 (2016).

[170] S. Valencia, A. Crassous, L. Bocher, V. Garcia, X. Moya, R. Cherifi, C. Deranlot, K. Bouzehouane, S. Fusil, A. Zobelli, et al., Nature materials **10**, 753 (2011).

[171] D. Preziosi, M. Alexe, D. Hesse, and M. Salluzzo, Physical review letters **115**, 157401 (2015).

[172] H. Chen, Q. Qiao, M. S. Marshall, A. B. Georgescu, A. Gulec, P. J. Phillips, R. F. Klie, F. J. Walker, C. H. Ahn, and S. Ismail-Beigi, Nano letters **14**, 4965 (2014).

[173] H. Lu, T. A. George, Y. Wang, I. Ketsman, J. Burton, C.-W. Bark, S. Ryu, D. Kim, J. Wang, C. Binek, et al., Applied Physics Letters **100**, 232904 (2012).

[174] Y. Liu, J. Tornos, S. te Velthuis, J. Freeland, H. Zhou, P. Steadman, P. Bencok, C. Leon, and J. Santamaria, APL Materials **4**, 046105 (2016).

[175] F. Y. Bruno, J. Garcia-Barriocanal, M. Varela, N. Nemes, P. Thakur, J. Cezar, N. Brookes, A. Rivera-Calzada, M. Garcia-Hernandez, C. Leon, et al., Physical review letters **106**, 147205 (2011).

[176] J. B. Goodenough, Physical Review **100**, 564 (1955).

[177] J. Kanamori, Journal of Physics and Chemistry of Solids **10**, 87 (1959).

[178] P. W. Anderson, Physical Review **115**, 2 (1959).

[179] S. S. Parkin, C. Kaiser, A. Panchula, P. M. Rice, B. Hughes, M. Samant, and S.-H. Yang, Nature materials **3**, 862 (2004).

[180] J. De Teresa, A. Barthélémy, A. Fert, J. Contour, R. Lyonnet, F. Montaigne, P. Seneor, and A. Vaures, Physical Review Letters **82**, 4288 (1999).

[181] A. Chanthbouala, V. Garcia, R. O. Cherifi, K. Bouzehouane, S. Fusil, X. Moya, S. Xavier, H. Yamada, C. Deranlot, N. D. Mathur, et al., Nature materials **11**, 860 (2012).

[182] W. Warren, J. Robertson, D. Dimos, B. Tuttle, G. Pike, and D. Payne, Physical Review B **53**, 3080 (1996).

[183] Z. Wen, C. Li, D. Wu, A. Li, and N. Ming, Nature materials **12**, 617 (2013).

[184] T. Jungwirth, X. Marti, P. Wadley, and J. Wunderlich, Nature nanotechnology **11**, 231 (2016).

[185] J. H. Jang and K. H. Yoon, Thin Solid Films **401**, 67 (2001).

[186] L. Pintilie and M. Alexe, Journal of applied physics **98**, 124103 (2005).

[187] L. Pintilie, K. Boldyreva, M. Alexe, and D. Hesse, Journal of Applied Physics **103**, 24101 (2008).

[188] I. Jankowska-Sumara, K. Szot, A. Majchrowski, and K. Roleder, physica status solidi (a) **210**, 507 (2013).

[189] R. Waser and M. Aono, Nature materials **6**, 833 (2007).

[190] D. S. Jeong, R. Thomas, R. Katiyar, J. Scott, H. Kohlstedt, A. Petraru, and C. S. Hwang, Reports on progress in physics **75**, 076502 (2012).

[191] R. Cope and A. Penn, Journal of Physics D: Applied Physics **1**, 161 (1968).

[192] J. Kim, C. Ko, A. Frenzel, S. Ramanathan, and J. E. Hoffman, Applied Physics Letters **96**, 213106 (2010).

[193] O. Fesenko, R. Kolesova, and Y. G. Sindeyev, Ferroelectrics **20**, 177 (1978).

[194] J. Zhai, Y. Yao, X. Li, T. Hung, Z. Xu, H. Chen, E. V. Colla, and T. Wu, Journal of applied physics **92**, 3990 (2002).

[195] B. Wang and C. Woo, Journal of applied physics **97**, 084109 (2005).

[196] M. Sharma, S. X. Wang, and J. H. Nickel, Physical Review Letters **82**, 616 (1999).

[197] M. Bowen, J.-L. Maurice, A. Barthélémy, P. Prodhomme, E. Jacquet, J.-P. Contour, D. Imhoff, and C. Colliex, Applied physics letters **89**, 103517 (2006).

[198] V. Borisov, S. Ostanin, I. Maznichenko, A. Ernst, and I. Mertig, Physical Review B **89**, 054436 (2014).

[199] E. Y. Tsymbal and D. Pettifor, Journal of Physics: Condensed Matter **9**, L411 (1997).

[200] E. Beaurepaire, H. Bulou, F. Scheurer, and K. Jean-Paul, *Magnetism and Synchrotron Radiation: New Trends*, Springer Proceedings in Physics (Springer Berlin Heidelberg, 2010), ISBN 9783642044984.